Università degli Studi di Milano-Bicocca

DIPARTIMENTO DI SCIENZA DEI MATERIALI
Doctorate in Materials Science – XXIV Cycle

A dissertation is submitted for the degree of
Doctor of Philosophy in Materials Science

Physical and Chemical Aspects of Thermoelectric Phenomena in Nanostructured Materials

Candidate:
Ekaterina Selezneva

Matricula: 725204

Advisor:
Prof. Dario Narducci

Dean of the Doctorate:
Prof. Gian Paolo Brivio

January 2012

I would like to dedicate this thesis to all the people who ever appreciated me, this way giving me strength and self-confidence

Acknowledgements

I would like to thank:

My advisor *Prof. Dario Narducci* for his strong encouragement, support, and guidance throughout my Ph.D. study that always led me to the solutions to all the challenges. I am also truly grateful to him for always finding time for me in spite of being often extremely busy.

Prof. Gian Paolo Brivio, the Dean of the Doctorate in Materials Science in the University of Milano-Bicocca who had been always very supportive to me. I am also very grateful to him for his prompt feedback when I was looking for a Ph.D. position, inviting me to this university for the participation in the Ph.D. admission examination.

Prof. Ali Shakouri for hosting me in his group in the University of California, Santa Cruz for my 6-month internship. It was a great professional as well as life experience for me. I am also truly grateful to him for his kindness and faith in me. He is a great professor and a great person whose model I would like to follow in my entire professional carrier.

Prof. Giampiero Ottaviani, *Prof. Stefano Frabboni* and *Dr. Rita Tonini* from the University of Modena, for the sample preparation and STEM analyses. I would also like to express my especial gratitude to *Prof. Giampiero Ottaviani* and *Prof. Stefano Frabboni* for their prompt feedback in the moment when I especially needed it.

Dr. Gianfranco Cerofolini from the University of Milano-Bicocca for the guidance and all the useful discussions.

Maria Cristina Fassina from the University of Milano-Bicocca for being always prompt and very helpful with all the administrative questions.

Dr. Maurizio Acciarri from the University of Milano-Bicocca for the help with the experimental setup for the Seebeck measurements and on the Hall effect measurements.

Dr. Elisabetta Romano from the University of Milano-Bicocca for the help with thermal treatment processes and for the useful advices.

Dr. Je-Hyeong Bahk from the University of California, Santa Cruz for the Seebeck and electrical conductivity simulations and for the general support in the project I was involved in. I am also truly grateful to him for being my good friend and for all the good sincere advices he gave me.

Prof. John Bowers from the University of California, Santa Barbara and *Prof. Joshua Zide* from the University of Delaware and their graduate students *Dr. Ashok Ramu* and *Dr. Laura Cassels* for their great contribution to the project I was involved in, as regarding the experimental part (which included the sample growth and processing and following Seebeck and Hall effect measurements) as well as during the preparation of the article.

Dr. Gilles Pernot from the University of California, Santa Cruz for the time-domain thermoreflectance measurements as well as for being my good friend and for all the useful advices he gave me.

Dr. Bjorn Vermeersch from the University of California, Santa Cruz for his prompt help any time it was needed as well as for many interesting talks we had. I enjoyed my first sightseeing tour in San Francisco thank to him too.

Prof. Zhixi Bian from the University of California, Santa Cruz for the discussions and very useful scientific advices.

Tela Favaloro from the University of California, Santa Cruz for the help on the Seebeck and electrical conductivity measurements.

Dr. Trevor Buehl from the University of California, Santa Barbara for the STEM analyses.

My colleagues and friends from the University of Milano-Bicocca: *Dr. Andrea Arcari*, *Dr. Simona Binetti*, *Dr. Stefano Marchionna*, *Dr. Alessia Le Donne*, *Lorenzo Ferraro*, *Dr. Natalia Mochenova*, *Dr. Agnieszka Mech*, *Vanessa Viganò*, *Andrea Picco*, *Gloria Preda*, *Daniele Scopece*, *Tommaso Crisenza*, *Dr. Michele Mauri*, *Laura Wahba*, *Maurizio Crippa*, *Andrea Scaccabarozzi*, *Lorenzo Caccamo*, *Bruno Lorenzi*, *Manuel Morgano*, *Sourav Jana*, *Bruno Vodopivec* and many others who were very nice and helpful to me throughout my Ph.D. study. Especially I would like to express my gratitude to *Andrea Arcari*, who also became my good friend.

My colleagues and friends from Santa Cruz:

My landlady *Marlene Majewska*, *Amirkoushyar Ziabari*, *Oxana Pantchenko*, *Ehsan Ardestani*, *Jesica Fernández*, *Hossein Talebi*, *Ramin Banan-Sadeghian*, *Kerry Maize*, *Anya Machulskaya*, *Xi Wang*, *Elnaz Ebrahimi*, *Sayeh Nojoomi*, *Mohsen Karimzadeh*, *Damla Ozcelik*, *Turhan Karadeniz*, *Yusuf Gören*, *Salvador Vazquez*, *Rubin Hood*, *Jose Armando Oviedo*, and many other nice people I met there.

Especially I would like to thank *Marlene*, *Amirkoushyar* and *Oxana* for being so kind and helpful to me all the time making me feel not so lonely away from home. I am also very grateful to *Marlene* for showing me the nice places in Santa Cruz and for the great conversations we had in the evenings after work. She also arranged with her sister my stay in Chicago, so I had a chance to visit this wonderful city. I will always remember the birthday party *Amirkoushyar* organized for me, as well as other parties with his friends with lots of Iranian music and dancing, which was a truly unforgettable experience.

Most of all I am grateful to my family for being truly proud of me and for their infinite love, support and understanding.

Finally, I would like to acknowledge Fondazione Cariplo for the funding.

Curriculum Vitae

Education

Jun. 2005	Bachelor of Science and Technology with specialization in Microelectronics	Saint Petersburg Electrotechnical University, Russia
Oct. 2008	Master of Science in Materials Science	University of Aveiro, Portugal
Jan. 2012	Doctor of Philosophy in Materials Science	University of Milano Bicocca, Italy

Publications

1. **E. Selezneva**, L. Cassels, A. Ramu, G. Pernot, T. Favaloro, J.-H. Bahk, Z. Bian, J. Bowers, J. Zide, and A. Shakouri. Thermoelectric transport in InGaAs with high concentration of rare-earth TbAs embedded nanoparticles. *J. Electron. Mater.* Submitted after revision: 2011

2. **E. Selezneva**, A. Arcari, G. Pernot, E. Romano, G. F. Cerofolini, R. Tonini, S. Frabboni, G. Ottaviani, A. Shakouri, and D. Narducci. Effect of Nanocavities on the Thermoelectric Properties of Polycrystalline Silicon. *MRS Proc. Vol. 1329* Published: 2011

3. D. Narducci, **E. Selezneva**, G. F. Cerofolini, S. Frabboni, and G. Ottaviani. High Figures of Merit in Degenerate Semiconductors. Energy Filtering by Grain Boundaries in Heavily Doped Polycrystalline Silicon. *The 9th European Conference on Thermoelectrics (ECT) AIP Proc.* Published: 2011

4. D. Narducci, **E. Selezneva**, A. Arcari, G. F. Cerofolini, E. Romano, R. Tonini, and G. Ottaviani. Enhanced Thermoelectric Properties of Strongly Degenerate Polycrystalline Silicon upon Second Phase Segregation. *MRS Proc. Vol. 1314* Published: 2011

5. D. Narducci, **E. Selezneva**, G. F. Cerofolini, E. Romano, R. Tonini, and G. Ottaviani. Opportunities and challenges in the use of heavily doped polycrystalline silicon as a thermoelectric material. An experimental study. *The 8th European Conference on Thermoelectrics (ECT) Proc.* Published: 2010

Schools and conferences

1. The 30th International Conference on Thermoelectrics (ICT), July, 17-21, 2011, Traverse City, USA

   Poster title: *Thermoelectric transport in InGaAs with high concentration of rare-earth TbAs embedded nanoparticles*

2. 2011 MRS Spring Meeting, April, 25-29, 2011, San Francisco, USA

   Oral presentation title: *Effect of Nanocavities on the Thermoelectric Properties of Polycrystalline Silicon*

3. 52nd Course of the International School of Solid State Physics, Workshop on Heat Control and Thermoelectric Efficiency, 23-28 October, 2010, Erice, Italy

   Poster title: *Enhancement of Thermoelectric Power in Heavily Doped Polysilicon Films Upon Isochronal Annealing*

4. 8th European Conference on Thermoelectrics (ECT 2010), 22-24 September, 2010, Como, Italy

5. 48th Course of the International School of Quantum Electronics, First Mediterranean International Workshop on Photoacoustic Photothermal Phenomena, 11-18 July, 2010, Erice, Italy

6. CIMTEC 2010, 5th Forum on New Materials, 13-18 June, 2010, Montecatini Terme, Italy

7. ICREA Workshop on Phonon Engineering, 24-27 May, 2010, Sant Feliu de Guixols, Spain

   Poster title: *Unexpected Trend of Seebeck Coefficient and Electrical Conductivity in Highly Doped Polysilicon Thin Films Upon Isochronal Annealing*

Abstract

The fivefold increase in the price of crude oil in 1973, accompanied by an increased awareness of environmental problems associated with global warming, resulted in an upsurge of scientific activity to identify and develop environmentally friendly sources of electrical power. The large amount of generated energy (almost 60%) is actually rejected in the form of heat. The ability to harvest even a small fraction of waste heat could have a huge impact on energy efficiency, leading to savings on fuel and reducing in CO_2 emission. Thermoelectric devices are among the systems which can be used for this purpose.

Thermoelectric efficiency of a material is described by the so-called thermoelectric figure of merit $ZT = S^2\sigma\kappa^{-1}T$, where S is the Seebeck coefficient, σ and κ are correspondingly the electrical and the total thermal conductivities. Nanostructuring has opened new ways to improve thermoelectric performance of a material either by decreasing κ or by increasing $S^2\sigma$.

We have studied thermoelectric properties of two nanostructured systems: heavily-doped polycrystalline silicon films with embedded nanocavities and InGaAs films with high concentration rare-earth TbAs embedded nanoparticles.

In the first system, we have analysed the effect of the formation of nanocavities, which were expected to act as efficient phonon scattering centres, thus reducing the thermal conductivity. The thermal conductivity was about half of the reported value in bulk polycrystalline silicon, however, the same low value was measured in the samples without nanocavities. This might suggest that the film microstructure dominates the thermal conductivity in all cases. The material also showed

outstanding thermoelectric properties. Upon thermal treatments at temperatures above 800°C we measured higher Seebeck coefficients than those normally found in monocrystalline silicon at corresponding doping level. This increase was found to be connected to the electron energy filtering by the potential barriers at the grain boundaries which accumulated dopant precipitates during the thermal treatments. As the result we have obtained a maximum ZT of 0.18 at room temperature.

In the second system, we studied the effect of embedded TbAs nanoparticles on the thermoelectric properties of InGaAs. In this group of materials, the nanoparticles serve to reduce thermal conductivity (through phonon scattering), increase Seebeck coefficient (through electron energy filtering), and increase of electrical conductivity (through nanoparticle donation of electrons). Both presence of the electron filtering and decrease of the thermal conductivity was experimentally observed. The electrical conductivity, however, drastically decreased and no enhancement of ZT was achieved.

Contents

List of Figures

LIST OF FIGURES

List of Tables

LIST OF TABLES

Chapter 1

Introduction

1.1 Energy at the crossroads

Human advances during the twentieth century were closely bound with an unprecedented rise of total energy consumption. This growth was accompanied by a worldwide change of the dominant energy base to hydrocarbons and rising share of fossil fuels used indirectly as electricity.

Substantial improvements of all key nineteenth-century energy techniques and introduction of new, and more efficient, better extraction and transportation processes resulted in widespread diffusion of labour-saving and comfort-providing conversions available at impressively low prices. Technical advances also ushered in an unprecedented mobility of people and goods. As a result, widespread ownership of private cars and mass air travel are among the most important social transformations of the second half of the twentieth century. Emergence of extensive global trade opened the paths to affluence even to countries lacking adequate fuel resources.

Even though many of the key twentieth-century trends, such as high reliance on fossil fuels, slow diffusion of renewable energy techniques, efficiency gains in all kinds of energy conversions, and rising per capita use of energy in low-income countries, will continue during the coming generations, there will have to be also some fundamental changes.

The key reason for these adjustments is the necessity to minimize environmen-

tal impact of energy use in general, and potentially very worrisome consequences of anthropogenic generation of greenhouse gases in particular. Extraction, transportation, and conversion of fossil fuels and generation and transmission of electricity have always had many local and regional environmental impacts ranging from destruction of terrestrial ecosystems to water pollution, and from acidifying emissions to photochemical smog. Carbon dioxide from the combustion of fossil fuels poses a different challenge: it remains the most important anthropogenic greenhouse gas, and its rising emissions will be the main cause of higher tropospheric temperatures.

Consequently, the future use of energy may not be determined just by the availability of resources or by techniques used to extract and convert them and by prices charged for them - but also by the need to ensure that the global energy consumption will not change many other key biospheric parameters beyond the limits compatible with long-term maintenance of global civilization. Prevention, or at least moderation, of rapid global warming is foremost, although not the sole, concern in this category, and it may turn out to be one of the most difficult challenges of the twenty-first century. Loss of biodiversity, human interference in the biogeochemical cycle, and health of the world ocean are other leading environmental concerns associated with the rising use of energy [26].

In this regards energy policy of Denmark implemented since the first oil crisis in 1973 presents an interesting case.

The Danish miracle

Like many other Western countries Denmark was totally dependent on the import of oil at the time of the first oil crisis in 1973. Almost all transport and residential heating was based on oil. Furthermore, 85% of the electricity supplied in Denmark was produced from oil. Altogether, prior to the oil crisis, more than 90% of the primarily energy supply was based on oil.

Denmark, like many other countries, was unprepared for the sudden rise in oil prices. Danish energy planning had been based on the principle of supplying whatever was demanded. Power stations were planned and built on a prognosis based on the historical development of needs. Denmark had no minister of energy

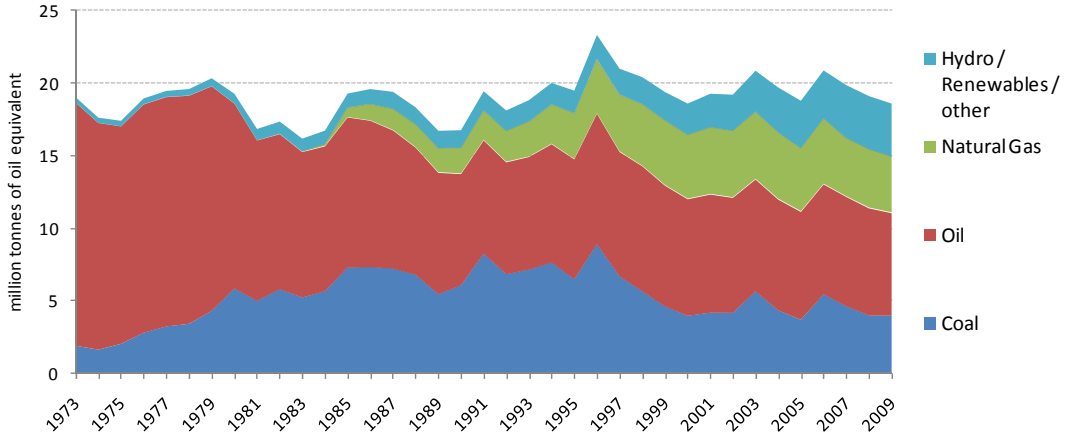

Figure 1.1: Danish primary energy supply [1]

and no energy department, no action plans in the case of being cut off from oil supplies, and no long-term strategy for the future in case oil resources were depleted.

Nevertheless, more than 30 years later, Danish society has proved its ability to implement rather remarkable changes. Fig. 1.1 shows the development of the primary energy supply of Denmark since 1973 and illustrates two important factors:

- Half of the oil consumption has been replaced by other fuels, e.g. coal, natural gas, and, to some extent, renewable energy.

- Denmark has managed to stabilize the primary energy supply at the same level as in 1973. This stabilization is unique compared to other countries, as it has been achieved simultaneously with a "normal western European" economic growth. Indeed, since 1980, the Danish economy has grown by 78%, while energy consumption has remained almost unchanged.

The primary means have been energy conservation and efficiency improvements in supply. Buildings have been insulated, and combined heat and power production has been expanded. Thus, 30 years later, the primary energy supply for heating has been reduced to two-thirds of what was used prior 1973, even though the heated space area has increased by more than 50% in the same pe-

riod. The renewable energy share of the primary energy supply has increased from around zero in 1973 to 16% in 2007 [27].

1.2 Thermoelectric power generation

It can be seen in Fig. 1.2 that the large amount of generated energy (almost 60%) is actually rejected, usually in the form of heat. This loss is largest in electrical power generation and transportation.

The ability to harvest even a small fraction of waste heat could have a huge impact on energy efficiency, leading to savings on fuel and reducing in CO_2 emission. For very large scale waste heat recovery, traditional mechanical heat engines such as Rankine, Brayton, or Stirling engines can be used; these offer higher conversion efficiency than thermoelectric devices. However, these systems do not scale easily for small system applications and do not function well at temperatures <140°C. Thermoelectric devices can be competitive in the case of small systems where the size, reliability, and maintenance-free aspects are major factors.

A thermoelectric generator (TEG) is a solid-state heat engine in which the electron gas serves as the working fluid and converts a flow of heat into electricity. It has no moving components, is silent, totally scalable and extremely reliable.

In a working thermoelectric device, segments of p-type and n-type semiconductor materials are connected by shunts to form a thermocouple. The shunts are made of an excellent electrical conductor, such as copper. The voltage output from semiconductor thermocouples remains relatively low, hundreds of microvolts per degree, and in practice a large number of thermocouples are connected electrically in series and thermally in parallel by sandwiching them between two high thermal conductivity but low electrical conductivity ceramic plates made of aluminium oxide or nitride to form a module (Fig. 1.3). When the temperature gradient is applied this device generates electricity which can be used to power an electric load through the external circuit.

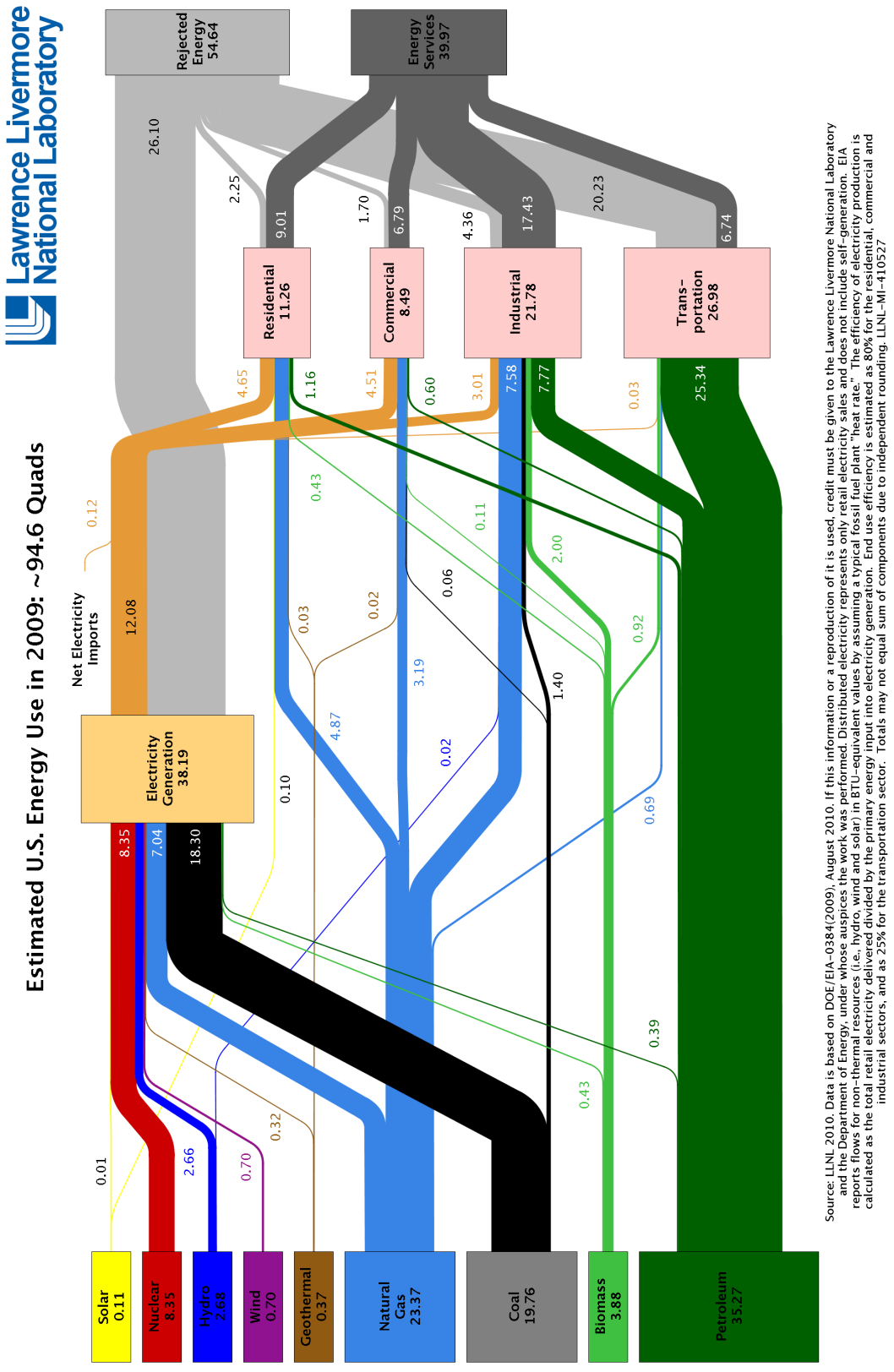

Figure 1.2: Estimated U.S. energy use in 2009 [2]

Isotopic powered thermoelectric generators

Thermoelectric power generation has its largest success in space applications. In 1961, the first radioisotope thermoelectric generator (RTG) used in a space mission was launched aboard a US Navy transit navigation satellite. The electrical power output of this RTG, which was called Space Nuclear Auxiliary Power (SNAP-3), was a mere 2.7 watts. This power was just a fraction of the satellite requirement and during the first decade of space exploration solar photovoltaic supplied the primarily electrical power to earth orbiting space crafts such as Explorer and numerous other space vehicles in programmes such as Ranger, Surveyor, Luner Orbiter, Pioneer and Mariner. However in 1970's attention turned towards the distant planets and in deep space missions to Jupiter and beyond where TEG power offers distinct weight advantages over solar cells. Since 1961 the United States has deployed 41 RTG's and one nuclear reactor powered generator providing power for 25 space systems. The most memorable of these were Apollo moon missions, the first Earthman on the moon and the Voyager deep space probes with the remarkable views of Saturn and its rings [28].

Although not as well documented as United States activities, the former USSR has also an impressive catalogue of TEG applications in space [29]. The first generators Orion-1 and Orion-2 employed a Polonium-210 heat source and powered the onboard equipment to artificial satellites Cosmos-84 and Cosmos-90. However the majority of Soviet thermoelectric reactors deployed in space relied on small nuclear reactors referred to as nuclear power plants (NPP) to provide heat. The first system in combination with thermoelectrics took the designation NPP-Buk. Typical reactors output were 100 kW thermal producing 2.5 to 3 kW electric. More than 30 Buk systems were launched within the period 1970-1988. The major draw-back of these systems was a short operational lifetime of 1-2 years.

In addition to space application isotopic powered TEGs are usually the most desirable power source for robotic or unmanned situations needing a few hundred watts (or less) of power for durations too long for fuel cells, batteries, or generators to provide economically, and in places where solar cells are not practical. However, employing radioisotopes as sources of heat has remained restricted to specialized applications where the thermoelectric generator's desirable properties listed above

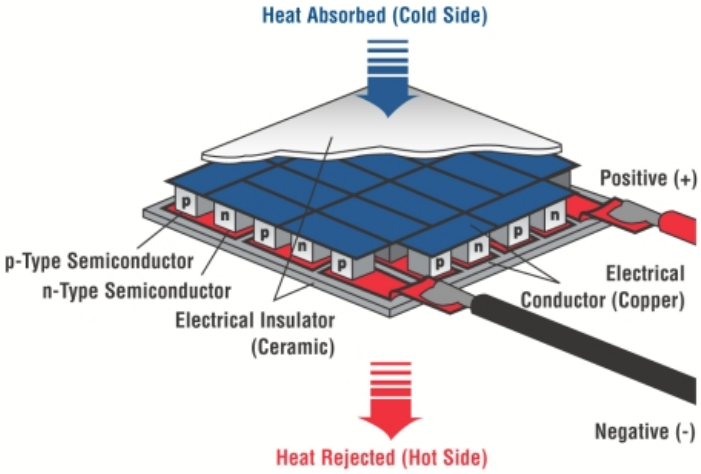

Figure 1.3: Schematic illustration of thermoelectric module. Source: www.newswireless.net

overweight its relatively low conversion efficiency (typically 5%).

Waste heat recovery

The fivefold increase in the price of crude oil in 1973, accompanied by an increased awareness of environmental problems associated with global warming, resulted in an upsurge of scientific activity to identify and develop environmentally friendly sources of electrical power. Thermoelectric power generation in applications, which employ waste heat as a heat source, is a totally green technology and when heat input is free, as with waste heat, the system's generating power density is of grater importance than its conversion efficiency in determining the system's economic viability.

Thermoelectric waste heat recovery for automobiles is a typical case that is being explored by several major car manufacturers. In a typical vehicle engine with a brake output power of 50 kW, an additional 35 kW of heat is generated and released to the atmosphere in the form of hot exhaust gases and another 35 kW is generated and released to the atmosphere through the engine cooling system. The exhaust flow is at a high temperature and represents a substantial loss of available or useful energy that could be harnessed. The techniques available to convert heat into shaft work include expansion devices, vapour power cycles, and solid

Figure 1.4: TEG prototype inserted into the exhaust system of Chevrolet Suburban. Source: General Motors

state and chemical regenerative techniques. However, in automotive applications, the simplicity of construction and light weight are important parameters. These criteria point to a solid-state solution and thermoelectric devices in particular [30].

Over the past 10 years, within multimillion-dollar/per year funding support from governments of major car manufacturing nations, a number of large R & D consortia have been formed to develop a thermoelectric recovery system from vehicle exhaust. The original TEG prototypes used stacks of thermoelectric material in box-shaped modules and were fitted into the exhaust lines of boosted gasoline engines. Test units has been installed in Chevrolet Suburban (Fig. 1.4) and increased its fuel economy by about 5% [31].

In the latest design, developed with Emitec and Benteler, the TEG has been integrated into the exhaust gas recirculation (EGR) cooler, used for reducing NO_x emissions at warm-up. Test units have been fitted to BMW's 5 Series diesel engine (Fig. 1.5(left)). The thermoelectric material was sandwiched inside double-walled tubes inside the EGR cooler: exhaust gas flew through the inside of the former; coolant around the outside of the latter (Fig. 1.5(right)). This system was able to generate about 250 W under optimum operation conditions, which is about half of the electrical demand for this particular car [32].

Thermoelectric power generation systems can be used for a wide range of other waste heat resources, such as hot water waste from steel plants, geothermal

Figure 1.5: TEG prototype integrated into the EGR cooler of BMWs 5 Series diesel engine (left) and its structure (right). Source: BMW Group

energy from hot springs, hot surfaces of furnaces, incinerators and other industrial processes, and remote subsea oil wells [28, 33].

Chapter 2

Background

There are two familiar methods for investigating the properties of electrical conductors. One may apply an electric field, then an electric current will result, and the ratio of current density to electric field when no temperature gradient is present defines the electrical conductivity, σ, of the material. On the other hand, if one applies a temperature gradient and measure the flow of heat which results when no electrical current is allowed to flow; under this conditions the ratio of heat flow per unit area to the temperature gradient defines the thermal conductivity, κ, of the material. There is, however, a third phenomenon which, at least until rather recently has been less studied. This is thermoelectricity. When we apply a temperature gradient to a conductor without an electric field, this of itself tends to produce not only the heat flow, but also an actual electric current, which is a thermoelectric current [34].

2.1 Thermoelectric and related effects

In 1794 - 1795 an Italian scientist Alessandro Volta wrote to a professor of physics in Royal University of Torino Anton Maria Vassali three letters entitled "A new paper on the animal electricity" [3]. In the first of these three letters Volta describes the following experiment:

"So, having bent an arc from 3 thick iron wires (Fig. 2.1), coarse and flexible, and having immersed its both ends into two glasses with water where carefully

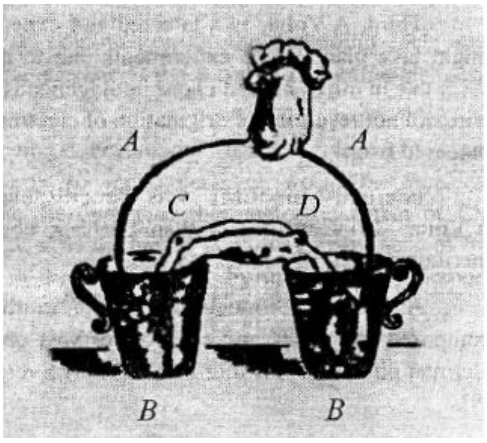

Figure 2.1: Scheme of Volta's experiment that resulted in the discovery of thermoelectricity. A - iron arc, B - glasses with water, C and D - frog parts placed in glasses with water [3]

as-prepared frog was placed in such a way that its hind legs were in one glass and its V back or spine (if spine alone was left) in the other glass, I manages to make it contract and jump. ... I immersed for a mere 30 seconds the end of such arc into boiling water, removed it and allowing no time for it to cool down to cool down, resumed the experiment with two glasses of cold water. It was then that the frog in the water started contracting, and it happened even two, three, four times on repeating the experiment till one end of the iron previously immersed into hot water did not cool down due to such more or less durable re-immersions or due to rather long stay in the air."

This experiment presenting a discovery of the thermoelectromotive force arising under the influence of temperature difference, however, remained little known to scientific community and the thermoelectric effect was named after German physicist Thomas Seebeck, who, 26 years later in 1821, discovered that a compass needle would be deflected by a closed loop formed by two metals joined in two places, with a temperature difference between the junctions (Fig. 2.2). Seebeck did not recognize there was an electric current involved, so he called the phenomenon the thermomagnetic effect. Danish physicist Hans Christian Ørsted rectified the mistake and coined the term "thermoelectricity". The voltage created by this effect can be derived from Eq. 2.1.

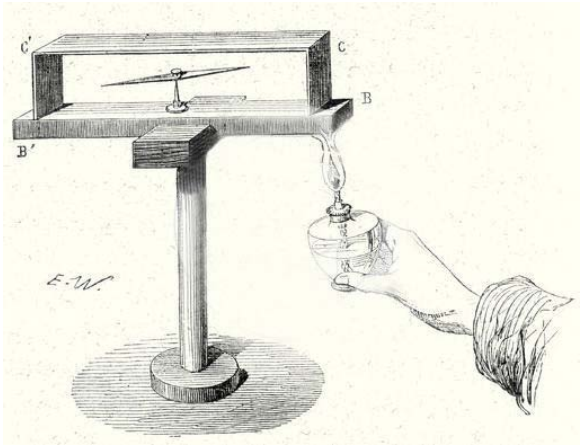

Figure 2.2: Seebeck experiment, 1821. ©Liszt Collection

$$V = \int_{T_1}^{T_2} (S_B(T) - S_C(T))dT \tag{2.1}$$

where S_B and S_C are the thermopowers (Seebeck coefficients) of metals B and C as a function of temperature, and T_1 and T_2 are the temperatures of the two junctions. The Seebeck coefficients are non-linear as a function of temperature, and depend on the conductors absolute temperature, material, and molecular structure. If the Seebeck coefficients are effectively constant for the measured temperature range, the absolute formula can be approximated as

$$V = (S_B - S_C) \times (T_2 - T_1) \tag{2.2}$$

Thirteen years after Seebeck made his discovery, Jean-Charles Peltier, a French watchmaker,observed that the passage of an electric current through a thermocouple produces a small heating or cooling effect depending on its direction. The Peltier heat Q generated or absorbed by the junction per unit time is equal to

$$\frac{\partial Q}{\partial t} = (\Pi_B - \Pi_C)I \tag{2.3}$$

where Π_B and Π_C are the Peltier coefficients of materials B and C and I is the electric current.

However, it was not immediately realized that the Seebeck and Peltier phe-

nomena are dependent on one another. This interdependency was recognized by William Thomson (who later became Lord Kelvin), in 1855. By applying the thermodynamic theory to the problem, he was able to establish a relationship between the coefficients and describe the Seebeck and Peltier effects. His theory also showed that there must be a third thermoelectric effect, which exists in a homogeneous conductor. This effect consists of reversible heating or cooling when there is both a flow of electric current and temperature gradient. If a current density J is passed through a homogeneous conductor, the heat production q per unit volume is:

$$q = \rho J^2 - \mu J \vec{\nabla}_x T \tag{2.4}$$

where ρ is the resistivity of the material, $\vec{\nabla}_x T$ is the temperature gradient along the wire and μ is the Thomson coefficient. The first term is the Joule heating, which does not change in sign; the second term is the Thomson heating, which follows J changing sign. The relations between the three coefficients come as follows:

$$\mu = T\frac{dS}{dT} \tag{2.5}$$

$$\Pi = S \times T \tag{2.6}$$

where T is the absolute temperature.

The fact that the Seebeck and Peltier effects occur only at junctions between dissimilar conductors might suggest that they are interfacial phenomena but they are really dependent on the bulk properties of the materials involved. Nowadays, we understand that electric current is carried through a conductor by means of electrons that can possess different energies in different materials. When a current passes from one material to another, the energy transported by the electrons is altered, the difference appearing as heating or cooling at the junction, that is as the Peltier effect. Likewise, when the junction is heated, electrons are enabled to pass from the material in which the electrons have the lower energy into that in which their energy is higher, giving rise to an electromotive force [35].

2.2 Boltzmann transport and thermoelectric coefficients

The transport of electric charge in solid is due to quasi-free electrons. In metals and semiconductors electrons carry not only the charge, but also the thermal energy. Through the interaction of the electrons with the periodic potential of the crystal lattice the energy of electrons must lie in discrete bands that are separated by forbidden regions of energy gaps. The lowermost, almost fully occupied band, is called the valence band by analogy with the valence electrons of individual atoms. The uppermost, almost unoccupied band is called the conduction band because only when electrons are excited to the conduction band current can flow.

According to quantum statistical mechanics, the probability that an electron state of energy, E, will be occupied is given by the Fermi distribution:

$$f_0(E) = \frac{1}{\exp\left(\frac{E-E_F}{k_B T}\right) + 1} \tag{2.7}$$

The quantity E_F has a value that depends on the total number of electrons that have to be accommodated, and k_B is Boltzmann's constant. The Fermi distribution function has the property that it is equal to zero when $(E - E_F) \gg k_B T$ and equal to unity when $(E - E_F) \ll k_B T$. The transition from zero to unity takes place over a very narrow range of energy ($\sim 2k_B T$). The energy, E_F, at which the Fermi distribution function is equal to $^1/_2$ is known as the Fermi level. If the number of permitted electron states in the energy range between E and $E + dE$ is represented by $g(E)dE$, the total number of electrons is

$$n = \int_0^\infty f_0(E) g(E) dE \tag{2.8}$$

It must be noted that electron conduction can take place only when the electrons in a band can move from one energy state to another. This, of course, cannot happen in an empty band since there are no electrons at all. It also cannot happen when a band is completely full, since there are then no free states into which an electron can move. Conduction is, therefore, entirely due to those electrons whose energy is such that the states are partially filled.

The density of electron states, $g(E)$, is small near the conduction band edge but rises rapidly within the band. Thus, if the Fermi level lies well within the conduction band, there will be a large number of electrons located near vacant states and the solid will be highly conducting. On the other hand, if the Fermi level lies within the energy gap, there will be virtually no electrons in the conduction band and the material will be an electrical insulator. When the Fermi level is close to the conduction band edge, there will be only few electrons but they will all be able to contribute to the conduction process. Because of their relatively small number, the conductivity will not be large and the material is called a semiconductor.

Before discussing the transport effects in a semiconductor, we shall introduce the concept of a relaxation time, τ, for the charge carriers. If the distribution function, f, is disturbed from its equilibrium value, f_0, it is assumed to relax towards f_0 according to

$$\frac{df(E)}{dt} = -\frac{f(E) - f_0(E)}{\tau} \tag{2.9}$$

The transport coefficients can be found by solving the Boltzmann equation that relates the effects of the applied fields and the scattering of the carriers. Considering transport processes that occur much slower than the relaxation process and assuming that the local deviation from equilibrium is small, the Boltzmann equation can be expressed as:

$$\frac{f(E) - f_0(E)}{\tau} = \vec{v}\frac{df_0(E)}{dE}\left(\vec{\nabla}_r E_F + \frac{(E - E_F)}{T}\vec{\nabla}_r T\right) \tag{2.10}$$

Here, $\vec{v}$ is the carrier velocity and E_F is the Fermi energy. The two terms in the brackets are associated with the electric field and the temperature gradient, respectively. We may use Eq. 2.10 to obtain the electric current density, j. The current density can be found as:

$$j = \mp \int_0^\infty e\vec{v} f(E) g(E) dE \tag{2.11}$$

where e is the electronic charge. The upper and lower signs apply for electrons and holes respectively.

In using the Boltzmann equation 2.10 to determine the transport coefficients, we can replace f by $(f - f_0)$ since there is no flow of any kind when $f = f_0$. Thus, Eq. 2.11 can be written in the form

$$j = \mp e \int_0^\infty \tau \upsilon^2 \frac{df_0(E)}{dE} \left(\vec{\nabla}_r E_F + \frac{(E - E_F)}{T} \vec{\nabla}_r T \right) g(E) dE \tag{2.12}$$

In order to determine the transport coefficients, we must use the appropriate boundary conditions. For simplicity we assume that both the current flow and the temperature gradient are in the x-direction. Thus, the electrical conductivity is given by the ratio j to the electric field $\varepsilon = -\frac{1}{e}\vec{\nabla}_x E_F$ when the temperature gradient $\vec{\nabla}_x T$ is zero. The Seebeck coefficient is equal to the ratio of the electric field ε to the temperature gradient when the electric current is zero:

$$\sigma = \left. \frac{j}{\varepsilon} \right|_{\vec{\nabla}_x T = 0} = -e^2 \int_0^\infty \tau \upsilon_x^2 \frac{df_0(E)}{dE} g(E) dE \tag{2.13}$$

$$S = \left. \frac{\varepsilon}{\vec{\nabla}_x T} \right|_{j=0} = \pm \frac{1}{e} \frac{e^2 \int_0^\infty \tau \upsilon_x^2 \frac{E - E_F}{T} \frac{df_0(E)}{dE} g(E) dE}{e^2 \int_0^\infty \tau \upsilon_x^2 \frac{df_0(E)}{dE} g(E) dE} \tag{2.14}$$

Eqs. 2.13 and 2.14 can be re-written as follows:

$$\sigma = -\int_0^\infty \sigma(E) dE \tag{2.15}$$

$$S = \pm \frac{k_B}{e} \frac{\int_0^\infty \sigma(E) \frac{E - E_F}{k_B T} dE}{\int_0^\infty \sigma(E) dE} \propto \langle E - E_F \rangle \tag{2.16}$$

where we introduce the differential conductivity,

$$\sigma(E) = e^2 \tau \upsilon_x^2 g(E) \frac{df_0(E)}{dE} \tag{2.17}$$

$\sigma(E)$ is a measure of the contribution of electrons with energy E to the total conductivity [9]. The Fermi window factor $\frac{df_0(E)}{dE}$ is a bell-shaped function centred at $E = E_F$ and has a width $k_B T$. It means that at a finite temperature only electrons near the Fermi surface contribute to the conduction process. In this picture the Peltier coefficient (the Seebeck coefficient multiplied by absolute tem-

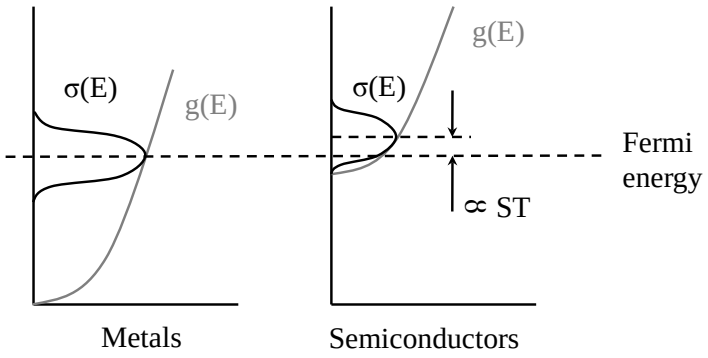

Figure 2.3: Density of states $g(E)$ and differential conductivity $\sigma(E)$ versus electron energy E for metals and semiconductors

perature) is the energy transported by the charge carrier measured with respect to the Fermi energy and averaged with $\sigma(E)\frac{df_0(E)}{dE}$. To achieve the best thermoelectric properties, $\sigma(E)$, within the Fermi window, should be as big as possible to increase the electrical conductivity and, at the same time, as asymmetric as possible with respect to the Fermi energy to enhance the thermopower (Fig. 2.3).

For any typical 3D thermoelectric material there is always a trade-off between electrical conductivity and the Seebeck coefficient. It can be easily explained of we consider the concept of differential conductivity. When the Fermi energy is close to the band edge, the density of states is asymmetric with respect to the Fermi level. This means that, e.g., for an n-type material, more states are available for transport above the Fermi energy than below it, so the average energy of the carrier will be higher than the Fermi energy. The electrical conductivity can be increased by doping. As we increase the doping in the material, the Fermi energy moves deeper in the band, the differential conductivity becomes more symmetric with respect to the Fermi energy. As the result the average energy of the carrier will be close to the Fermi energy, and the value of the Seebeck coefficient will be low. As the doping increases further, the symmetry of the differential conductivity remains constant, however, the Seebeck coefficient will still keep decreasing. This is because the denominator of the Eq. 2.16 is proportional to electrical conductivity. As the doping in the material and the

conductivity increases, we need a larger asymmetry in the differential conductivity if we want to keep the Seebeck coefficient high [9].

2.3 Heat transport

Heat energy can be transmitted through solids via electrical carriers (electrons or holes) and lattice waves. The total thermal conductivity κ can be thus written as a sum of the components:

$$\kappa = \kappa_e + \kappa_l \tag{2.18}$$

where κ_e and κ_l are the electrical and lattice component, respectively.

Lattice thermal conductivity is the dominant thermal conduction mechanism in non-metals including semiconductors and alloys. In solids atoms vibrate about their equilibrium positions. The vibrations of atoms are not independent of each other, but are rather strongly coupled with neighbouring atoms. The crystal lattice vibration can be characterized by the normal modes, or standing waves. The quanta of the crystal vibrational field are called "phonons". In the presence of a temperature gradient, the thermal energy is considered as propagating by means of wave packets consisting of various normal modes, or phonons.

The average number of phonons $n^0_{\vec{q}}$ with wave vector $\vec{q}$ is given by Bose-Einstein distribution:

$$n^0_{\vec{q}} = \frac{1}{\exp\left(\frac{\hbar\omega_{\vec{q}}}{k_B T}\right) - 1} \tag{2.19}$$

Once again employing the relaxation time approximation, the Boltzmann transport equation can be expressed as:

$$\frac{n_{\vec{q}} - n^0_{\vec{q}}}{\tau_q} = -(\vec{v}_g \cdot \vec{\nabla}_r T)\frac{\partial n^0_{\vec{q}}}{\partial T} \tag{2.20}$$

where $\vec{v}_g$ is the phonon group velocity and τ_q is the phonon scattering relaxation time. The heat flux due to a phonon mode $\vec{q}$ is the product of the average phonon energy and the the group velocity.

$$\vec{Q} = \sum_{\vec{q}} n_{\vec{q}} \hbar \omega_{\vec{q}} \vec{v}_g \tag{2.21}$$

We can replace $n_{\vec{q}}$ by $n_{\vec{q}} - n^0_{\vec{q}}$ since there is no flow of any kind when $n_{\vec{q}} = n^0_{\vec{q}}$. Substituting Eq. 2.20 into Eq. 2.21 yields

$$\vec{Q} = -\sum_{\vec{q}} \hbar \omega_{\vec{q}} v_g^2 \langle \cos^2 \theta \rangle \tau_q \frac{\partial n^0_{\vec{q}}}{\partial T} \vec{\nabla}_r T = -\frac{1}{3} \sum_{\vec{q}} \hbar \omega_{\vec{q}} v_g^2 \tau_q \frac{\partial n^0_{\vec{q}}}{\partial T} \vec{\nabla}_r T \tag{2.22}$$

where θ is the angle between $\vec{v}_g$ and $\vec{\nabla}_r T$. The lattice thermal conductivity is

$$\kappa_l = -\frac{\vec{Q}}{\vec{\nabla}_r T} = \frac{1}{3} \sum_{\vec{q}} \hbar \omega_{\vec{q}} v_g^2 \tau_q \frac{\partial n^0_{\vec{q}}}{\partial T} \tag{2.23}$$

Eq. 2.23 can be simplified using the assumptions of Debye theory. An average phonon velocity v_s (approximately equal to the velocity of sound in solids) is used to replace v_g, and the phonon velocities are the same for all polarizations. The summation can be replaced by the integral:

$$\kappa_l = \frac{1}{3} \int \hbar \omega_{\vec{q}} v_s^2 \tau_q \frac{\partial n^0_{\vec{q}}}{\partial T} g(\vec{q}) d\vec{q} \tag{2.24}$$

where $g(\vec{q})$ is the phonon density of states. For a 3D case $g(\vec{q})d\vec{q} = (3q^2/2\pi^2)dq$, and therefore $g(\omega)d\omega = (3\omega^2/2\pi^2 {v_s}^3)d\omega$ [36]. Using the Debye assumptions and Eqs. 2.19 and 2.24 leads to

$$\kappa_l = \frac{1}{2\pi^2 v_s} \int_0^{\omega_D} \hbar \omega^3 \tau_q(\omega) \frac{(\hbar\omega/k_B T^2) \exp(\hbar\omega/k_B T)}{(\exp(\hbar\omega/k_B T) - 1)^2} d\omega \tag{2.25}$$

where ω_D is the Debye frequency such that the total number of phonon modes equals to

$$3N = \int_0^{\omega_D} g(\omega) d\omega \tag{2.26}$$

Making the substitution $x = \hbar\omega/k_B T$ and defining the Debye temperature $\Theta_D = \hbar\omega_D/k_B$, Eq. 2.25 becomes

$$\kappa_l = \frac{k_B}{2\pi^2 \upsilon_s}\left(\frac{k_B}{\hbar}\right)^3 T^3 \int_0^{\Theta_D/T} \tau_q(x)\frac{x^4 e^x}{(e^x-1)^2}dx \tag{2.27}$$

Within the Debye approximation the differential lattice specific heat is

$$C(x)dx = \frac{3k_B}{2\pi^2 \upsilon_s^3}\left(\frac{k_B}{\hbar}\right)^3 T^3 \frac{x^4 e^x}{(e^x-1)^2}dx \tag{2.28}$$

Defining the mean free path of phonons as $l(x) = \upsilon_s \tau_q(x)$ [37], the lattice thermal conductivity can be written as:

$$\kappa_l = \frac{1}{3}\int_0^{\Theta_D/T} {\upsilon_s}^2 \tau_q(x) C(x)dx = \frac{1}{3}\int_0^{\Theta_D/T} C(x)\upsilon_s l(x)dx \tag{2.29}$$

2.4 Thermoelectric efficiency and figure of merit

A thermoelectric converter is a heat engine and like all heat engines it obeys the laws of thermodynamics. If we consider the converter operating as ideal generator in which there are no heat losses, the efficiency is defined as the ratio of the electrical power delivered to the load to the heat adsorbed at the hot junction:

$$\eta = \frac{\textit{energy delivered to the load}}{\textit{heat energy absorbed at hot junction}} \tag{2.30}$$

Conveniently the efficiency can be expressed as a function of the temperature over which it is operated and a so called "goodness factor" or thermoelectric figure of merit Z:

$$Z = \frac{S^2\sigma}{\kappa} \tag{2.31}$$

where S, σ and κ are the Seebeck coefficient, the electrical and the total thermal conductivity, respectively. The figure of merit is often expressed in its dimensionless form, ZT where T is absolute temperature.

The conversion efficiency as a function of operating temperature difference and for a range of values of the material's figure of merit is displayed in Fig. 2.4. Evidently an increase in temperature difference provides a corresponding

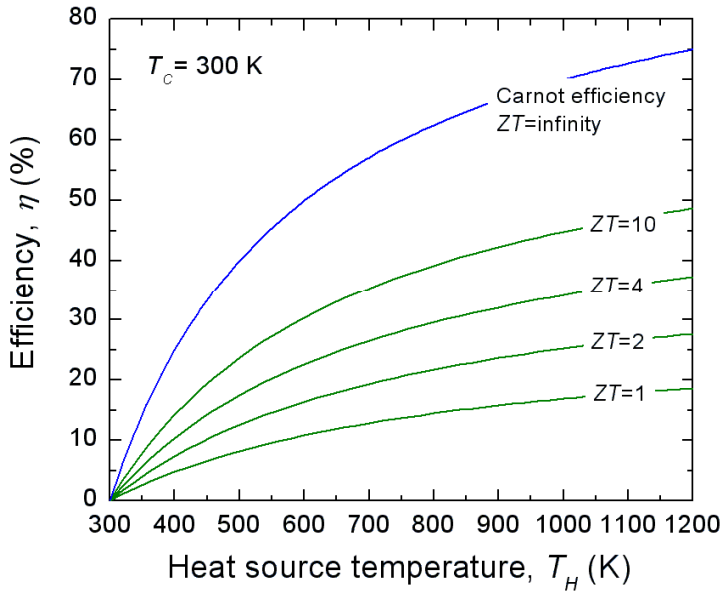

Figure 2.4: Generating efficiency as a function of temperature and material's ZT [4]

increase in available heat for conversion as dictated by the Carnot efficiency, so large temperature gradients are desirable. As a rough figure a thermocouple fabricated from thermoelectric materials with an average $ZT = 1.5$ would have an efficiency of around 10% when operated over a temperature difference of 500 K.

2.5 Directions of thermoelectric research

In recent years, it has been found convenient to introduce a quantity known as the power factor that contains both the Seebeck coefficient and the electrical conductivity. The power factor is defined as $S^2\sigma$ and is useful because S and σ are the parameters that are most strongly dependent on the electron transport properties. The other quantity that is involved in the definition of the figure of merit is the thermal conductivity, κ. κ is less dependent on the electron transport since in the promising thermoelectric materials (non-metals) it is often dominated by the lattice contribution, or phonon transport.

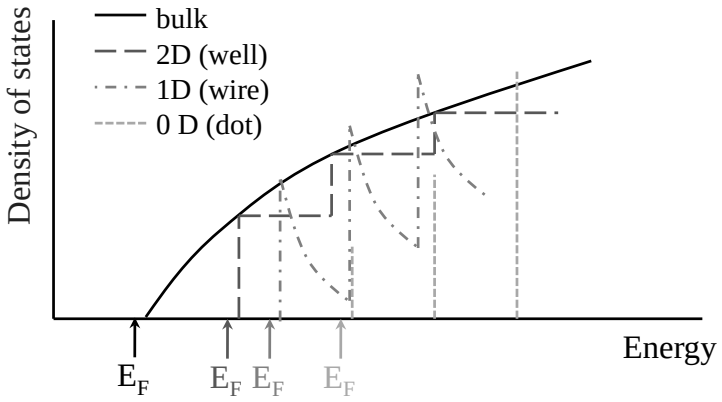

Figure 2.5: Electronic density of states for a bulk (3D), quantum well (2D), nanowire (1D), and quantum dot (0D) crystalline semiconductors [5]

2.5.1 Electron transport optimization

In Section 2.2 it was pointed out that for any typical 3D thermoelectric material there is always a trade-off between electrical conductivity and the Seebeck coefficient, which makes optimization of the power factor quite challenging. Currently there exist two alternative approaches to achieving enhanced power factor:

1) use of low dimensional systems

2) carrier energy filtering

2.5.1.1 Low dimensional thermoelectrics

In 1993 the outstanding pioneer work of Hicks and Dresselhaus [38] renewed interest in thermoelectrics, becoming the inspiration for most recent developments in the field. The key concept was that quantum confinement of in-plane carrier transport could substantially enhance the power factor over that of homogeneous materials, leading to ten-fold increase in ZT. Such enhancement could occur because sharp features in the electronic density of states of quantum-confined structures (see Fig. 2.5), enable a doping-level-tunable increase in the asymmetry between hot (electron energy is above the Fermi energy) and cold (electron energy is below the Fermi energy) electron transport, resulting in a large average transport energy and a large number of carriers moving in the material (i.e., a large Seebeck coefficient and electrical conductivity) [8].

A couple of years later and experimental investigation [6] found a good agreement with the theoretical predictions. The authors studied a multiple quantum wells (MQWs) system based on PbTe/$Pb_{1-x}Eu_xTe$ superlattice. Fig. 2.6 shows experimental and calculated results for S^2n as a function of well thickness, a, and as a function of carrier density, n. The mobility was assumed to be the same as the bulk value, and therefore was not considered in the analysis.

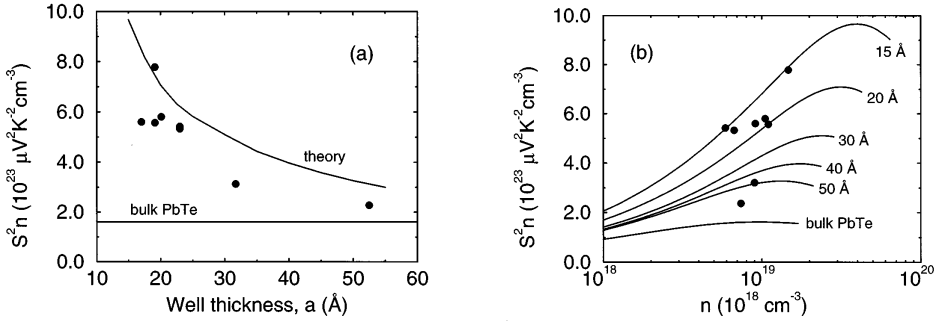

Figure 2.6: S^2n results for PbTe/$Pb_{1-x}Eu_xTe$ MQWs as a function of well thickness, a (left), and as a function of carrier concentration, n (right). Calculated results are shown as solid lines [6]

A few groups have also claimed quantum well enhanced Seebeck coefficients [7, 39, 40, 41, 42]. However, in some cases the apparent increase was an error due to inaccurate carrier concentration measurement [8]. Fig. 2.7 (left) shows the in-plane Seebeck coefficients measured in PbTe/PbSe nanodot superlattices (NDSL) and subsequently corrected measurements confirming that no Seebeck enhancement was observed (Fig. 2.7 (right))

Improving the thermoelectric power factor of quantum well materials is difficult for three reasons [9]. First, we live in a 3D world, and any quantum well structure should be embedded in barriers. These barriers are electrically inactive, but they add to the heat loss between the hot and the cold junctions. One cannot make the barrier too thin because the tunneling between adjacent quantum wells will broaden energy levels and reduce the improvement due to the density of states. Second, the sharp features in density of states of low-dimensional nanostructures disappear quickly as soon as there is size uniformity in the material.

Third, the number of conducting channels (found as carrier velocity times density of states) decreases as dimensionality decreases. Therefore, in order to realize the advantage of the power factor enhancement in low-dimensional nanostructures on the macroscopic scale, we must produce the same number of conductive channels in the area as is achieved in 3D. Calculations of Kim *et al.* [43] showed that for a device with 1×1 cm^2 in the cross-section and with 100% packing fraction, the thickness of the 2D films must be less than ~ 1.89 nm or the size of each nanowire must be less than $\sim 2.03 \times 2.03$ nm^2. In practice, nanowires or quantum wells are separated by barriers, i.e. the fill factor should be less than 1. For wires, the fill factor should be 1/4 to 1/3 to maintain their 1D properties.

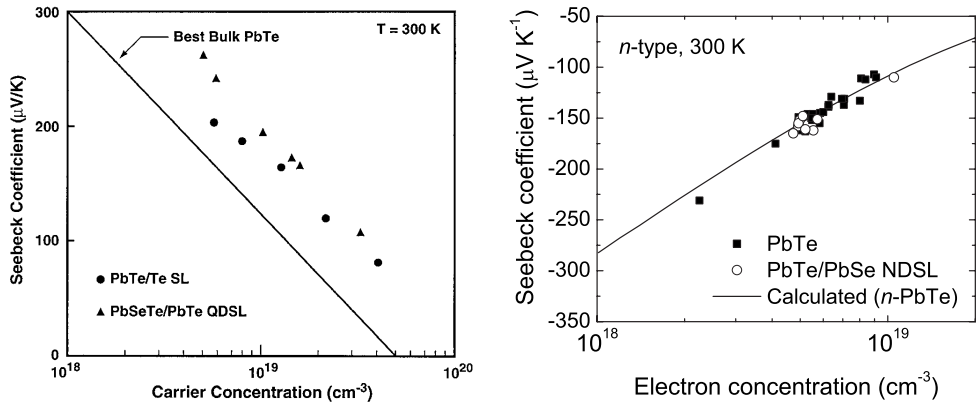

Figure 2.7: In-plane Seebeck coefficients of PbTe/PbSe NDSL (left) and subsequently corrected measurements showing no Seebeck enhancement [7, 8]

2.5.1.2 Carrier energy filtering

An alternative approach to achieving enhansed power factor is carrier energy filtering [10, 44]. By introduction of tall barriers ($\sim$1-10 $\times$ k_BT) in the conduction band (for n-type materials) or the valence band (for p-type materials), the higher-energy hot carriers can be selectively transmitted through the structure by filtering out the lower-energy carriers (Fig. 2.8). The asymmetry between hot and cold electron transport will increase, thereby overcoming the trade-off between the Seebeck coefficient and electrical conductivity.

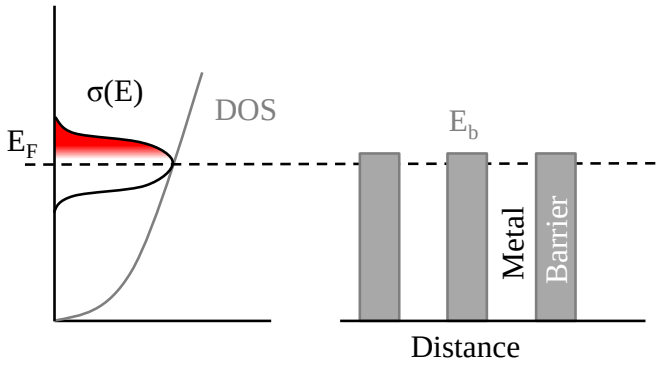

Figure 2.8: Density of states in the conduction band in a metal or highly degenerate semiconductor superimposed to the energy diagram of the multiple barriers vs. distance to show the principle of the electron filtering (selective emission of hot electrons) [9]

However, the simplistic picture in the energy space is misleading. One may think that all hot electrons with energies larger than the barrier height are transported above the barrier. However, if we look at electronic states on the momentum space (Fig. 2.9), we see that, with planar barriers, only electrons with kinetic energy in the direction perpendicular to the barrier higher than the threshold value are emitted. There are many hot electrons that have large transverse momentum. They cannot go above the barrier layer. The basic idea is that planar superlattices are momentum filters and not energy filters. In analogy with optics, we can say that these hot electrons have total internal reflection at the barrier interface, and they cannot be emitted [9].

The conservation of transverse momentum is due to symmetry of the system (translation invariance in the direction perpendicular to the barrier layers). Using non-planar barriers or scattering centres, one can break this symmetry. The key requirement is to break the symmetry without a significant reduction in the electron mean free path (electron mobility) in the structure. Thus it is important to have a low defect density and a high crystallinity near the interface. This could be achieved for instance with semimetallic nanoparticles endotaxially embedded into semiconductor alloys [45]. The main idea is that the Fermi level pinning at the nanoparticle/host matrix interface can be used to create 3D Schottky potential barriers which can selectively scatter hot electrons. Zebarjadi *et al.* [11]

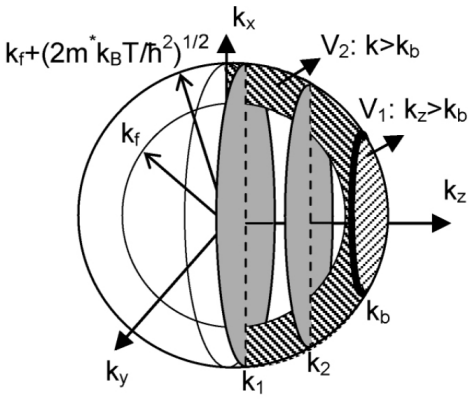

Figure 2.9: Electronic states in momentum space when the Fermi energy is deep inside the band (Fermi sphere) [10]

considered finite-size nanoparticles inside a host semiconductor and investigated their effect on the thermoelectric transport. The nanoparticle radius distribution followed Gaussian function with an average radius of 2 nm and variance of 0.7 nm. The barrier height was 0.1 eV. Fig. 2.10 shows the total scattering cross section per nanoparticle for different nanoparticle concentrations. It can be seen that, for low concentrations, electrons with energies close to the barrier height (0.1 eV) have the largest scattering cross section. At high nanoparticle concentrations, however, electrons see an overall potential distribution and do not see single barriers. Therefore the peak at 0.1 eV disappears in favour of a sharp increase at low energies. Such a sharp increase is an indication of the electron filtering. Low-energy electrons are blocked in this picture and high-energy ones contribute to the transport, and therefore the average energy transported per carrier (thermopower) increased.

These results were experimentally verified in InGaAlAs embedded with ErAs nanoparticles [11]. Nanoparticles randomly distributed inside the bulk matrix had sizes 2 nm to 3 nm and were epitaxially connected to the host. Fig. 2.11 shows the comparison between the prediction of the theory and the experimental data.

The model was able to reproduce electrical conductivity data quite accurately. The Seebeck coefficient, however, was off by as much as 15%. This difference came from the fact that the real potential of the nanoparticle is not known and that a

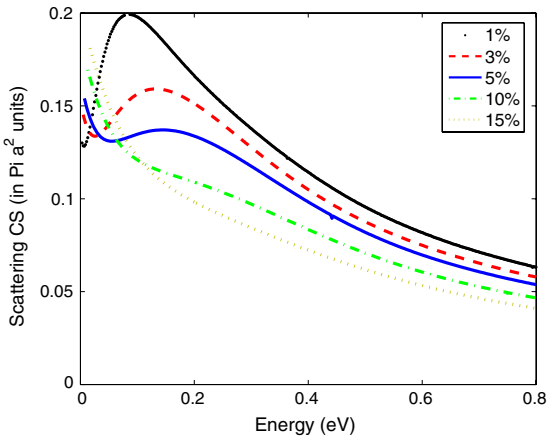

Figure 2.10: Total scattering cross section per nanoparticle inside a host semiconductor for different nanoparticle concentrations [11]

simplified model of the potential distribution around nanoparticles was used.

2.5.2 Phonon transport optimization

Although phonons do not contribute directly to the energy conversion, the reduction of their contribution to the thermal conductivity is a central issue in the thermoelectric research. It is known that the lattice thermal conductivity can be reduced by the scattering phonons on various types of defect, including the boundaries of any finite crystal. Such defects may, of course, scatter the charge carriers as well as the phonons. Indeed, since the mean free path is usually greater for electrons or holes than it is for phonons, we might expect there to be greater effect on the mobility than on the lattice conductivity. In practice, however, it turns out that, in many cases, the ratio of the mobility to the thermal conductivity can be raised through defect scattering.

2.5.2.1 Phonon defect scattering

In 1956 Ioffe *et al.* [46] suggested that the formation of a solid solution between two semiconductors that have the same crystal structure should lead to a reduction in the lattice conductivity. It was claimed that the mobility of the charge carriers would not necessarily be reduced by the alloying process. It was argued

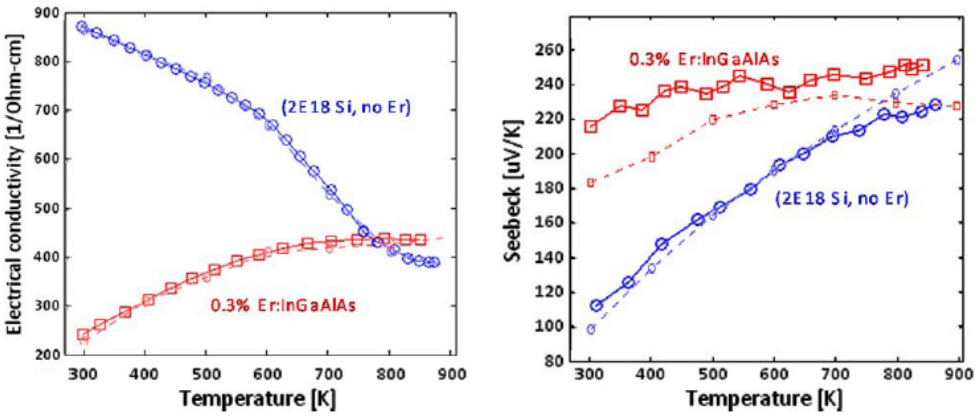

Figure 2.11: InGaAlAs embedded with ErAs nanoparticles. Comparison of the theory with the experiment [11]

that the long-range order would be preserved and, since the wavelength associated with the charge carriers is also rather large, they would suffer no additional scattering. On the other hand, the phonons that predominate in the conduction of heat have short wavelength and are scattered by the disturbances in the short-range order in a solid solution.

The effect of alloying is particularly large in the Si-Ge system because the lattice conductivity of pure silicon and germanium is so high that it is comparable with the total thermal conductivity of most metals ($\approx$ 150 W/mK). The thermal conductivity of $Si_{1-x}Ge_x$ is plotted in Fig. 2.12. The data points are labelled by the Ge concentration in atomic percent. The dashed line represents the thermal conductivity of pure Si. As we can see, the thermal conductivity of Si is decreased by a factor of ≈ 2 for a Ge concentration of 0.13 atomic percent [12].

Microstructural complexity is also responsible for the outstanding thermoelectric properties of $(AgSbTe_2)_{0.15}(GeTe)_{0.85}$ (TAGS) and $(AgSbTe_2)_x(PbTe)_{1-x}$ (LAST) compounds, which were first studied in the 1950s and have still remained some of the materials having highest known ZT. From early on it was predicted that lattice strain in TAGS could explain the low lattice thermal conductivities of 0.3 W m^{-1} K^{-1} [47]. Recent work points to the presence of twin-boundary defects in TAGS as an additional source of phonon scattering [48]. In LAST, Ag-Sb - rich nanoparticles 1 - 10 nm in size as well as larger micrometre-sized

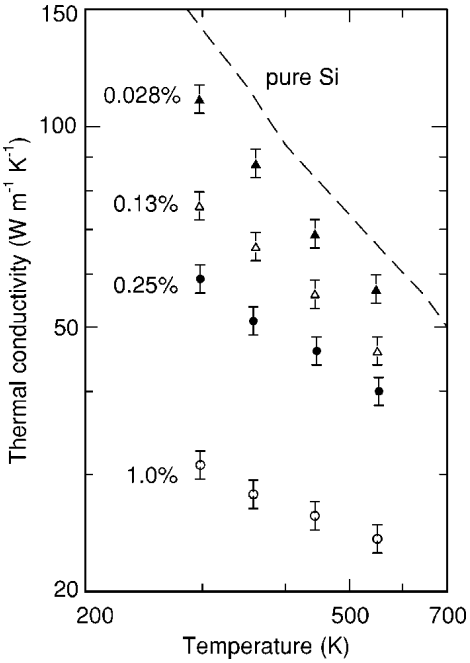

Figure 2.12: Thermal conductivity of epitaxial SiGe layers [12]

features precipitate from the bulk [13, 49, 50] (Fig. 2.13). The nanoparticles are coherent with the surrounding crystal matrix, therefore electronic conductivity is not significantly reduced. Conversely, the large density difference between the different regions leads to interfacial scattering of the phonons reducing the thermal conductivity. Through these mechanisms thermal conductivities of the order of 0.5 W m^{-1} K^{-1} at 700 K have been observed.

2.5.2.2 Phonon boundary scattering

It has long been known, since the pioneer work of Casimir [51] that phonons can be scattered on the boundaries of crystals at low temperatures. It was hard to observe this effect at ordinary temperatures, since the phonon mean free path decreases with temperature usually becoming less than 1 nm. Nevertheless, it was predicted in 1968 [52] that the lattice conductivity might be reduced by boundary scattering of the phonons for grain sizes of the order of 1 μm. The effect was observed for thin sheets of silicon in 1973 [53] and has since been found in other semiconductors.

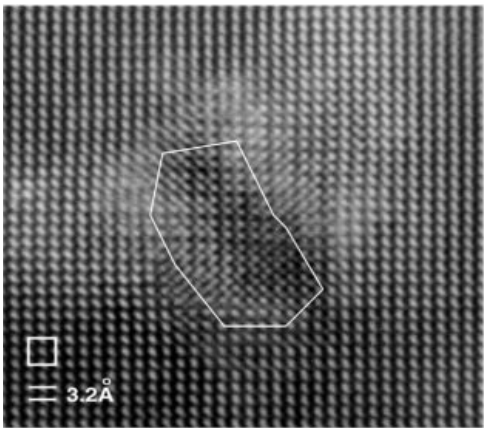

Figure 2.13: TEM image of a $AgPb_{18}SbTe_{20}$ sample. Ag-Sb - rich nanosized region (a "nanodot" shown in the enclosed area) is endotaxially connected to the Ag-Sb - poor surrounding structure [13]

Some early experimental data [54] indicate that the thermal conductivity of superlattices could be significantly reduced, especially in the cross-plane direction. Extensive experimental data on the thermal conductivity of various superlattices have been reported in recent years [55, 56, 57, 58, 59], mostly in the cross-plane direction. Impressive ZT values (~ 2.4) have been reported by Venkatasubramanian's group in Bi_2Te_3 / Se_2Te_3 superlattices at room temperature [59].

Aside from superlattices and thin films, other low-dimensional structures such as quantum wires and quantum dots are also being considered for thermoelectric applications. The experiments on silicon nanowires [14, 60] showed up to 100-fold reduction in thermal conductivity yielding to ZT values close to unity at room temperature. Hochbaum *et al.* [14] observed further reduction of the thermal conductivity in the nanowires with rough surface. Calculations of Martin *et al.* [15] showed that at low nanowire diameters the effect of surface roughness has a particularly strong effect resulting in a deviation from the linear diameter dependence ($\sim D$) to a scaling as ($\sim (D/\Delta)^2$), where Δ is the rms surface roughness. These predictions found excellent agreement with experimental values for the nanowires with diameters below 50 nm. Fig. 2.14 presents the thermal conductivity data for silicon nanowires prepared by two different routes: (a) typical vapour-liquid-solid (VLS) growth (rms Δ = 1-3 Å) and (b) synthesized by an aqueous electroless etching (EE) method (rms Δ = 3-3.25 nm)

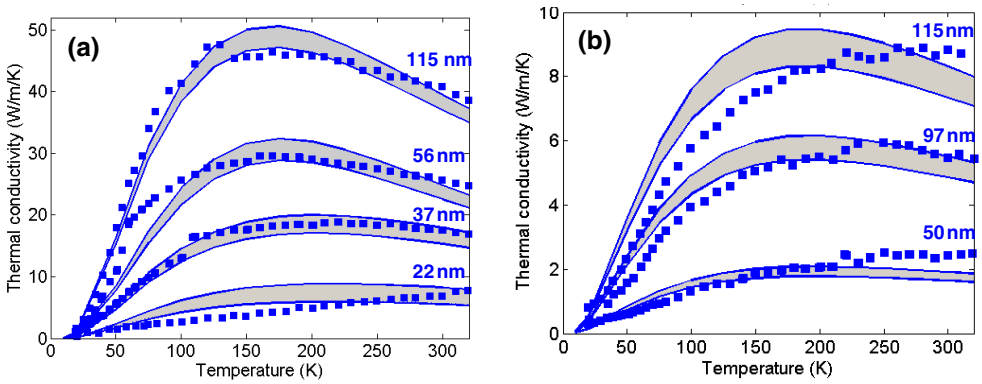

Figure 2.14: Thermal conductivity of (a) smooth VLS silicon nanowires (rms Δ = 1-3 Å) and (b) rough EE silicon nanowires (rms Δ = 3-3.25 nm). Shaded areas are theoretical predictions [14, 15]

A few experimental and theoretical studies on the thermal conductivity of quantum dot arrays [61, 62] and nanostructured porous media [16, 63, 64] have been also reported. Theoretical studies of Lee *et al.* [16] on ordered nanoporous silicon predicted the thermal conductivity reduction up to two orders of magnitude compared to the bulk monocrystalline silicon value. The thermal conductivity of this structure as a function of the pore diameter, d_p, and spacing between the pores, d_s, is presented in Fig. 2.15.

2.5.3 Phonon-Glass Electron-Crystal

In 1994 Slack introduced the concept of "phonon-glass electron-crystal" (PGEC) for the semiconductors which may prove superior for thermoelectric applications [65]. PGEC materials would posses electronic properties normally associated with good semiconductor but would have thermal properties normally associated with amorphous materials.

2.5.3.1 Skutterudites and Clathrates

Characteristics of crystals that have glass-like thermal conductivities were detailed by Cahill *et al.* [66]. They contain atoms that are loose in the sense that they do not have unique positions in the lattice. These loose atoms do not have

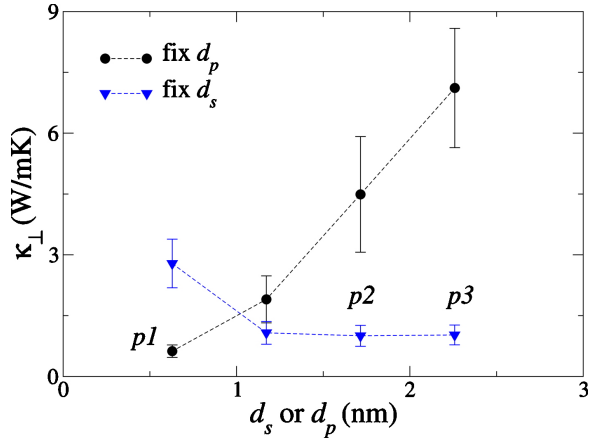

Figure 2.15: Room-temperature theoretical thermal conductivity of ordered nanoporous silicon for a case of fixed pore diameter (black circles) and fixed pore spacing (blue triangles) [16]

fixed positions relative to each other. The concentration of these atoms may be relatively high, at least 3%. The structures that can accommodate these loose atoms exhibit rather large open cages formed by more stable atoms. The so-called rattling motion of the loose atoms is responsible for intense phonon scattering and thus thermal conductivity reduction.

One class of such materials are scutterudites [67, 68, 69, 70, 71]. Skutterudite is the name first given to the mineral $CoAs_3$ discovered in a small Norwegian town Skutterud, and since then extended to other compounds with general formula MX_3 where M is Co, Rh, or Ir and X is P, As, or Sb. A key feature of the unit cell of skutterudite is that it contains empty spaces. In $CoSb_3$, the cobalt atoms form an almost cubic framework with square arrangements of each set of four antimony atoms, there being six such squares for every eight pseudo cubes. The voids that exist in such an arrangement can be occupied by loosely bound atoms that are known as "rattlers" (Fig 2.16). It is the rattlers that reduce the lattice conductivity to an extremely low level [35].

The clathrates are another group of compounds that have open structures into which loosely bound guest atoms can be incorporated [72, 73, 74, 75]. The original clathrates were crystalline complexes of H_2O with trapped atoms or molecules. Ice clathrates were known to have very small thermal conductivities. They typically

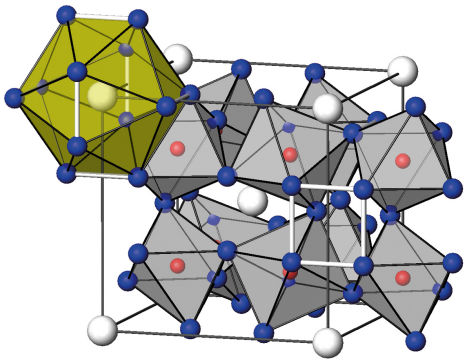

Figure 2.16: Schematic illustration of the skutterudite structure; red: Co atoms, blue: Sb atoms, white: guest ions; the big voids (yellow shaded) are filled with guest ions. Source: Chemnitz University of Technology

have a very large number of host atoms in the unit cell. These clathrates are electrical insulators but there are also clathrates with semiconducting properties.

Conducting clathrates have general formula $X_2Y_6E_{46}$ (Type I) or $X_8Y_{16}E_{136}$ (Type II) where X and Y are guest atoms on two different sites and E is Si, Ge, or Sn. The elements of Group IV of the periodic table are usually found to have the diamond structure, each atom being covalently bonded to four other atoms. These bonds are retained in the clathrates but there are no longer groups of four atoms forming tetrahedra. Instead, the Group IV atoms form dodecahedra and either tetrakaidecahedra or hexakaidecahedra. In Type I clathrates, the unit cell is made up of six tetrakaidecahedra and two dodecahedra, whereas in Type II clathrates, the cell comprises 16 dodecahedra and eight hexakaidecahedra. It is, therefore, possible for each unit cell in a Type I clathrate to accomodate eight guest atoms and in a Type II clathrate it can accommodate 24 guest atoms [35].

2.5.3.2 Oxides

Another method for circumventing the inherent materials conflict of a phonon-glass with electron-crystal properties is to use a complex material with distinct regions providing different functions. Likewise, the ideal thermoelectric material would have regions of the structure composed of a high-mobility semiconductor that provides the electron-crystal electronic structure, interwoven with a phonon-glass. The phonon-glass region would be ideal for housing dopants and disordered

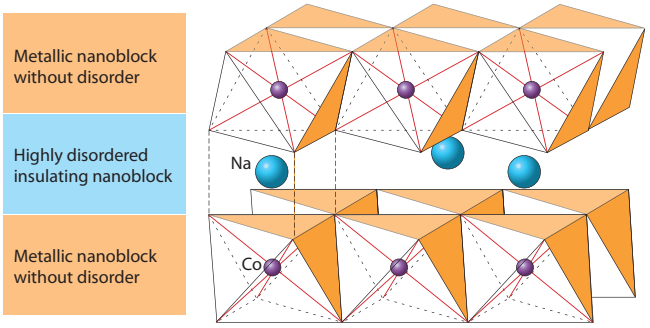

Figure 2.17: Crystal structure of Na_xCoO_2. Source: [17]

structures without disturbing the carrier mobility in the electron-crystal region. The electron crystal regions must be thin, on the nanometre or angstrom scale, so that phonons with a short mean free path are scattered by the phonon-glass region.

Such structure can be found in thermoelectric cobaltite oxides (Na_xCoO_2 and others such as those based on the Ca-Co-O system) [76, 77, 78]. The Co-O layers form metallic layers separated by insulating, disordered layers with partial occupancies (Fig. 2.17).

Oxides typically have low mobilities and high lattice thermal conductivities, due to the high electronegativity of oxygen and the strong bonding of light atoms, respectively. These properties give oxides a distinct disadvantage for thermoelectric materials. The success of the cobaltite structures as thermoelectric materials is an example how the microstructural duality for the electron and phonon transport overcomes these disadvantages.

These compounds are especially attractive for high-temperature applications as they are potentially stable and chemically inert.

2.5.3.3 Half-Heusler compounds

The basic Heusler alloy Cu_2MnAl is a ferromagnetic material with a structure in which Cu atoms form a primitive cubic lattice with alternative cells containing Mn and Al atoms. The half-Heusler structure is the same except that the atoms on the copper sites are missing. In the prototype half-Heusler compound, AgAsMg, the Mg and Ag atoms form a rock salt structure, and the As and either the Mg

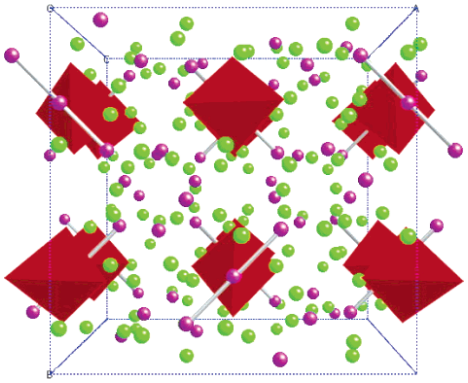

Figure 2.18: Crystal structure of $Yb_{14}MnSb_{11}$; green: Yb atoms, purple: Sb atoms, red polyhedra: $MnSb_4$ tetrahedra [18]

or Ag atoms form a zinc blend structure. A group of half-Heusler compounds with the formula MNiSn, where M = N, Zr, or Ti, is known to have good n-type thermoelectric properties even though the lattice conductivity is rather high.

A typical half-Heusler coumpound, ZrNiSn, has a lattice conductivity that is equal to about 10 W m^{-1} K^{-1}, but this can be reduced by forming a solid solution such as $Zr_{0.5}Hf_{0.5}NiSn$ [79]. The prospects for improvement are good since the charge carriers mobility is rather small and not likely to be reduced much when attempts are made to reduce the lattice conductivity still further.

Many of the half-Heusler compounds, such as ZrNiSn, HfNiSn, and TiNiSn, normally display n-type conduction but others including HfPtSn and ZrPtSn are p-type conductors [80]. However, the latter have rather low values for the electrical conductivity with ZT less than 0.03 at all temperatures.

2.5.3.4 Zintl phase compounds

Zintl compounds have recently emerged as a new class of thermoelectrics [81] because they can form quite complex crystal structures. A Zintl compound contains a valence-balanced combination of both ionically and covalently bounded atoms. The ionic cations donate electrons to the covalently bound anionic species. The covalent bonding allows higher mobility of the charge carriers that found in purely ionic materials. The combination of the bonding types leads to complex structures with the possibility of multiple structural units in the same struc-

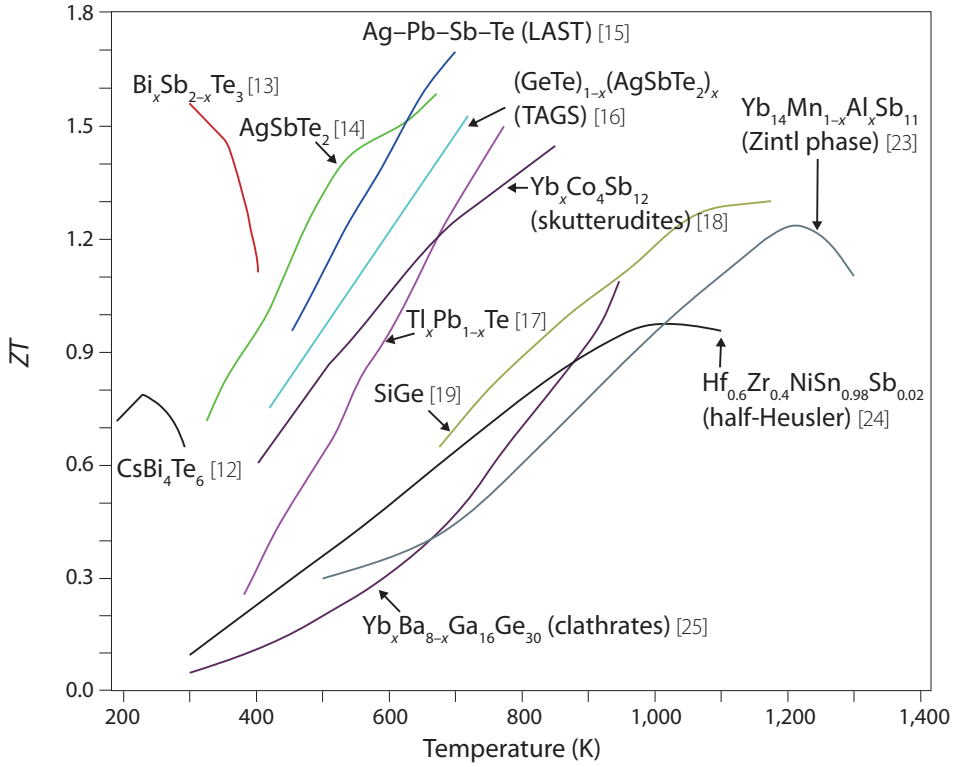

Figure 2.19: Figure of merit (ZT) of recent high-performance bulk thermoelectric materials [17]

ture. One example is $Yb_{14}MnSb_{11}$ [18, 81], which contains $[MnSb_4]^{9-}$ tetrahedra, polyatomic $[Sb_3]^{7-}$ anions, as well as isolated Sb^{3-} anions and Yb^{2+} cations (Fig. 2.18). This structural complexity, despite the crystalline order, enables extremely low lattice thermal conductivity (0.4 W m^{-1} K^{-1} at room temperature).

Combined with large Seebeck coefficient and high electrical conductivity, $Yb_{14}MnSb_{11}$ results in a ZT of ~ 1 at 900°C. This ZT is nearly twice that of p-type SiGe used in NASA spacecraft and has led to rapid acceptance of $Yb_{14}MnSb_{11}$ into NASA programmes for development of future thermoelectric generators [82].

Fig. 2.19 presents the recent data on high performance bulk thermoelectric materials summarizing the systems described above [17].

Chapter 3

Thermoelectric characterization

The measurement of the thermoelectric properties of a material presents some special problems. In early stages of the development of new material, a high accuracy may not be needed, but, once it is to be used in practical applications, these quantities must be known precisely. The performance is strongly dependent on the figure of merit, Z, which itself involves three other parameters, the square of the Seebeck coefficient, the electrical conductivity, and the thermal conductivity.

It is, generally, preferable for all the measurements to be made on a single sample. There are examples in the literature where falsely optimistic predictions have been made about potential new thermoelectric materials on the basis of data obtained from different specimens. It is understandable how such problem arises. The electrical conductivity is best found for a square sample with Van der Pauw geometry [20] of the electrical contacts. On the other hand, a long sample with a small cross-sectional area is preferred for the Seebeck measurements since this minimizes possible errors due to non-linear heat flow near the contacts. When the use of different samples from a given ingot is unavoidable, it is recommended that several pieces be cut and that the determination of, say, electrical conductivity of one piece be accompanied by the Seebeck measurements for neighbouring pieces on either side.

It is helpful in the basic study of a material to extend the measurements to cover the Hall effect, which gives not only a direct measure of charge carrier density and mobility, but can also provide with a useful information concerning impurities, imperfections, ununiformity, scattering mechanisms, etc. which is not

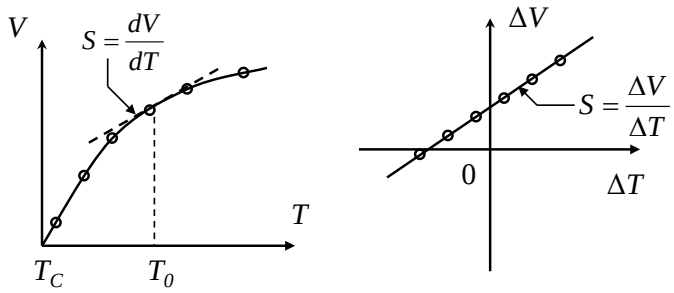

Figure 3.1: Seebeck coefficient measurements: integral method (left), differential method (right)

available from any other single technique [83].

The following section provides a description of the measurement techniques implemented in this work.

3.1 Measurement techniques

3.1.1 Seebeck coefficient

The two basic techniques for measuring Seebeck coefficients are the integral and the differential methods [84], see Fig. 3.1

In the integral method, one end of the specimen is held at a fixed temperature (generally 0°C) and the other end is varied through the temperature range of interest. The Seebeck coefficient at a selected temperature point can be obtained from the slope of the Seebeck voltage versus temperature, i.e., $S = dV(T)/dT$, at that point of the curve (Fig. 3.1 (left)). Large thermal gradients are an inherent feature of this method. In the differential method, a small thermal gradient ΔT is applied across a specimen which gives rise to a Seebeck voltage $\Delta V(T)/\Delta T$. For accurate measurements the value of ΔT is kept small and is varied about the selected temperature of measurement. Measuring $\Delta V(T)$ at several ΔT's avoids the assumption that the curve passes through the origin.

The accurate measurement of the Seebeck coefficient is simple in concept but complex in practice. Two of the major experimental problems encountered are (i) the presence of small spurious emfs generated in the measuring circuit and (ii)

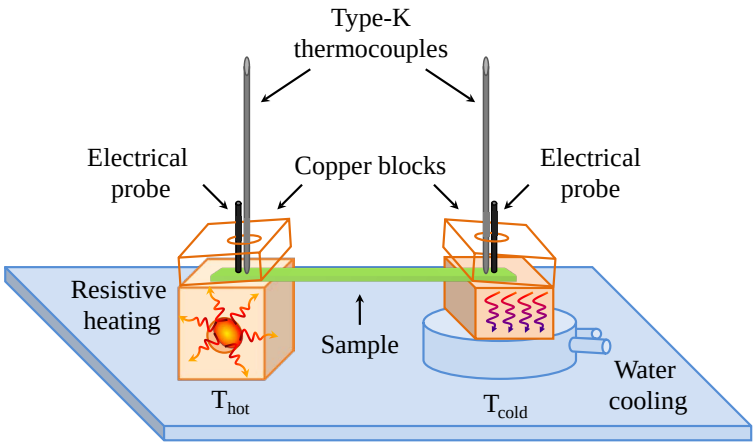

Figure 3.2: Schematic illustration of the experimental setup for room temperature Seebeck measurements

the difficulty of measuring the temperature and Seebeck voltage at exactly the same point of the specimen [85].

Experimental techniques based on the differential method are well covered in literature [86, 87, 88, 89]. Differential method using a pointed hot probe for determining the Seebeck coefficient of bulk specimens has been reported by several workers. One of the earliest reports was done in 1962 by Cowles and Dauncey [90] who used a copper hot probe with a thermocouple soldered to its end. The hot probe, heated externally using resistive heaters, was pressed on the sample resting on a huge brass block, which acted as a heat sink. The electrical contact between the thermocouple and the hot probe may lead to spurious results. This was avoided by Goldsmid who modified the apparatus of Cowles and Dauncey by isolating the thermocouples from both the probe and heat sink [91].

In comparison, fewer papers are available on the integral method. Wood *et al.* [85] described a setup that measures Seebeck voltages using the integral method in which the sample was pressed between a resistance-heated molybdenum furnace and a water cooled copper plate. Kumar and Kasiviswanathan [92] developed a setup that measures the Seebeck voltage of thin wires and thin films in the temperature range of 300 - 650 K by employing localized heating using the hot probe, which also acts as the voltage measuring lead. The hot and cold probes had in-built thermocouples which with proper calibration enabled the accurate

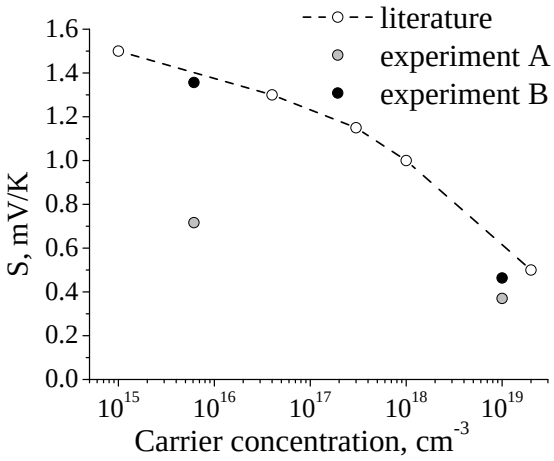

Figure 3.3: The Seebeck coefficient of silicon at room temperature as a function of the doping concentration. Comparison of our experimental results with those reported in the literature [19]

measurement of the temperature of the hot and cold points on the samples.

3.1.1.1 Apparatus for room temperature measurements

We have first developed a basic apparatus for the room temperature Seebeck measurements using the integral method. The experimental setup consisted of a sample holder with two copper blocks serving as a heat source and a heat sink, two type-K thermocouples and two electrical probes installed to measure the temperature gradient over the specimen and the resulting Seebeck voltage. The thermocouples were electrically insulated from the sample. The heat sink was water cooled and held at room temperature while the heat source was varied through the range of temperatures up to 100°C by means of a resistance heater (Fig. 3.2). The data was acquired by a Keithley® 2700 digital voltmeter equipped with a voltage scanning card (Keithley® data acquisition system, Model 7702). The temperature control was performed manually.

We developed a LabView program in order to control the data acquisition. The program details are given in Appendix A.

We performed the test measurements of commercially available silicon wafers with different concentration of the dopant and compared our data with those

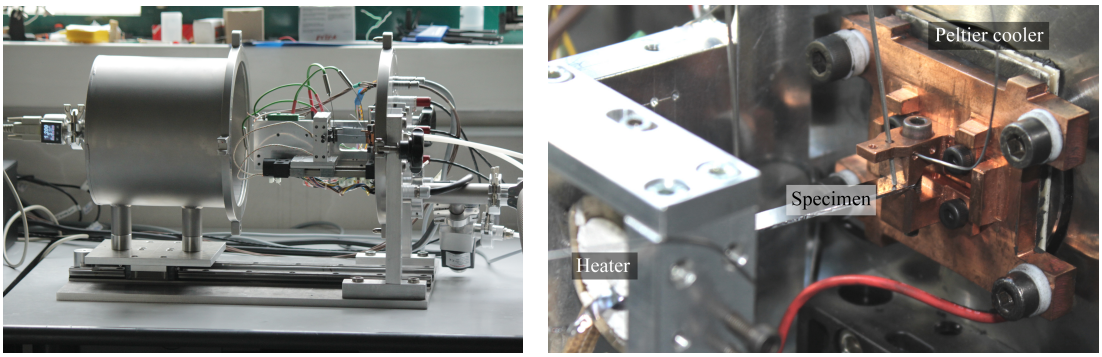

Figure 3.4: Experimental setup for high temperature Seebeck measurements (left) with a closer look to the sample holder (right)

reported in the literature [19]. The results are summarised in Fig. 3.3.

First, the temperature gradients and resulting Seebeck voltages were measured continuously upon the heating/cooling cycle (experiment A). The resulting Seebeck coefficients were found to be lower than those given in the literature. This problem was solved by switching to the steady measurement conditions when the data were collected upon stabilization of the system at the given temperature points (experiment B). In this case we found a much better agreement with the literature data.

3.1.1.2 Apparatus for high temperature measurements

For the high temperature Seebeck measurement we developed an improved setup (Fig. 3.4(left)). In order to decrease radiation losses at high temperature and thus improve the accuracy of the temperature control, the measurements were carried out in vacuum. The vacuum chamber was made of grade 304 stainless steal [93] commonly used for vacuum applications and was equipped with an oil rotary vacuum pump (Ing. Brizio Basi C.®). The sample was sandwiched by a pair of copper pincers, which also served as the heat source and the heat sink (Fig. 3.4(right)). Like in the earlier setup for the room temperature Seebeck measurements we implemented the integral method. For the heating we used a Ni-Cr 80/20 alloy strip mounted inside a mould made of grade 310 stainless steal [94] meant for high temperature service. The strip had length, width and

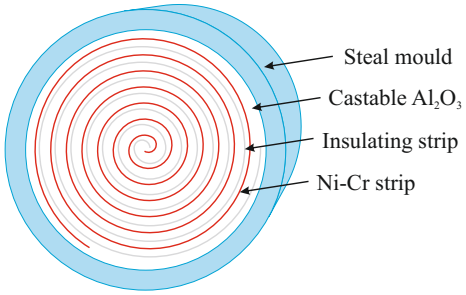

Figure 3.5: Schematic illustration of the heating element in the experimental setup for high temperature Seebeck measurements

thickness of 100, 2 and 0.3 mm, correspondingly, and the total resistance of 2.2 ohm. The coils of the strip were first electrically insulated from each other by insulating strips; the structure was then fixed and insulated from the mould by Al_2O_3 castable ceramics (Fig. 3.5). For the cooling we used a commercial Peltier cooler which was able to dissipate up to 150 W. Both the heater and the cooler were mounted at the rear of the pincers (see Fig. 3.4(right)). The temperature control was performed by means of Eurotherm® 3504 advanced temperature controller which allowed simultaneous communication with the heat source and the heat sink. We used a Keithley® 2700 digital voltmeter equipped with a voltage scanning card (Keithley® data acquisition system, Model 7702) to read the temperature of the hot and cold sides and the resulting Seebeck voltage. A LabView program was used to control the temperature and the data acquisition.

3.1.2 Electrical conductivity

The electrical resistance, R, of a metal or semiconductor specimen can be found by passing a known current through it and observing the potential difference between the ends. The electrical conductivity, σ, is equal to A/Rl, where l is the length of the wire and A is the cross-section area. In the case of semiconductors one should also take into account a resistance associated with the contacts. The conventional way to overcome this problem involves four-point probe methods. Typical arrangements of the probes are shown in Fig. 3.6

When the linear arrangement (Fig. 3.6(a)) is used, an electric current is passed

between the outer probes and the potential difference is measured between the inner probes.

For bulk samples where the sample thickness $t \gg s$, the probe spacing, a spherical protrusion of current emanating from the outer probe tips is assumed and the differential resistance can be found as:

$$\Delta R = \rho \frac{dx}{A} \tag{3.1}$$

Integrating between the inner probe tips (where the voltage is measured) we will get:

$$R = \int_{x_1}^{x_2} \rho \frac{dx}{2\pi x^2} = \frac{\rho}{2\pi}\Big(-\frac{1}{x}\Big)\Big|_{x_1}^{x_2} = \frac{1}{2s}\frac{\rho}{2\pi} \tag{3.2}$$

Due to the superposition of current at the outer two tips, $R = V/2I$. Thus, we arrive at the expression for bulk resistivity [95]:

$$\rho = 2\pi s \frac{V}{I} \tag{3.3}$$

For a very thin layer (thickness $t \ll s$) we get current rings instead of spheres. Therefore the expression for the area $A = 2\pi x t$. The derivation is as follows:

$$R = \int_{x_1}^{x_2} \rho \frac{dx}{2\pi x t} = \int_{s}^{2s} \frac{\rho}{2\pi t}\frac{dx}{x} = \frac{\rho}{2\pi t}\ln(x)\Big|_{s}^{2s} = \frac{\rho}{2\pi t}\ln 2 \tag{3.4}$$

Consequently, for $R = V/2I$, the sheet resistivity for a thin sheet is:

$$\rho = \frac{\pi t}{\ln 2}\frac{V}{I} \tag{3.5}$$

As we can see, this expression is independent of the probe spacing s. In general, the sheet resistivity $R_s = \rho/t$ can be expressed as:

$$R_s = k\frac{V}{I} \tag{3.6}$$

where the factor k is a geometric factor. In the case of a semi-infinite thin sheet, $k = 4.53$, which is just $\pi/\ln 2$ from the derivation. The factor k will be different for non-ideal samples [95].

The square arrangement (Fig. 3.6(b)) has the advantage that it occupies less

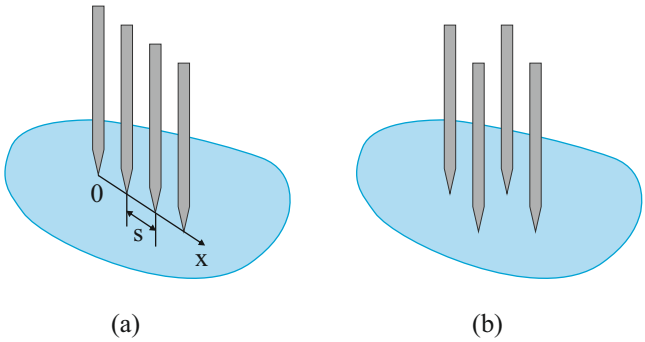

Figure 3.6: Four-point probe configurations; (a) probes regularly spaced in line and (b) probes at the corners of a square

space and it can, therefore, be used for smaller samples. In this configuration, the current is passed between adjacent probes and the potential difference between the other pair of probes is measured. This contact arrangements is used in the van der Pauw method [20].

Van der Pauw method

The power of this method in its ability to accurately measure the properties of a sample of any arbitrary shape, as long as the sample is approximately two-dimensional (i. e. the sample thickness must be much less than its width and length).

The measurements require that four ohmic contacts be placed on the sample. Certain conditions for their placement need to be met:

(i) They must be on the boundary of the sample (or as close to it as possible).

(ii) They must be infinitely small (or as small as possible).

The reason for that is to reduce errors which are introduced when the contacts are of finite size and not on the boundary of the sample. In Fig. 3.7(a) is presented the case in which one of the contacts is of finite length d and it is assumed to lie on the boundary of the sample. The other contacts are infinitely small and located at the boundary. The diameter of the sample will be denoted by D. In this case the order of magnitude of the error is approximately found as [20]:

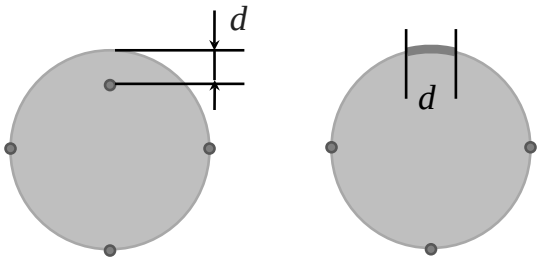

Figure 3.7: Special cases of the electrical contacts geometry which introduce errors in the resistivity measurement; (a) contact is of finite length and (b) contact lies at a distance from the boundary

$$\frac{\Delta\rho}{\rho} \approx -\frac{d^2}{16D^2 ln2} \tag{3.7}$$

In Fig. 3.7(b) is shown the case in which one contact lies at a distance d from the boundary of the sample. In this case we obtain [20]:

$$\frac{\Delta\rho}{\rho} \approx -\frac{d^2}{2D^2 ln2} \tag{3.8}$$

The influence of the contacts can be eliminated still further by using a "clover-shaped" sample as shown in Fig. 3.8.

In his paper, van der Pauw showed that the sheet resistance of samples with arbitrary shapes can be determined from two resistances - one measured along a horizontal edge, such as $R_{AB,CD}$, and a corresponding one measured along a vertical edge, such as $R_{AD,BC}$. The actual sheet resistance is related to these resistances by the van der Pauw formula:

$$\exp^{-\pi R_{AB,CD}/R_s} + \exp^{-\pi R_{AD,BC}/R_s} = 1 \tag{3.9}$$

Since $R_{AB,CD} = R_{CD,AB}$ it is possible to obtain a more precise value for the resistances $R_{AB,CD}$ and $R_{AD,BC}$ by making two additional measurements of their

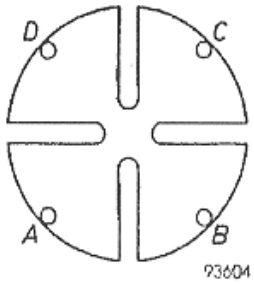

Figure 3.8: The "clover-shaped" sample where the influence of the contacts has been reduced considerably [20]

reciprocal values $R_{CD,AB}$ and $R_{BC,AD}$ and averaging the results. We define

$$R_{horizontal} = \frac{R_{AB,CD} + R_{CD,AB}}{2}, \tag{3.10}$$

$$R_{vertical} = \frac{R_{AD,BC} + R_{BC,AD}}{2} \tag{3.11}$$

Then the van der Pauw formula becomes

$$\exp^{-\pi R_{horizontal}/R_s} + \exp^{-\pi R_{vertical}/R_s} = 1 \tag{3.12}$$

A further improvement in the accuracy of the resistance values can be obtained by repeating the resistance measurements after switching polarities of both the current source and the voltage meter. Since this is still measuring the same portion of the sample, just in the opposite direction, the values of $R_{horizontal}$ and $R_{vertical}$ can be calculated as the averages of the standard and reverse polarity measurements. The benefit of doing this is that any offset voltages, such as thermoelectric potentials due to the Seebeck effect, will be cancelled out. Combining this method with the reciprocal measurements from above leads to the formula for the resistance being

$$R_{horizontal} = \frac{R_{AB,CD} + R_{CD,AB} + R_{BA,DC} + R_{DC,BA}}{2}, \tag{3.13}$$

$$R_{vertical} = \frac{R_{AD,BC} + R_{BC,AD} + R_{DA,CB} + R_{CB,DA}}{2} \tag{3.14}$$

The van der Pauw formula takes the same form as in Eq. 3.12

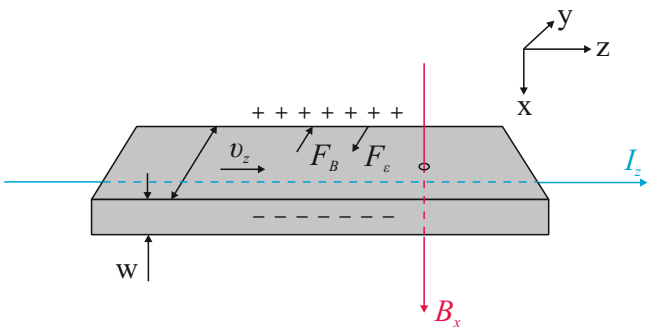

Figure 3.9: Schematic diagram to illustrate the Hall effect on a semiconductor sample

3.1.3 Hall measurements

The Hall effect has formed one of the essential characterization techniques throughout the history of semiconductor development. The reason is that for an extrinsic semiconductor it gives a direct measure of free carrier type and density which, when combined with a resistivity measurement on the same sample, also yields a value for the appropriate carrier mobility.

It is convenient to explain the physics of the classical Hall effect by reference to a uniform bar sample, as shown in Fig. 3.9. We consider a current of positive holes flowing from left to right under the influence of an applied electric field ε_z. A uniform magnetic induction B_x is also applied along the positive x direction (normal to the top surface) and this result in a force $F_B = eB_x v_z$ acting on the holes, tending to push them in the positive direction (according to Fleming's left hand rule), v_z being the hole drift velocity. The initial deflection of the positive charge towards the sample edge produces a transverse electric field ε_y which opposes the magnetic force and a steady state is reached when there is no transverse current (i.e. $J_y = 0$). This implies that the two forces are in balance, i.e.:

$$eB_x v_z = -e\varepsilon_y \tag{3.15}$$

The Hall field ε_y is proportional to both B_x and the current density J_z, so we may write:

$$-\varepsilon_y = R_H J_z B_x (J_y = 0) \tag{3.16}$$

where the proportionality constant R_H is known as the Hall coefficient. Rearranging Eq. 3.16, using Eq. 3.15 for ε_y and the relation $J_z = ep\upsilon_z$ allows us to write:

$$R_H = \frac{-\varepsilon_y}{B_x J_z} = \frac{\upsilon_z}{J_z} = \frac{1}{ep} \tag{3.17}$$

showing that a measurement of R_H gives a value for the hole density p.

The above argument is based on the assumption of a common drift velocity υ_z for all the carriers which is generally not true. For a sample at finite temperature T the charge carriers have a distribution of energies (and therefore of thermal velocities) spread over a few $k_B T$. In practice, it is necessary to take an average of υ_z over the energy distribution. This modifies Eq. 3.17 to:

$$R_H = \frac{r}{ep} \tag{3.18}$$

where the Hall scattering factor r lies between 1 and 2, depending on the details of the scattering processes which limit the drift velocity.

If we consider the corresponding case of an n-type semiconductor, the electrons would drift from right to left in Fig. 3.9 deflecting towards the same edge of the sample. Thus the Hall field is of opposite sign, i.e. it is negative for the same configuration of B_x and I_z and this provides an easy method of determining conductivity type in extrinsic material. The corresponding relation to Eq. 3.18 becomes:

$$R_H = -\frac{r}{en} \tag{3.19}$$

and the scattering factor is also different as it depends on the band structure of the conduction band which is usually very different from that of the valence band.

The practical evaluation of R_H depends on measuring the Hall voltage V_H, the current I_z, the magnetic induction B_x and the sample thickness w. Thus:

$$R_H = \frac{-\varepsilon_y}{B_x J_z} = \frac{V_H/h}{B_x I_z/wh} = \frac{V_H w}{B_x I_z} \tag{3.20}$$

V_H being positive for hole conduction and negative for electron conduction.

A Hall measurement is usually combined with one of resistivity. The electrical conductivity can be thus found as:

$$\sigma = \frac{J_z}{\varepsilon_z} \tag{3.21}$$

While the drift mobility is given by:

$$\mu = \frac{\sigma}{en} = -\frac{R_H \sigma}{r} \tag{3.22}$$

where we have used Eqs. 3.19, 3.20 and 3.21. The quantity $R_H\sigma$ is usually reffered as to the "Hall mobility" μ_H:

$$\mu_H = |R_H \sigma| = r\mu \tag{3.23}$$

and it is μ_H which is normally quated when analysing Hall effect and resistivity measurements, though one must always bear in mind that μ_H is generally slightly greater than the drift mobility μ [83].

Majority of Hall measurements are made in the van der Pauw geometry [20]. Like in the case of electrical conductivity, finite size contacts located away from the boundary of the sample cause the errors in determination of Hall mobility. for the case in which one of the contacts is of finite length d and it is assumed to lie on the boundary of the sample (Fig. 3.7(a)) the magnitude of the error is approximately found as [20]:

$$\frac{\Delta\mu_H}{\mu_H} \approx -\frac{2d}{\pi^2 D} \tag{3.24}$$

For the case in which one contact lies at a distance d from the boundary of the sample (Fig. 3.7(b)) we obtain [20]:

$$\frac{\Delta\mu_H}{\mu_H} \approx -\frac{2d}{\pi D} \tag{3.25}$$

Again, the influence of the contacts can be reduced further by using a "clover-

shaped" sample (Fig. 3.8).

Van der Pauw also showed that the Hall coefficient is given by:

$$R_H = \frac{w}{B_x}\Delta R_{AC,BD} \tag{3.26}$$

where $\Delta R_{AC,BD}$ is the change in $R_{AC,BD}$ produced by the applied magnetic field B_x ($R_{AC,BD}$ is measured using diagonal pairs of contacts rather than adjacent pairs (Fig. 3.8)). It is standard practice to reverse the current and magnetic field and interchange current and voltage arms, to obtain R_H from an average of eight readings [83].

Figure 3.10: Experimental setup for resistivity and Hall measurements

For the Hall measurements we used a home built system presented in Fig. 3.10. The experimental setup consisted of Leybold® refrigerator-cooled cryosystem in which helium compressor (1a) unit and cold head (1b) were separately installed and connected to each other via two flexible pressure tubings; a vacuum chamber (2) used as the thermostat, Leybold® LTC 60 Low Temperature Controller (3); Keithley® 705 Scanner equipped with Keithley® 7065 Hall Effect Card (4)

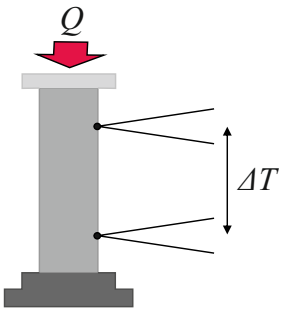

Figure 3.11: Schematic diagram of the experimental setup for steady-state thermal conductivity measurements

designed to assist in making resistivity and Hall measurements on semiconductor specimens; Keithley® 220 Programmable Current Source (5); Keithley® 196 System DMM (6); and the magnet generating magnetic fields up to 0.5 T (7).

3.1.4 Thermal conductivity

The accurate measurement of the thermal conductivity of a material can pose many challenges. For instance, loss terms of the heat input intended to flow through the sample usually exist and can be most difficult to quantify. There exist many methods for the determination of thermal conductivity, such as steady-state techniques, the 3ω technique, and the optical heating methods. Each of these techniques has its own advantages as well as its inherent limitations, with some techniques more appropriate to specific sample geometry. This will be discussed in detail in the following sections.

3.1.4.1 Steady-state method

Determination of the thermal conductance of a sample is a solid-state transport property measurement in which a temperature difference (ΔT) across a sample is measured in response to an applied amount of heating power (Fig. 3.11). This is a measure of the heat flow through the sample. The thermal conductivity κ is given by the slope of a power versus ΔT sweep at a fixed base temperature with the dimensions of the specific sample taken into account. The thermal conductivity is derived from a typical "steady-state" measurement method is

$$\kappa = \frac{Q_s L}{A \Delta T} \tag{3.27}$$

where κ is the total thermal conductivity, Q_s is the power flowing through the sample, L is the length between the thermocouples, ΔT is the temperature difference measured, and A is the cross sectional area of the sample through which the power flows.

However, determination of Q_s is not such a simple task. Typically, an input power, Q_{in}, is applied to one end of the sample, and the power through the sample is

$$Q_s = Q_{in} - Q_{loss} \tag{3.28}$$

where Q_{loss} is the power lost to radiation, heat conduction through gases or through the connection leads, or losses due to heat convection currents. The losses can be substantial unless sufficient care is taken in the design of the measurement apparatus and setup. These losses cannot be completely eliminated, but as stated an appropriate experimental design would include design considerations to minimize or sufficiently account for each loss term. For instance, proper thermal shielding and thermal anchoring are essential, while the thermocouple wires should be small diameter (0.25 mm) and posses low thermal conductivity, such as chromel or constantan wire. Heat loss through the connection wires of the input heater or the thermocouple leads can be calculated and an estimate obtained for this correction factor, which is typically less than 1-2 % in a good experimental design.

The steady-state thermal conductivity technique requires uniform heat flow through the sample; therefore, excellent heat sinking of the sample to the stable temperature base as well as the heater and thermocouples to the samples an absolute necessity. Insufficient thermal anchoring can be difficult to detect even by experienced researchers, therefore it is recommended to perform systematic checks measuring known standards and comparing values to rule out errors due to poor thermal anchoring [37].

The error in thermal measurements due to blackbody radiation is proportional to the third power of temperature and the reciprocal of the thermal conductance

of the sample. Assuming that (i) a radiation shield surrounds the sample; (ii) ΔT is small so that the radiation loss is proportional to ΔT; and (iii) the sample losses heat only from the side surfaces of the sample, not from the top and from the attached heaters and thermometers, the error in the measurement due to radiation $\frac{Q_{rad}}{Q}$ is found as

$$\frac{Q_{rad}}{Q} = \frac{8\varepsilon\sigma_{S-B}T^3}{\kappa}\left(\frac{l^2}{\sqrt{A}}\right) \tag{3.29}$$

where l and $\sqrt{A}$ is the sample length and the cross sectional area, respectively, σ_{S-B} is the Stephan-Boltzmann constant ($\sigma_{S-B} = 5.7 \times 10^{-8}$ W/m^2 K^4) and ε is the emissivity of the sample. The total emissivity of most dielectrics is close to one at temperatures near room temperature. For a sample with $l = 2.5$ cm and $A = 0.1$ cm^2 the error introduced by blackbody infrared radiation is approximately 15% for a-SiO_2 at 100 K. Radiation from the attached heaters and thermometers would increase the error [96].

The radiation error is greatly reduced by using the 3ω method.

3.1.4.2 3-omega method

Although initially developed for measuring the thermal conductivity of bulk materials, the method was later extended to the thermal characterization of thin films down to 20 nm thick [97, 98, 99, 100, 101, 102]. This technique is currently one of the most popular methods for thin-film cross-plane thermal conductivity characterization.

In this method a thin electrically conductive wire is deposited onto the specimen whose thermal conductivity needs to be measured. The wire functions as both a heater and a temperature sensor (Fig. 3.12). An AC current with angular modulation frequency ω is driven through the wire, causing Joule heating at a frequency 2ω. The generated thermal wave diffuses into the specimen and the penetration depth is determined by the thermal diffusivity of the specimen and the frequency of the AC current. Since the resistance of the heater is proportional to the temperature, the resistance will be modulated at 2ω. The resistance oscillation at 2ω multiplied by the excitation current at ω produces a voltage

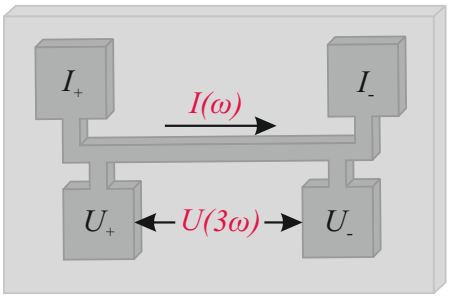

Figure 3.12: Schematic diagram of thermal conductivity measurements using the 3ω method

oscillation at 3ω. The amplitude of this 3ω voltage is measured by the lock-in amplifier. Hence is the name "3ω method".

The exact solution for the temperature oscillations at distance r from an infinitely narrow line source on an infinite half-volume $\Delta T(r)$ is given by Carslaw and Jaeger [103]:

$$\Delta T(r) = \frac{P}{l\pi\kappa} K_0(qr) \tag{3.30}$$

where κ is the thermal conductivity of the infinite half-volume and P/l is the amplitude of the power per unit length generated at a frequency 2ω in the line source of heat. K_0 is the zeroth-order modified Bessel function. The magnitude of the complex quantity $1/q$,

$$\frac{1}{q} = \sqrt{\frac{D}{i2\omega}} \tag{3.31}$$

is the wavelength of the diffusive thermal wave or what is called the thermal penetration depth. Here, D is the thermal diffusivity found as $\kappa/\rho C$, where ρ is the density and C is the specific heat.

In the limit $|qr| \ll 1$, Eq. 3.30 can be approximated by [97]

$$\Delta T(r) = \frac{P}{l\pi\kappa}\left(\frac{1}{2}\ln\frac{\kappa}{C(w/2)^2} - \eta - \frac{1}{2}\ln(2\omega) - \frac{i\pi}{4}\right) \tag{3.32}$$

where w and l are the width and the length of the heater, respectively, and η is the constant. The analytical solution gives $\eta = 0.923$ while the experiments on

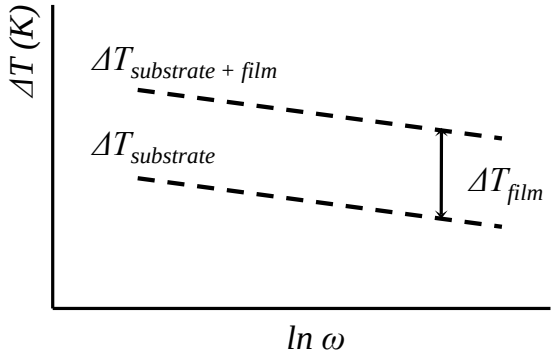

Figure 3.13: Amplitude of the temperature oscillation ΔT as a function of a frequency of drive current

a-SiO_2 and MgO substrates showed that $\eta = 1.05$ more accurately describes the experimental results [98]. Eq. 3.32 has been written to separate the frequency-dependent and the imaginary contributions to the solution. Either the real or imaginary part of the temperature oscillations ΔT can be used to determine the thermal conductivity. The imaginary part (out-of-phase oscillations) gives the thermal conductivity directly, but it was experimentally found by Cahill [97] that the slope of the real part (in-phase oscillations) versus $\ln \omega$ is a more reliable measure.

As it was mentioned earlier, the method can be also extended for cross-plane thermal conductivity measurements of thin films. Since the film thickness is usually less than the thermal penetration depth, the through-thickness heat transport in the film simply adds a frequency independent ΔT_{film} to the thermal response of the substrate $\Delta T_{substrate}$, see Fig. 3.13.

When the film thickness t is far smaller than the width of the heater w, heat flow in the film can be considered one-dimensional and the thermal conductivity κ_{film} of the layer can be found using [98]

$$\Delta T_{film} = \frac{P}{l\kappa_{film}} \frac{t}{w} \tag{3.33}$$

To calculate the heat lost to blackbody infrared radiation we will again assume that the radiation shield is held at temperature T, the average temperature of the sample. This assumption is mostly for convenience and does not greatly affect

our results. In the 3ω method heat is lost only from a small area on the surface of the sample; the area is the surface within the thermal penetration depth of the heater-thermometer. The radiation error in the 3ω method is

$$\frac{Q_{rad}}{Q} = \frac{8\varepsilon\sigma_{S-B}T^3}{\kappa}\left|\frac{1}{q}\right| \tag{3.34}$$

A thermal penetration depth of 30μm reduces the error due to radiation by a factor of approximately 10^4 compared to the standard geometry described in the previous section. This small thermal penetration depth can be achieved in a typical glass with a 5-μm-wide heater-thermometer and a rather modest heater frequency of a few hundred hertz. Even at 1000 K the calculate error due to radiation in this case is less than 2% [96].

An important factor in the accuracy of 3ω measurement is that the current should be confined to the metal strip resistor since any leakage to the substrate will invalidate the results. This is because the heat source would no longer be localized on the surface and also because any Schottky behavior at metal/semiconductor interface will create nonlinearities that affect the 3ω signal substantially [104]. On the other hand, presence of electrical insulation layer inevitably introduces an additional thermal resistance between the metal test pattern and the sample, which can reduce both the sensitivity and accuracy of the technique [105].

These problems can be solved by using the optical heating methods. Because in this case the temperature is measured optically, these methods are less dependent on the electrical properties of the metal heater. One of such methods, time-domain thermoreflectance, is described in the following section.

3.1.4.3 Time-domain thermoreflectance

Time-domain thermoreflectance (TDTR) technique allows determination of the temperature response ΔT through the change of the reflectivity ΔR of the sample such as:

$$\frac{\Delta R}{R} = \frac{1}{R}\frac{dR}{dT}\Delta T \tag{3.35}$$

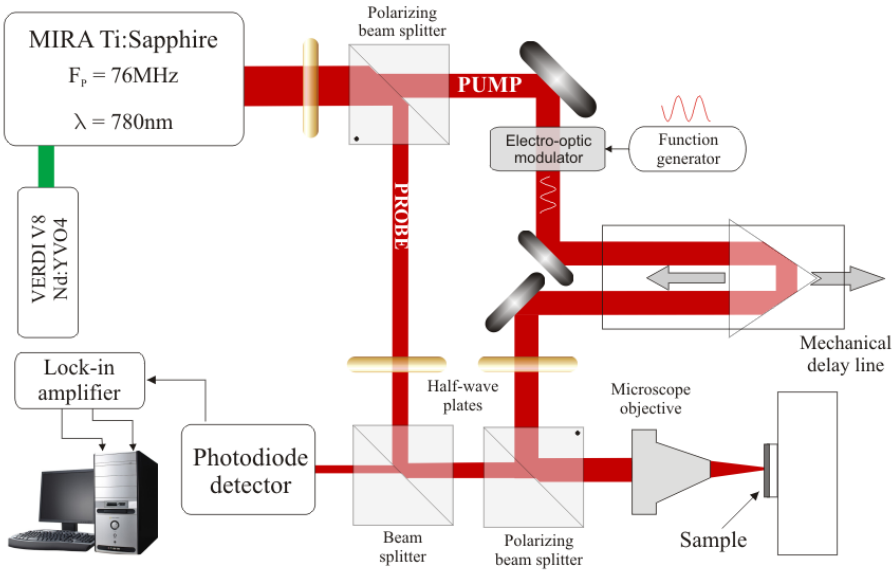

Figure 3.14: Schematic of the time-domain thermoreflectance (TDTR) setup for thermal conductivity measurements. Courtesy of G. Pernot

The example of TDTR experimental apparatus is presented in Fig. 3.14. In TDTR measurements, the output of a mode-locked laser is split into a pump beam and a probe beam. The pump beam is used to heat the sample and the probe beam is used to monitor the reflectivity variations of the surface. The temporal response of the sample is obtained by creating a delay between the pump and the probe beams by means of the mechanical delay line which modifies optical path of one of the beams. Because the variations of the reflectivity are weak ($\frac{1}{R}\frac{dR}{dT} \sim 10^{-3} - 10^{-5}$ [37]), the pump pulses are modulated in amplitude by an electro-optical modulator at frequency f, $0.1 < f < 10$ MHz. A thin layer ($\sim$ 80 nm) of metal with high thermoreflectance (e.g., Al) is deposited on the sample and serves as the transducer to absorb the heating pump beam and to convert the temperature excursions at the surface into changes in the intensity of the reflected probe beam. A photodiode and a lock-in amplifier are used to measure the small changes in the probe intensity that are created by the pump.

Thermal response of a single pulse is inferred from repetitive measurements of

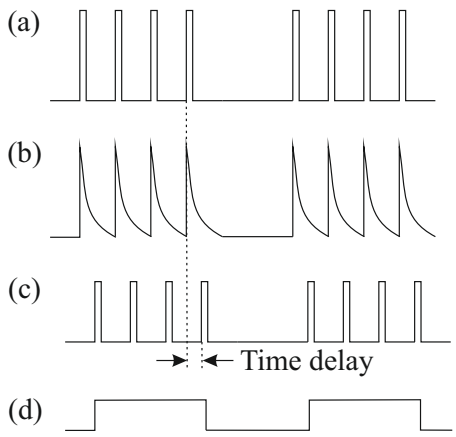

Figure 3.15: Illustration of time-domain thermoreflectance (TDTR) detection scheme

the probe response to many identical heating pulses. Fig. 3.15 explains the basic idea behind TDTR method. The mode-locked pulse lasers such as a Ti-sapphire laser produces a series of < 1 ps pulses at a repetition rate of $\sim$ 76MHz (Fig. 3.15 (a)). The thermal response of the sample, under the quasi-steady condition, is shown in Fig. 3.15 (b). Due to the temperature rise, there will be a small modulation in the reflected probe pulses falling in the period when the pump pulses are not blocked by the electro-optical modulator (Fig. 3.15 (c)). The photodetector averages over a number of the probe laser pulses (Fig. 3.15 (d)), and the small power variation in the time averaged reflectance signal is picked up by a lock-in amplifier. The amplitudes of the probe beam intensity variation at different delay times give the thermal response of the sample to the pulse train [37].

The changes in reflectivity intensity at frequency f have both an in-phase V_{in} and out-of-phase component V_{out}. Usually the ratio V_{in}/V_{out} is analysed to make use of the additional information in the out-of-phase signal and eliminate artefacts created by unintended variations in the diameter or position of the pump beam created by the mechanical delay line.

The thermal penetration depth of TDTR measurements d_{TDTR} is given by

$$d_{TDTR} = \sqrt{\frac{D_f}{\pi f}} \tag{3.36}$$

where $D_f = \kappa_f / C_f$ is the thermal diffusivity of the thin film, and κ_f and C_f are the thermal conductivity and the volumetric heat capacity of the film. For a film of $\kappa_f = 5$ W m^{-1} K^{-1}, $C_f = 1.5$ J cm^{-3} K^{-1} and $f = 10$ MHz, $d_{TDTR} \approx 300$ nm. Usually, the penetration depth in TDTR is much smaller than the $1/e^2$ radii of the laser beams of a several microns. Hence, heat flow in TDTR is predominantly one dimensional through the thickness of the film [105].

Data analysis in TDTR is more complicated than the 3ω method. Measurements of the ratios V_{in}/V_{out} as a function of delay time are compared to numerical solutions of a thermal model [106]. The thermal model normally has two free parameters: the thermal conductance of the Al/film interface and κ_f of the thin film. For most cases it is possible to separate these two parameters from the fitting of the model calculations to the measurements [107, 108, 109].

Chapter 4

Thermoelectric properties of polycrystalline silicon films with and without nanocavities

This part of the work was performed in collaboration with the group of Prof. Giampiero Ottaviani in the University of Modena.

4.1 Introduction

In Chapter 2 we discussed the effect of nanostructuring on material's thermoelectric properties. Theoretical studies of Lee *et al.* [16] on ordered nanoporous silicon predicted the lattice thermal conductivity reduction up to two orders of magnitude (see Section 2.5.2.2) compared to the bulk monocrystalline silicon value. Computation of the remaining thermoelectric transport coefficients showed that the electrical conductivity, σ, of such structure would decrease by a factor of 2-4, depending on doping levels while the Seebeck coefficient, S, would yield a two-fold increase for carrier concentrations less than 2 $\times 10^{19}$ cm $^{-3}$, above which S would remain close to the bulk value. Combining these results with the calculations of the lattice thermal conductivity, κ, the authors predicted the figure of merit ZT to increase by two orders of magnitude over that of bulk [110].

We have performed an experimental investigation of thermoelectric proper-

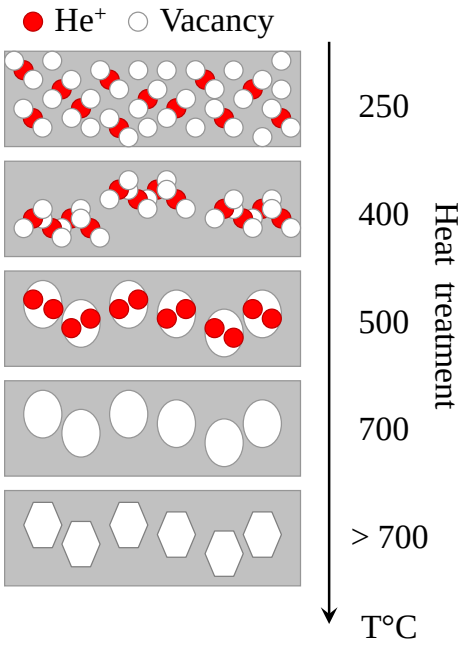

Figure 4.1: Schematic illustration of the nanocavities formation in silicon [21]

ties of a somewhat similar structure: polycrystalline silicon films with embedded nanocavities.

Nanocavities (NCs) can be easily formed in silicon by high-dose ion implantation of light ions (He, H) and subsequent thermal annealing. Helium presents many advantages with respect to other light ions. Due to its high permeability it diffuses easily through the silicon and from the surface. Being an inert gas, it does not interact with the host atoms or other species, so that no impurity is left in the wafer and chemical interactions are avoided. Finally, due to the very low solubility of helium in crystalline silicon it does not dissolve into the lattice, as many other gases would do. Helium bubble formation is a quite complex phenomenon and involves a sequence of independent steps [21, 22, 111, 112] (Fig. 4.1).

Upon implantation, He is repealed by vacancies and forced to an enhanced diffusion during implantation. Helium atoms are instead trapped by divacancies stabilizing them and favouring their evolution into more complex He_n-V_n clusters at annealing temperature T_a up to 400°C. The silicon atom displaced during

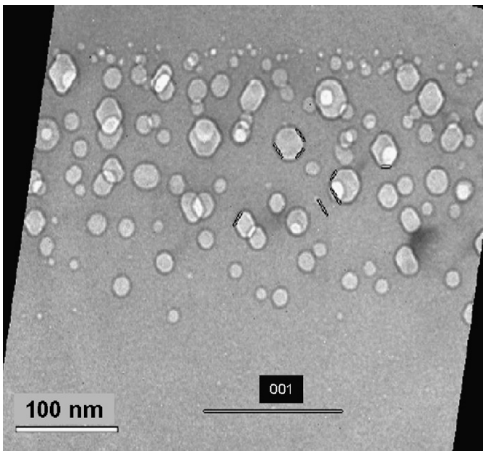

Figure 4.2: TEM image of a silicon region with embedded nanocavities formed by annealing of silicon implanted with helium at 950°C for 2 hours [22]

implantation recombine at the surface in the same range of temperatures. The result is a supersaturation of vacancies in the silicon bulk, contrary to what happens in the case of ion implantation and annealing of common substitutional impurities (i.e., a supersaturation of self-interstitials) [21]. For $455 < T_a \leq 570$°C a coalescence process between cavities located near the center is observed. When the cavities completely merge, a planetary-like structure is formed [112]. Helium remains stable up to $\sim$ 450°C, a loss occur at higher annealing temperatures and it becomes almost undetectable at $T_a = 700$°C [111]. Annealing at higher temperatures result in modification of the morphology of the NCs surface [22]. In Fig. 4.2 is presented TEM image of a silicon region with embedded NCs formed by annealing of silicon implanted with helium at 950°C for 2 hours. NCs in an amount of 1.1×10^{11} cm^{-2} were almost uniformly distributed inside the zone and had the mean diameter of 20 nm [22].

4.2 Experimental details

Polycrystalline 450-nm thick silicon films were deposited on top of a silicon oxide insulating layer and were then heavily implanted with boron at fluence of 2×10^{16} cm^{-2}. After that, the samples underwent a rapid thermal annealing at 1050°C in Ar + 5% O_2 for 30 seconds in order to electrically activate the dopant. The

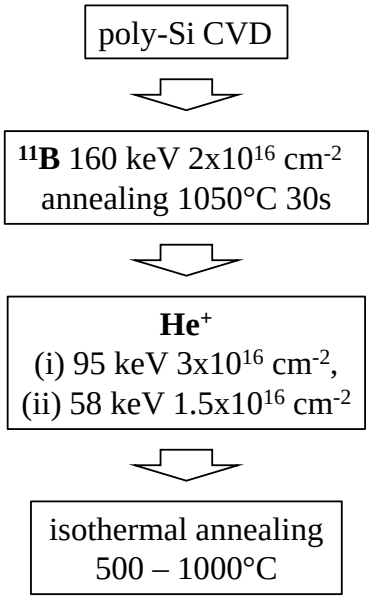

Figure 4.3: Schematics of the experimental procedure used for preparation of polycrystalline silicon films with embedded nanocavities

average boron concentration, 4.4×10^{20} cm^{-3}, was larger than boron kinetic solubility at the same temperature (2×10^{20} cm^{-3} [113]). The samples were then implanted with helium. In order to obtain a nearly uniform helium concentration inside the polysilicon layer the implantation was performed in two steps: first with a dose 2.97×10^{16} cm^{-2} of He$^+$ ions at energy of 95 keV and then with a dose 1.5×10^{16} cm^{-2} of He$^+$ ions at energy of 58 keV, through a sacrificial aluminium stopping layer of thickness 250 nm that was deposited on top of the structure. Helium implanted samples then underwent a sequence of one-hour isochronous thermal treatments in argon carried out every 50°C in the range 500 - 1000°C. The same annealing cycle was also performed on the polysilicon samples before He implantation, for control purposes.

After each annealing step the samples were submitted to the full thermoelectric characterization, which included Seebeck, electrical and thermal conductivity measurements.

The room temperature Seebeck and 2-wire resistance measurements were performed using a home built system described in Section 3.1.1. The samples were obtained by cutting 5×50 mm^2 rectangular chips and evaporating 100-nm thick

aluminium contacts through a shadow mask. The resistances were obtained from the slopes of the I-V characteristics which at the same time were used to control the ohmicity of the contacts. Seebeck voltages were measured by fixing the temperature of the cold contact at 20°C while heating the other contact between 40 and 120°C. For the Hall measurements 17×17 mm^2 square samples were cut and 100-nm thick aluminium contacts were evaporated on small areas in the four corners according to the Van der Pauw geometry. In order to avoid aluminium contamination of the samples during the high temperature annealing the contacts were removed by etching in 10% HCl solution prior to each subsequent annealing step. Thermal conductivity was measured by TDTR technique (see Section 3.1.4.3). For this purpose, a 70-nm thick aluminium layers were deposited on the sample surfaces.

We also performed electron microscopy (EM) analyses. Both low-energy (30 keV) Dark Field Scanning Transmission EM DF-STEM) and in high-energy (200 keV) transmission (TEM) modes were used. Low energy analyses have been performed with a FEI Strata 235M equipped with Bright Field (BF)/Dark Field (DF) solid state detector. TEM and Electron Spectroscopic Images (ESI) have been performed with a JEM2011 electron microscope equipped with conventional LaB_6 electron source and an Electron Energy Loss Imaging Filter (GIF 200®). This attachment allows to record both Electron Energy Loss Spectroscopy (EELS) data and energy filtered Electron Spectroscopic Imaging (ESI).

A typical electron energy loss spectrum consists of three parts [114]

1. Zero-loss peak at 0 eV:

   It mainly contains electrons that still have the original beam energy E_0, i.e., they have only interacted elastically or not interacted at all with the specimen. In thin specimen, the intensity of the zero-loss beam is high, so that damage of the CCD chip can occur. Since there is no useful information in it, the zero-loss beam is often omitted during spectrum collection.

2. Low-loss region (< 100 eV):

   Here, the electrons that have induced plasmon oscillations occur. Since the plasmon generation is the most frequent inelastic interaction of electron

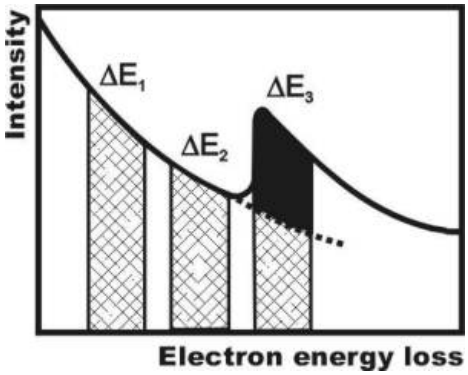

Figure 4.4: Schematic illustration of the three window method used for electron spectroscopic imaging (ESI). Source: [23]

with the sample, the intensity of this region is relatively high. Intensity and number of plasmon peaks increases with specimen thickness.

3. High-loss region (> 100 eV):

   For the ionization of atoms, a specific minimum energy, the critical ionization energy, E_C or ionization threshold, must be transferred from the incident electron to the expelled inner-shell electron, which leads to ionization edges in the spectrum at energy losses that are characteristic for an element. Thus, EELS is complementary to X-ray spectroscopy, and it can be utilized for qualitative element analyses. In particular, the detection of light elements is a main task of EELS.

Compared to the plasmon generation, the inner-shell ionization is a much less probable process, leading to a low intensity of the peaks. This signal can be enhanced by means of ESI technique. Mostly, the so-called three-window method is applied for mapping (see Fig. 4.4): an image is taken after a suitable ionization edge of the corresponding element (post-edge image, ΔE_3), two additional images (pre-edge 1, ΔE_1, and pre-edge 2, ΔE_2) are recorded at energy losses smaller than the ionization edge. Only the electrons passing through the selected energy slit contribute to these images. Specimen drift during recording of these images is compensated by a cross-correlation algorithm implemented in the software. The pre-edge images are used for an appropriate determination of the unspecific

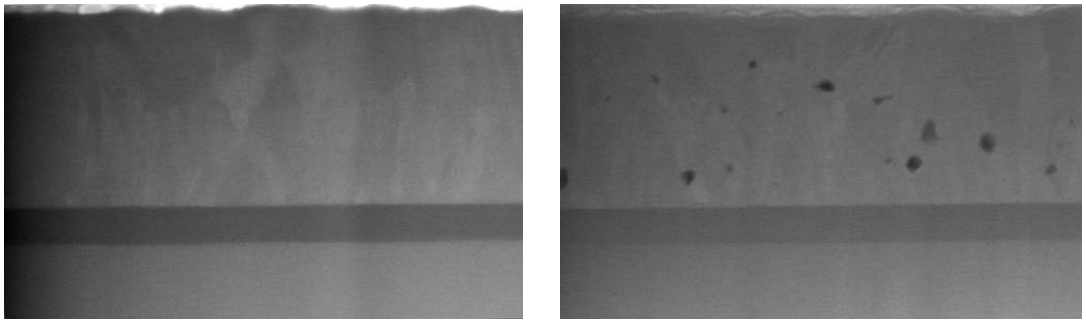

Figure 4.5: STEM images of the cross section of polysilicon structure before He implantation (left) and the structure with NCs annealed at 1000°C (right)

background which is then subtracted from the post-edge image leading to an elemental map with enhanced contrast. Alternatively, the post-edge image can be divided pixel by pixel by a pre-edge image (ratio method) [23]

4.3 Overview of the experimental results

4.3.1 Thermoelectric properties of polycrystalline silicon films with embedded nanocavities

In Fig. 4.5 are presented the STEM images of polysilicon structure before He implantation and after annealing at 1000°C. The micrographs provide clear evidence of the presence of NCs randomly distributed throughout the polysilicon layer after annealing. However, it must be notices that the volume fraction of the NCs formed in polycrystalline silicon is much lower than that in monocrystal.

Fig. 4.6 presents the room temperature Seebeck and electrical conductivity values of polysilicon films after He implantation as a function of annealing temperature T_a. The dashed baselines represent S and σ values measured on blank polysilicon sample with the same doping level before He implantation and annealing.

Annealing of the sample after He-implantation, further to promoting the formation of NCs, also leads to recovering from the radiation damage. Actually, the electrical conductivity displayed a quite steeply growth with the annealing

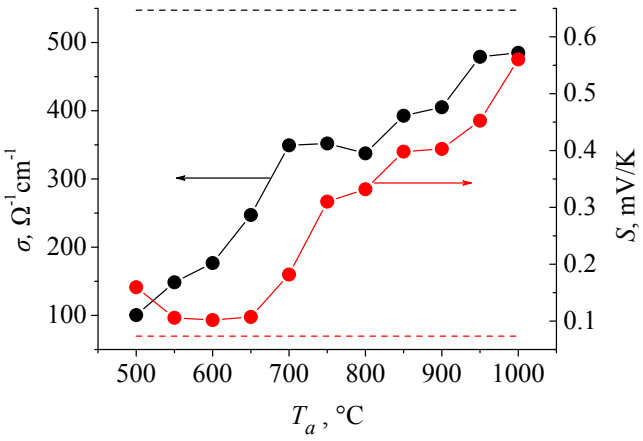

Figure 4.6: Dependence of the room temperature Seebeck coefficient, S, and the electrical conductivity, σ, of degenerate polysilicon films after He implantation on the annealing temperature T_a. The dashed baselines represent the values measured on blank polysilicon sample with the same doping level before He implantation and annealing

temperature, its value being dominated by the increase of hole mobility resulting from disappearance of implantation-induced crystal defects. Thus, it is not unexpected that the measured values of σ along the sequence of annealing steps almost recovered the value of blank polysilicon films with the same doping level. The concurrent growth of the Seebeck coefficient with the annealing temperature was instead less obvious, since one would normally expect the Seebeck coefficient to decrease with conductivity. However, similar trend was also observed in blank polysilicon films upon annealing at temperatures above $T_a = 800$°C , which became the topic of a more detailed investigation presented in the following Section. Owing to simultaneous increase of the two coefficient, the film power factor $S^2\sigma$ rapidly increased upon annealing, getting to the unusually high value of 15.2 mW m^{-1} K^{-2} for $T_a = 1000$°C.

The thermal conductivity κ upon annealing at 1000°C was found to be 25 W m^{-1} K^{-1}, almost two times lower than that measured in bulk polysilicon at comparable doping levels (40 W m^{-1} K^{-1} for boron concentration of 5×10^{20} cm^{-3} [115]). Thus, we could obtain a corresponding ZT of 0.18 at 300 K.

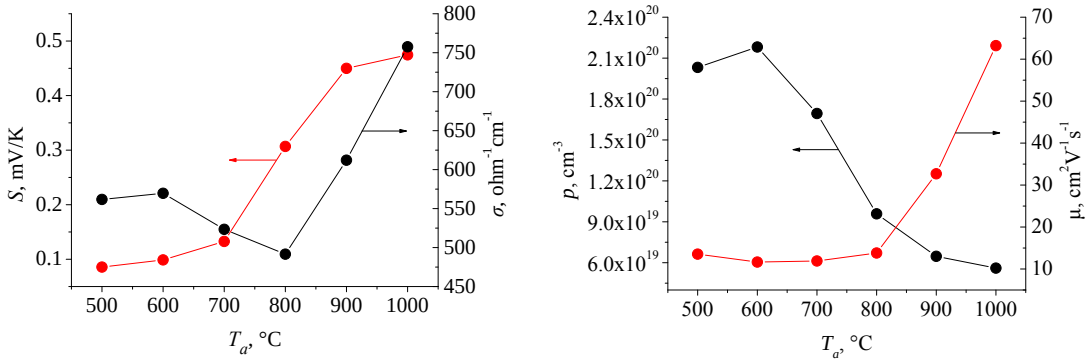

Figure 4.7: Dependence of the room temperature Seebeck coefficient, S, and the electrical conductivity, σ, (left); charge carrier density, p, and the drift mobility, μ, (right) of degenerate polysilicon films on the annealing temperature T_a

4.3.2 Thermoelectric properties of heavily-doped polycrystalline silicon films

As anticipated, also in the case of blank polysilicon films the Seebeck coefficient displayed the unusual trend (Fig. 4.7(left)). The expected decrease of S with σ was observed only up to $T_a = 800°C$, the trend then reverted to a simultaneous increase of both coefficients.

The partial yet striking inconsistency of the experimental data motivated us for a more detailed analysis of the transport coefficients.

Actually the Hall measurements showed that the carrier density was decreasing with T_a while hole drift mobility (computed from the Hall mobility μ_H assuming $\mu/\mu_H = 0.8$ [116]) increased (Fig. 4.7(right))

Therefore, qualitatively, all expected trends are recovered: Seebeck coefficient actually decreases with p, while hole mobility appears to be dominant by ionized impurity scattering. However, a quantitative inspection of the dependence of S upon p shows that as the carrier concentration continues decreasing with annealing temperatures the Seebeck coefficient values start to exceed those normally found at the given carrier concentrations [19] (see Fig. 4.8). Boron solubility also shows some anomalies. Assuming $p = [B_{Si}]$, Hall measurements report a B_{Si} density after heat treatment at 1000°C of 5.6×10^{19} cm^{-3}, smaller than solubil-

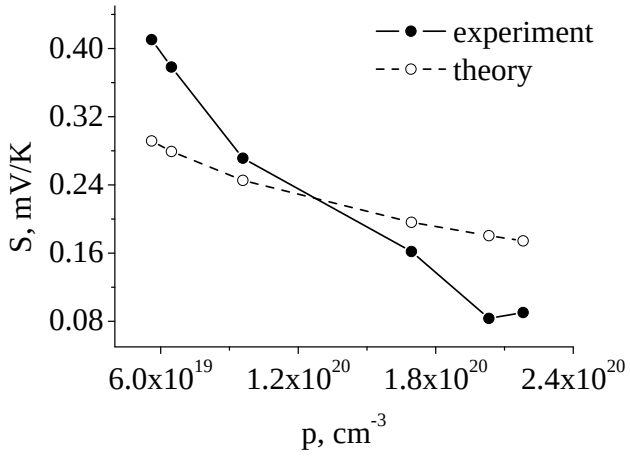

Figure 4.8: Seebeck coefficient, S, as a function of carrier concentration, p. Comparison of experimental data with the theoretical predictions [19]

ity threshold of single crystals, while the solubility of substitutional impurities in polycrystalline semiconductors may often exceed the corresponding value for single crystals because of the combined effect of the destabilization of segregates [117] and of lattice strain [118].

The thermal conductivity was very close to the value measured on the sample with NCs, and it was found to be independent of annealing temperature.

The theoretical analysis if the observed trends is presented in following Sections.

4.4 Analysis of electrical transport properties

Microstructure of the poly layer

We assume that the thermal history of the samples sets the actual values of carrier density. Upon implantation and following post-implantation rapid thermal annealing (RTA), boron being in excess to its solubility limit at the RTA temperature precipitates. In the absence of significant inner surface (grain boundary) oxidation, it is difficult to justify a decrease of solubility in poly-Si. It is therefore sensible to ascribe such difference to the presence of some sort of compensation. At this stage there was no information available about the nature of the compen-

sation, therefore it was natural to ascribe it to the presence of donor impurities. The donor density c_D can be computed as the difference between the B_{Si} single-crystal solid solubility at 1000°C and the actual carrier density upon the final annealing treatment, leading to $c_D = 6.3 \times 10^{19}$ cm^{-3}.

As boron concentration exceeds the solid solubility at any annealing temperature, thermal processing promotes its precipitation. Modelling of the sequential annealing cycles can be carried out within the frame of the Ham's theory of diffusion limited precipitation [119]. Accounting for the growth of precipitates with time in the spherical particle approximation, the average concentration of the dopant at time t, $c(t)$, computes to

$$H\left(\left(\frac{c(0)-c(t)}{c(0)-c_S}\right)^{\frac{1}{3}}\right) = \frac{Dt}{r_S^2}\left(\frac{c(0)-c_S}{c_P-c_S}\right)^{\frac{1}{3}} \tag{4.1}$$

where the Ham function is defined as

$$H = \frac{1}{6}\left(\frac{u^2+u+1}{u^2-2u+1}\right) - \frac{1}{\sqrt{3}}\tan^{-1}\left(\frac{2u+1}{\sqrt{3}}\right) + \frac{1}{\sqrt{3}}\tan^{-1}\left(\frac{1}{\sqrt{3}}\right) \tag{4.2}$$

where c_S is the solubility of the dopant, c_P is the concentration in the precipitate (8×10^{22} for SiB_4 [120]), r_S is the average spacing of precipitates, correlated to their number per volume unit N_P as $r_S = \left((4/3)\pi N_P\right)^{-\frac{1}{3}}$, and D is the dopant diffusivity. Using the standard theory of nucleation, N_P can be correlated with c as

$$N_P = K_P \exp\left(-\frac{16\pi}{3}\left(\frac{\gamma}{k_B T}\right)^3 \frac{1}{c_P^2\left(\ln(c/c_S)\right)^2}\right) \tag{4.3}$$

where K_P is proportional to the number of nucleation cites and γ is the precipitate surface energy. For Si:B Solmi *et al.* [120] proposed values for K_P and γ of 10^{16} cm^{-3} and 2×10^{-5} J cm^{-3}, respectively. One estimates $N_P(T)$ to range in turn between 4.78×10^{15} cm^{-3} (at 500°C) and 1.18×10^{13} cm^{-3} (at 1000°C). In sequential processing we used in our work it is therefore sensible to disregard any nucleation event further to that induced by the first annealing at 500°C, upon which nuclei distribute in solid solution with an average distance r_S of 37 nm.

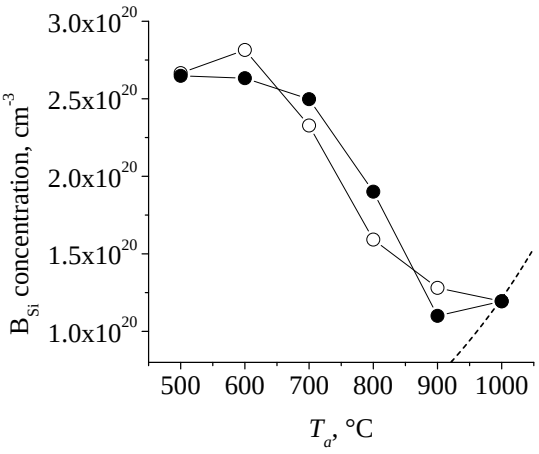

Figure 4.9: Experimental (open circles) and fitted (filled circles) B_{Si} concentration upon annealing. The dashed line shows the solubility of B_{Si} in the single crystal [24]

Their critical radius computes to

$$r_{cr} = \frac{2\gamma}{c_P(k_BT)\ln(c/c_S)} \tag{4.4}$$

i.e. $r_{cr} \approx 0.9$ nm for $c_P \approx 10^{20}$ cm^{-3}. Solving Eq. 4.1 for $c(t)$ and in view of the fact that each annealing step lasted the same time t_a, the average concentration c_j of dissolved (non precipitated) boron at the j-th processing step can be written as

$$\left(\frac{c_j - c_{j-1}}{c_S - c_{j-1}}\right)^{\frac{1}{3}} = H^{-1}\left(\frac{D_j t_a}{r_S^2}\left(\frac{c_{j-1} - c_S}{c_P - c_S}\right)^{\frac{1}{3}}\right) \tag{4.5}$$

where D_j is short for $D(T_j)$. Eq. 4.5 was fitted to the experimental data under the assumption $p = c - c_D$ (Fig. 4.9). Boron diffusivity is found to be

$$D_B = \left(4.8 \times 10^{10}\text{cm}^2\text{s}^{-1}\right)\exp\left(-\frac{1.11eV}{k_BT}\right) \tag{4.6}$$

The relatively low value of the activation energy may find a rationale in the presence of preferential diffusion paths for boron at grain boundaries.

The direct observation of boron in silicon by EELS is still a challenge. The

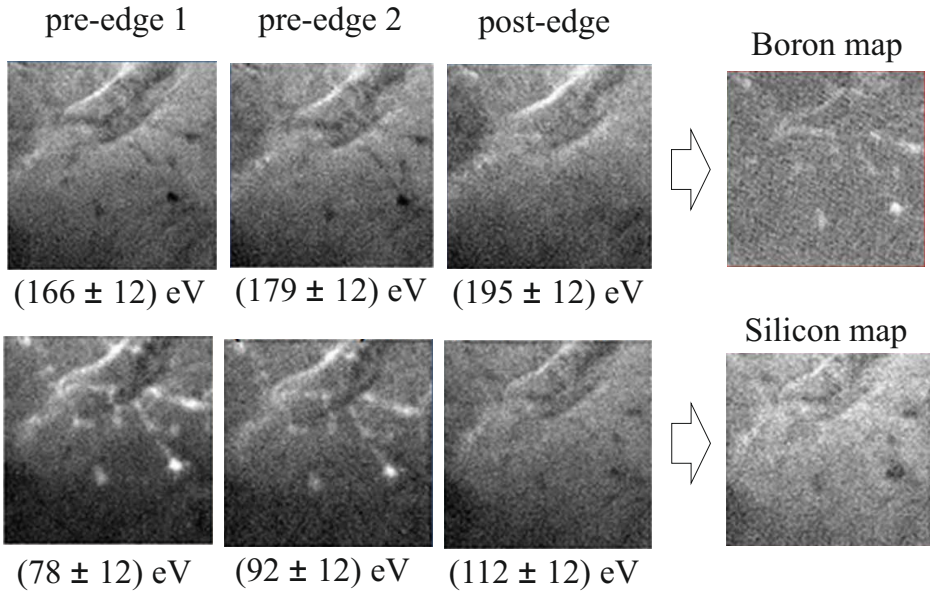

Figure 4.10: ESI procedure to obtain an contrast-enhanced boron and silicon map images of polysilicon layer after annealing at 1000°C

EELS spectrum of Si L_{23} and Si L_1 edges have an intense tail, which extends until 300 eV of energy loss spectrum. This tale act as a heavy background for the 188 eV Boron K edge, and strongly reduces the peak/background ratio until, as in our case, to bury it.

We tried to get information about the presence of boron related precipitates in the poly-silicon layers by exploting Electron Spectroscopic Imaging (ESI), recorded with the three-window method (see Section 4.2), for both Si-L edges and B-K edges on the same area of the specimen. The three-window method is very effective in the background subtraction in the case of small precipitates since this procedure is performed "pixel by pixel" from the signal image by subtracting of two pre-edge background images. The comparison between boron map and silicon map should localize areas of the sample with low silicon signal and high boron signal; thus giving an indication, although not an evidence, of the boron precipitation phenomena.

In Fig. 4.10 presented the procedure to obtain ES images for both 100 eV (Si-

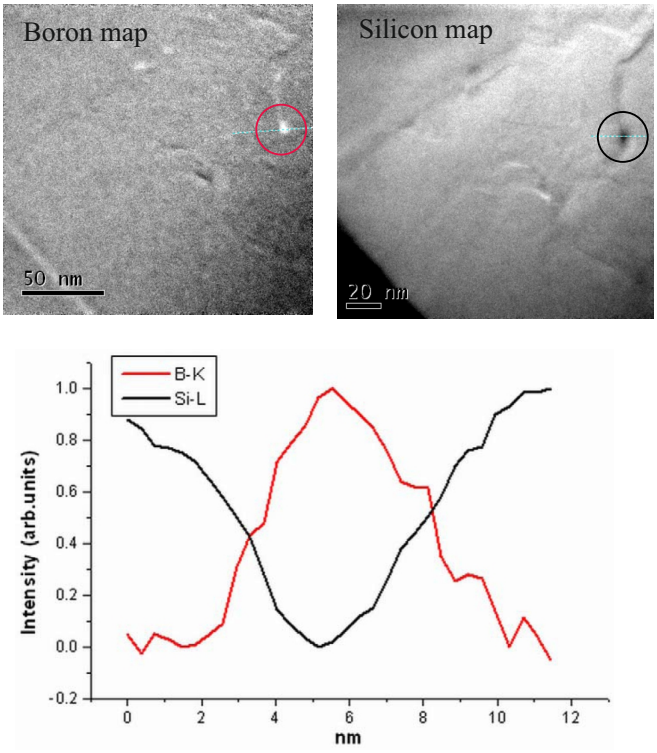

Figure 4.11: ESI profiles taken across the two brighter and darker details of the boron and silicon map images of polysilicon layer after annealing at 1000°C

L) and 188 eV (B-K) energy loss, with an energy window of 12 eV. The contrast inversion clearly visible in the map images strongly support the interpretation of small circular contrast details as boron related precipitates.

A stronger indication is obtained from the comparison between the line profile taken across the two brighter and darker details on the boron and silicon map images, respectively (Fig. 4.11)

Electron energy filtering

It has been shown in Section 2.5.1.2 that when the potential barriers are introduced to the conduction band (for n-type materials) or the valence band (for p-type materials), the higher-energy hot carriers can be selectively transmitted through the structure by filtering out the lower-energy carriers. Since the mean energy per carrier is increased, Seebeck coefficient increases while electrical con-

ductivity is not degraded significantly.

For polycrystalline materials the grains appear as traps for low energy carriers, while higher energy carriers diffuse through the specimen [121]. The grain boundaries therefore appear to filter out the lower energy carriers.

Popescu *et al.* [122] considered the potential barriers with an average height E_b, width ω, and distance between them L. The authors has shown that as E_b increases, the conductivity decreases while the opposite trend is found for the Seebeck coefficient. It can be explained by noting that higher barriers will scatter carriers with larger energy, therefore less carriers will contribute to the electrical current. The same filtering process will contribute to the increase in the energy per carrier leading to an increased Seebeck coefficient for barriers with larger height. The same physical behavior can be achieved by changing ω or L. For example, increasing ω results in a decrease in σ and increase in S due to small quantum-mechanical transmission probability of the carriers through the barrier. Furthermore, decreasing L results in decreasing σ and increasing S due to more frequent carrier scattering from the barriers [122].

EELS analysis reported in the previous Section indicated presence of boron precipitates localized at the grain boundaries (see Fig. 4.11). The size of the precipitates was increasing upon each subsequent annealing cycle, thus increasing the width of the potential barriers. This phenomenon therefore can explain the increasing Seebeck coefficients as well as the low carrier concentrations, also providing a sounder explanantion than donors to the compensation effects we claimed during the analysis of precipitation.

4.5 Analysis of thermal transport properties

In the beginning of this Chapter we mentioned the calculations of Lee *et al.* [16] for ordered nanoporous silicon which predicted the thermal conductivity reduction up to two orders of magnitude compared to the bulk monocrystalline silicon value. The authors actually observed two effects:

1) if we define the pore volume fraction φ as

$$\varphi = \frac{\pi d_p^2}{4(d_p + d_s)^2} \tag{4.7}$$

thermal conductivity decreases as φ increases, as it implies a reduction of the channels for phonon transport;

2) the thermal conductivity becomes smaller even for small pores at given φ due to a decrease of the phonon mean-free path arising from increased phonon scattering at the pore surfaces, which is evaluated by the pore surface-to-volume ratio ρ, namely

$$\rho = \frac{\pi d_p}{(d_p + d_s)^2} \tag{4.8}$$

where d_p is the pore diameter and d_s is the spacing between the pores.

In our case, the average nanocavity diameter and spacing were estimated from the STEM image and found to be 29 nm and > 152 nm, respectively. Thus, the pore volume fraction and the pore surface-to-volume ratio account to are $\varphi = 0.02$ and $\rho < 0.003$ nm^{-1}, which are much lower than those usually reported - and that were also considered in the model calculation [16] (0.07 - 0.38 for φ and 0.30 - 1.18 nm^{-1} for ρ).

As an alternative, one might consider that in polycrystalline silicon films other effects have occurred which have hindered the the effect of the NCs on the thermal properties of the system. The measured thermal conductivity value was almost two times lower than that measured in bulk polycrystalline at similar doping level [115]. This effect however can not be correlated with enhanced phonon boundary scattering, since the film thickness (450 nm) is above the effective phonon mean free path for monocrystalline silicon (near 300 nm [123]). Therefore, the decrease of the thermal conductivity must be connected to the specific microstructure of the films itself. Indeed, the average grain size varied between 20 and 280 nm with smaller grains found at the film interface with SiO_2 and large ones close to the film surface. Such variation in the grain sizes is typical for a columnar structure found in polycrystalline films in which the grain size increases from the bottom of the layer to the top [124].

4.6 Summary

We have studied the thermoelectric properties of heavily doped polycrystalline silicon films. We have analyzed the effect of the formation of NCs, which were expected to act as efficient phonon scattering centres. We have actually shown how NCs do not deteriorate the electronic transport properties of the film. Once the film recovers the implantation damage, both S and σ are fully comparable to the corresponding values measured in non-He implanted films.

Upon thermal treatments at temperatures above 800°C we measured higher Seebeck coefficients than those normally found in monocrystalline silicon at corresponding doping level, while the charge carrier concentration was below the solubility threshold of the single crystal. These phenomena were found to be connected to the formation of the potential barriers at the grain boundaries which accumulated dopant precipitates during the thermal treatments. The potential barriers filtered out the lower energy carriers. As the result less carriers contributed to the electrical current while the mean energy per carrier increased leading to an increase of the Seebeck coefficient.

The thermal conductivity measurements showed a decrease of κ by a factor of 2 with respect to the thermal conductivity reported in the literature in bulk polysilicon. Unexpectedly enough, the same low κ values were found both in the presence and in the absence of NCs. This might suggest that the film microstructure dominates the thermal conductivity in all cases. Grain boundaries are exceedingly effective in damping phonon diffusion, to the point that reportedly effective phonon scatterers as NCs have no impact on κ.

Nevertheless, owing to outstanding electrical properties and rather low (especially compared to single crystal Si) thermal conductivities the resulting figures of merit ZT were found to be equal to 0.18 and 0.13 for polysilicon films with and without nanocavities, respectively, being an order of magnitude higher than those reported for single crystal silicon.

4. THERMOELECTRIC PROPERTIES OF POLYCRYSTALLINE SILICON FILMS WITH AND WITHOUT NANOCAVITIES

Chapter 5

Thermoelectric properties of InGaAs with rare-earth TbAs embedded nanoparticles

This part of the work was performed at the University of California, Santa Cruz during my internship in the Quantum Electronics group under supervision of Prof. Ali Shakouri. The work was performed in collaboration with the group of Prof. John Bowers in the University of California, Santa Barbara and the group of Prof. Joshua Zide in the University of Delaware.

5.1 Introduction

In Chapter 2 it was shown that nearly all recent thermoelectric research has centred on utilizing nanoscale structures within semiconductors to lower thermal conductivity below the alloy limit with hopes of simultaneously increasing the thermoelectric power factor (or at least minimally sacrificing its value) [125]. One such set of materials involves co-doping epitaxial III-V semiconductors like InGa(Al)As with the rare earth metal Er, which, at levels exceeding the solubility limit in the semiconductors, precipitates into randomly-distributed Er-V nanoparticles. The nanoparticles serve to reduce thermal conductivity (through phonon scattering)[126], increase Seebeck coefficient (through electron

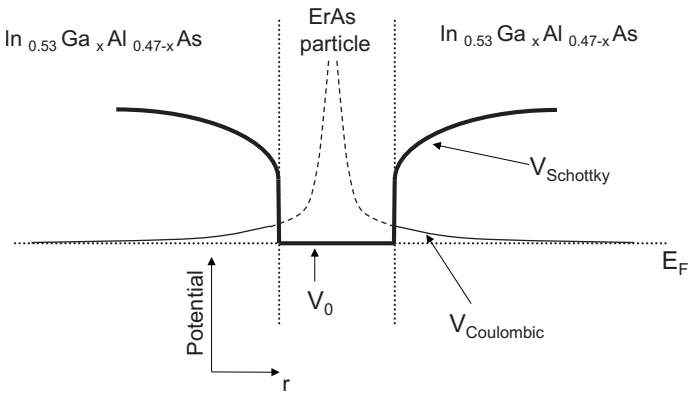

Figure 5.1: Schematic diagram of the potential around an ErAs nanoparticles in InGaAlAs. Source: [25]

filtering or energy-dependent electron scattering) and increase electrical conductivity (through nanoparticle donations of electrons) [25, 45]. Progress in the development of this material system, which targets not only heat transport but also seeks to optimize electronic properties, has thus far led to an n-type ZT of 1.33 at 800 K for 0.6 at. % ErAs in InGaAlAs [25].

The presence of ErAs nanoparticles pins the effective Fermi level of the composite at a particular energy. In InGaAs, the Fermi level is pinned within the conduction band, resulting in high conductive material. In this case, impurity scattering is minimized because the Fermi level is pinned by the nanoparticles, resulting in only a small change in potential, which is undesirable for electron filtering concept. By controlling the aluminium content in InGaAlAs, the position of the conduction band edge (E_C) can be independently tuned with respect to Fermi level (E_F). The energy difference ($E_C - E_F$) determines the scattering mechanisms which electron experience as a result of the nanoparticles. In this case, a scattering term is introduced because a Schottky barrier forms around the nanoparticles, the height of which is linearly related to aluminium content (Fig. 5.1). This Schottky barrier is the dominant scattering mechanism. It is worth noting that in some cases, charge transfer is likely primarily from the nanoparticles to the matrix. Even in a codoped sample, in which charge transfer is reversed, the effective barrier height that carriers experience would be unchanged despite the change in the direction of band-bending [25].

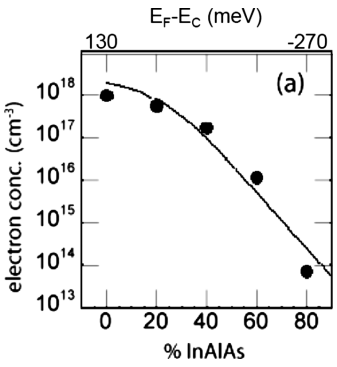

Figure 5.2: Room temperature free electron concentration vs. InGaAl content for ErAs:$(In_{0.52}Al_{0.48}As)_x(In_{0.53}Ga_{0.47}As)_{1-x}$ nanocomposites [25]

In Fig. 5.2 the effective electron concentration of ErAs:$(InAlAs)_x(InGaAs)_{1-x}$ composites, as measured by the Hall effect, is plotted against InAlAs content. It is worth noting that the $(InAlAs)_x(InGaAs)_{1-x}$ matrix material is effectively an InGaAlAs alloy. The curve is the predicted carrier concentration based on a barrier height $(E_C - E_F)$ which changes linearly with InAlAs content. The result is a tunable energy-dependent scatterer [25].

TbAs is expected to provide certain benefits over ErAs, due primarily to its larger lattice constant which is anticipated to favourably alter electronic properties while providing similar reduction in thermal conductivity. It has been observed that strain on the nanoparticles brought by their lattice-mismatch to the matrix may be the major factor in the positioning of the Fermi level within the semiconductor's band gap [127]. Indeed, tensile strain on the nanoparticles causes the Fermi level to be shifted up from a universal donor level while compressive strain causes it to be shifted down. TbAs, which is less strained than ErAs in InGaAs with $\approx 0.9\%$ tensile mismatch, is expected to pin the Fermi level below the conduction band. The Seebeck coefficient should then be improved, since this quantity is proportional to the average energy transported by the charge carrier with respect to the Fermi energy, particularly at high temperature, relative to ErAs-containing materials.

Although deposition of TbAs (<1%) results in a significant increase in power factor, significant reduction in thermal conductivity is not observed [125]. Larger concentrations result in a more significant reduction in thermal conductivity. We

have studied the thermoelectric properties of TbAs:InGaAs nanocomposites for three different (relatively large) Tb concentrations of 1.68, 2.47, and 6.36% and compared the data with Si-doped InGaAs for control purposes.

5.2 Experimental details

TbAs:InGaAs nanocomposites were grown by molecular beam epitaxy (MBE) and characterized by several techniques including high-angle annular dark field scanning electron microscopy (HAADF STEM), Hall effect measurements, time-domain thermoreflectance (TDTR), and high temperature in-plane Seebeck coefficient and electrical conductivity measurements.

5.2.1 Material growth and processing

The samples were grown in an Osemi NexGEN® solid-source MBE system. At a substrate temperature of 490°C (determined by band-edge thermometry), terbium was co-deposited during the growth of $In_{0.53}Ga_{0.47}As$ on top of InP:Fe semi-insulating substrate. The Tb concentration was above its solubility limit in InGaAs which resulted in random precipitation of the nanoparticles throughout the material. The samples containing 1.68 and 2.47% Tb were 1μm thick while the one with 6.36% Tb had thickness of 250 nm. The InGaAs growth rates were 1.188, 1.2744, and 1.28952 $\AA$/s for the sample with 1.68, 2.47%, and 6.36% Tb, respectively and the related Tb source temperatures were respectively 1330, 1360, and 1420°C. Rutherford Backscattering Spectroscopy (RBS) was used for layer composition and thickness measurements.

For the room temperature Hall measurements the samples had Van der Pauw geometry with indium contacts soldered at the corners. For the high temperature measurements the Van der Pauw and Seebeck bar patterns were defined by photolithography using the positive photoresist AZ-4210® (Fig. 5.3(a)). The patterns were then chemically etched in the solution H_3PO_4:H_2O_2:H_2O (1:1:8 by volume) which is selective to InGaAs over InP. The photoresist was removed in acetone/isopropanol/de-ionized water. In order to prevent As desorption from the surface during high temperature measurements, the sample surface was then

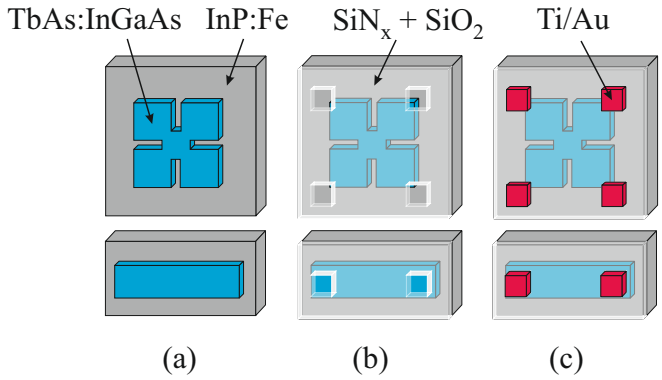

Figure 5.3: Fabrication steps of Van der Pauw (up) and Seebeck bar (down) samples for high temperature measurements: (a) definition of the sample pattern, (b) encapsulation with $SiN_x + SiO_2$ and definition of the electrical contact regions, (c) metallization with Ti/Au and lift off the metal everywhere except the contact areas

encapsulated with 150 nm silicon nitride followed by 300 nm silicon dioxide using Plasma-Enhanced Chemical Vapor Deposition (PECVD) The contact regions were then defined by photolithography using negative photoresist AZ-5214®, and the encapsulation layer was etched using buffered HF (Fig. 5.3(b)). The sample was then metalized by electron beam evaporation-deposition of 400 nm Au with 40 nm Ti as an adhesion layer. This metallization is functional up to 700 K, beyond which Ti diffusion becomes an issue [128]. Metal was lifted off everywhere except the contact areas during the photoresist removal in acetone/isopropanol/deionized water (Fig. 5.3(c)).

5.2.2 Sample characterization

Plan-view HAADF STEM samples were prepared by mechanical polishing without the use of Ar ion milling; then, micrographs were taken with an FEI Titan 80-300 STEM/TEM equipped with a field-emission electron gun which was operated at 300 kV. 0.8% and 14% TbAs:InGaAs samples are shown in Figs. 5.4(a) and 5.4(b), respectively. Randomly-distributed TbAs nanoparticles of about 1nm in diameter were found in 0.8% TbAs:InGaAs while nanoparticles appear to be much larger and less uniform in size in a 14% TbAs:InGaAs sample possibly due

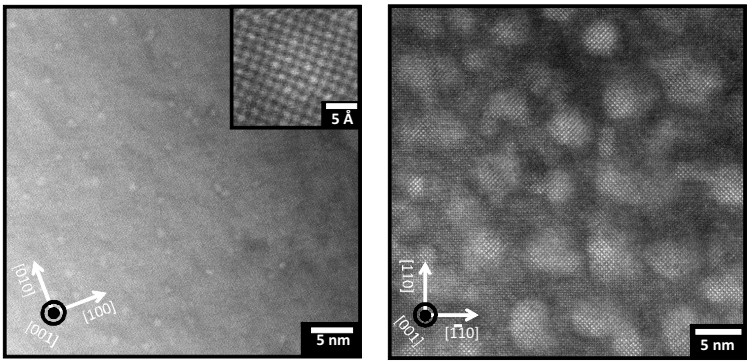

Figure 5.4: HAADF STEM plan-view images of (a) 0.8% TbAs:InGaAs and (b) 14% TbAs:InGaAs

to overlap of multiple particles.

The high temperature Seebeck coefficient and electrical conductivity measurements were performed using a home built system presented in Fig. 5.5(left). The experimental setup consisted of the vacuum chamber, the thermostat: a cylindrical radiant heater of 8.5 cm inner diameter and the wall thickness of 2.5 cm mounted on a hollow stainless steel standoff, the measurement stage represented in Fig. 5.5(right) which is capable of inducing temperature gradients across the sample mounted on the top of the standoff, two R-type thermocouples and two additional platinum wires used for the 4-probe electrical conductivity measurements, two DC power supplies used for heating, Eurotherm® 2404A temperature controller, HP/Agilent® 34420A nanovolt/micro-ohm meters, and Varian® turbo-vacuum pumping system. The detailed description of the setup can be found elsewhere [129]

5.3 Results and discussion

5.3.1 Electrical and thermal properties

The room temperature Hall effect data from as-grown TbAs:InGaAs with indium contacts is summarized in Table 5.1. We also present the data measured in Si-doped InGaAs. As the Tb content increases, the charge carrier concentra-

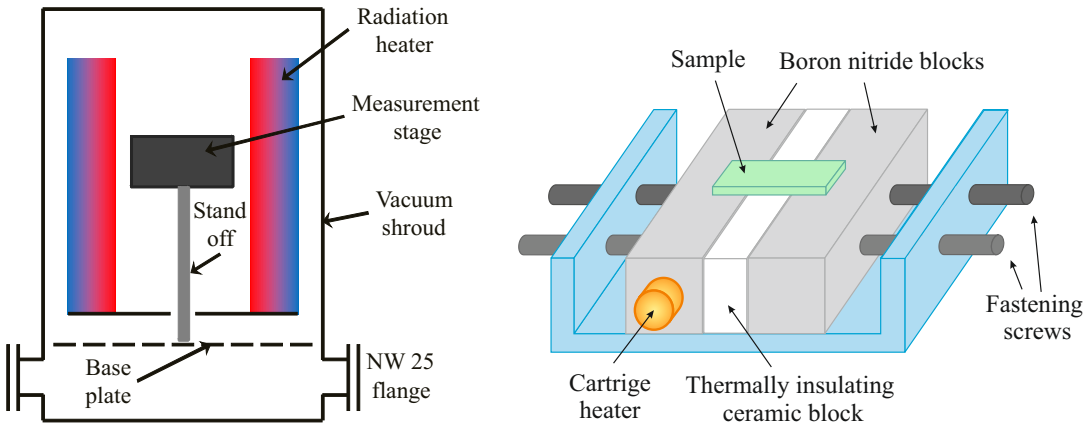

Figure 5.5: Side-view cross-sectional diagram of the vacuum insulated thermostat (left) and schematic diagram of the in-plane Seebeck coefficient measurement stage (right)

% TbAs	Carrier concentration, cm^{-3}	Mobility, $cm^2/V\ s$	Carrier type
1.68%	1.42×10^{18}	1490	n
2.47%	2.49×10^{18}	1300	n
6.36%	8.68×10^{17}	954	n
0% (Si-doped)	2.47×10^{18}	3396	n

Table 5.1: Room temperature Hall effect data of TbAs:InGaAs nanocomposites and Si-doped InGaAs

tion first increases up to a maximum of 2.77×10^{18} cm^{-3} for 3.32% Tb, and then decreases; while the mobility monotonically decreases. The size of the nanoparticles increases with increasing Tb content. It follows that large nanoparticles are less electrically active [130] and contribute fewer electrons to the InGaAs matrix. With increasing nanoparticle content the randomness of the system increases and therefore the mobility decreases.

Indium melts at 165°C, hence it is not a suitable contact material for high temperature measurements. This necessitates Ti/Au deposition by photolithography. However we observed discrepancies in the Hall effect data obtained from the samples before and after processing. The distortion in the Hall carrier concentrations and the Hall mobilities was especially large (over 30%). We believe

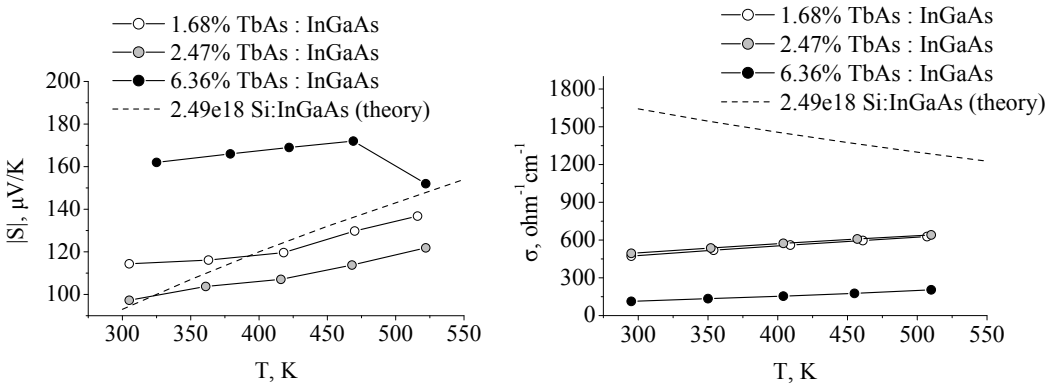

Figure 5.6: High temperature Seebeck coefficient (left) and electrical conductivity (right) of TbAs:InGaAs nanocomposites together with the computed trends for Si-doped InGaAs

that the reason for this distortion is incompatibility of TbAs:InGaAs samples with standard III-V wet chemical processing techniques, which is the topic of a forthcoming paper [131]. However, the electrical conductivity values, except for the sample with 1.68% Tb (which is yet unclear), remained within acceptable limits ($\approx 10\%$). Therefore, we do not present here the high temperature Hall effect data from the processed samples, presenting instead only the electrical conductivity. For further analysis, including comparisons with Si-doped InGaAs, we will be only using the carrier concentrations measured in the samples before the processing.

The Seebeck coefficient and electrical conductivity of TbAs:InGaAs nanocomposites together with the theoretical trends for Si-doped InGaAs are plotted as a function of temperature in Fig 5.6. The theoretical data for Si-doped InGaAs was computed using non-parabolic bands and including optical phonon effects [132].

As we can see, both coefficients increase with temperature. The growth of electrical conductivity is due to increasing carrier concentration via nanoparticle doping at high temperatures. The explanation of the trend of the Seebeck coefficient with temperature is less obvious: in a typical semiconductor one would expect the Seebeck coefficient to decrease with increasing carrier concentration. The simultaneous increase of the Seebeck coefficient and electrical conductivity indicate presence of energy dependent electron scattering or electron filtering. In

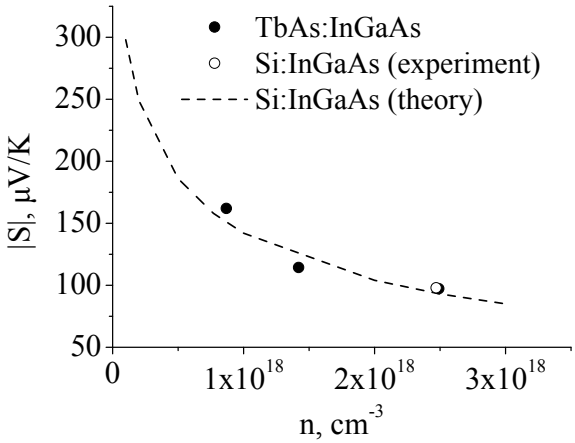

Figure 5.7: "Pisarenko" plot for experimentally measured room temperature Seebeck coefficients of TbAs:InGaAs nanocomposites and Si-doped InGaAs together with computed trend for Si-doped InGaAs

such regime the electrical transport is limited only to those electrons which energy is high enough to overcome the potential barriers formed at the TbAs/InGaAs interfaces. The average energy of the electrons contributing to the conduction becomes higher, hence higher is the thermopower.

The room temperature Seebeck data for TbAs:InGaAs nanocomposites and Si-doped InGaAs together with the theoretical trend for Si-doped InGaAs are plotted as a function of the carrier concentration ("Pisarenko" plot) in Fig. 5.7. The theoretical data for Si-doped InGaAs was again computed using non-parabolic bands and including optical phonon effects [132]. We have not observed increase of Seebeck coefficients of TbAs:InGaAs samples compared to Si-doped InGaAs. It is possible that there is enhancement in the Seebeck coefficient of TbAs:InGaAs at high temperatures, but since standard III-V processing appears to corrupt Hall effect measurements on TbAs:InGaAs, we do not have reliable carrier concentration data and are therefore unable to make fair comparisons at temperatures above 300 K.

We observed over two fold drop of the electrical conductivity compared to the Si-doped InGaAs which is likely to be due to pronounced nanoparticle scattering and scattering due to possible strain induced defects at the TbAs/InGaAs interfaces.

% TbAs	0 (Si-doped)	1.68	2.47	6.36
κ, W/m K	5.9	3.5	2.95	2.25

Table 5.2: Room temperature thermal conductivity of TbAs:InGaAs nanocomposites and Si-doped InGaAs measured by TDTR technique

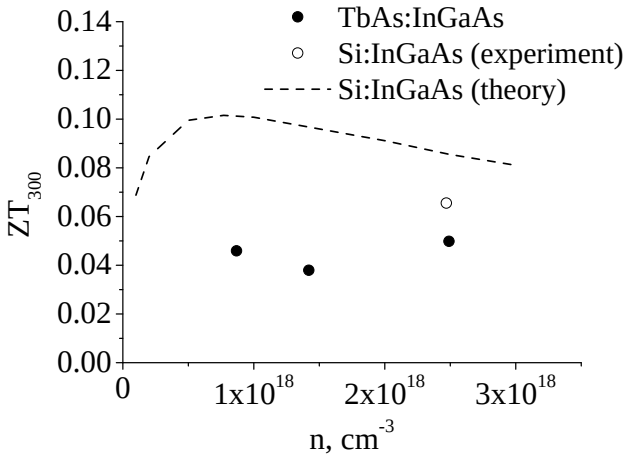

Figure 5.8: Experimental room temperature thermoelectric figure of merit ZT of TbAs:InGaAs nanocomposites and Si-doped InGaAs as a function of the carrier concentration together with computed trend for Si-doped InGaAs

The TDTR results for the thermal conductivity of TbAs:InGaAs nanocomposites and Si-doped InGaAs are presented in Table 5.2.

The thermal conductivity of TbAs:InGaAs nanocomposites was lower than that of Si-doped InGaAs and it decreased with increasing nanoparticle content. In spite of that decrease no improvement in the thermoelectric performance over Si-doped InGaAs was observed (see Fig. 5.8).

5.3.2 Anisotropic effects

Sample with 6.36% Tb content was found to be 33% more resistive in one direction and we have also observed anisotropy of the thermoelectric properties. The results are summarized in Fig. 5.9. We believe that this anisotropy is connected with the diffusion of the nanoparticles during the growth. The nanoparticles tend to diffuse along the fast diffusion direction, most probably along (110). As a result

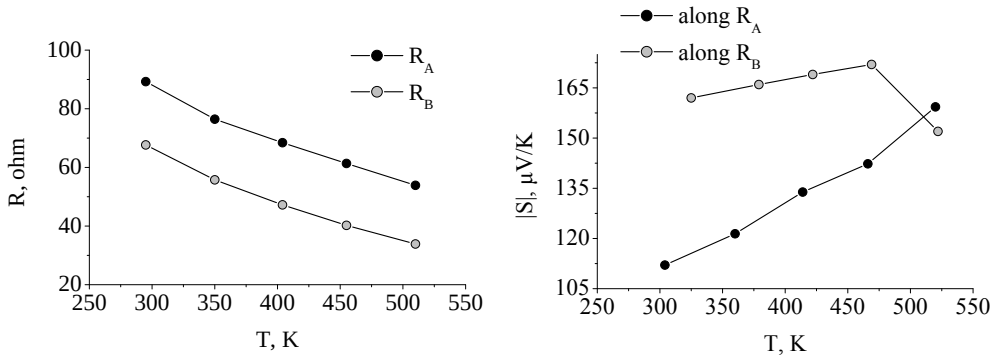

Figure 5.9: Electrical resistance (left) and the Seebeck coefficient (right) measured in perpendicular directions in TbAs:InGaAs nanocomposite with 6.36% of TbAs content

the potential barriers are formed, which would affect the electronic transport across them. The measured Seebeck coefficient across the barriers was lower. However, as the temperature increased, the electron energy became enough to overcome the barriers and the thermopower approached the value measured in the direction along the barriers. It is worth to mention that similar trends were also observed in ErAs:InGaAs nanocomposites with high nanoparticle content.

5.4 Summary

We studied high temperature thermoelectric properties of TbAs:InGaAs nanocomposites with 1.68, 2.47, and 6.36% of TbAs nanoparticles. The occurrence of the energy dependent electron scattering was experimentally observed for all the compositions. However, drastic worsening of the electrical properties compared to Si-doped InGaAs was also observed. In spite of the decrease of the thermal conductivity the thermoelectric performance was still governed by the electrical properties and no enhancement of ZT over Si-doped InGaAs was achieved.

For the nanocomposite with 6.36% of Tb content, anisotropy of the electrical properties was observed which is believed to be a result of the preferential alignment of the nanoparticles along the fast diffusion direction.

5. THERMOELECTRIC PROPERTIES OF INGAAS WITH RARE-EARTH TBAS EMBEDDED NANOPARTICLES

Chapter 6

Conclusions

Technical advances of the twentieth century lead to an unprecedented rise of total energy consumption. This growth was accompanied by increasing reliance on fossil fuels.

The necessity to minimize environmental impact of energy use in general and potential consequences of greenhouse gases generation brings our society to the moment when the fundamental changes have to be made in the key twentieth-century energy trends. The new trends should include improvements in energy conservation and energy conversion efficiency, as well as gradual transitions towards renewable energy techniques.

One of the promising renewable energy techniques is thermoelectric power generation. It was shown that the large amount of generated energy (almost 60%) is rejected, usually in the form of heat. This loss is largest in electrical power generation and transportation.

Thermoelectric waste heat recovery for automobiles is a typical case that is being explored by several major car manufacturers. Several companies have actually already demonstrated the prototypes of thermoelectric modules fitted into the exhaust lines of boosted gasoline engines. Thermoelectric power generation systems can be also used for a wide range of other waste heat resources, such as hot water waste from steel plants, geothermal energy from hot springs, hot surfaces of furnaces, incinerators and other industrial processes, and remote subsea oil wells.

Thermoelectric efficiency of a material is described by the so-called thermo-

electric figure of merit $ZT = S^2\sigma\kappa^{-1}T$, where S is the Seebeck coefficient, σ and κ are correspondingly the electrical and the total thermal conductivities. Nanostructuring has opened new ways to improve thermoelectric performance of a material either by decreasing κ or by increasing the power factor $S^2\sigma$.

In this work we performed an experimental investigation of thermoelectric properties of two promising nanostructured materials analysing the effects of both electrical and thermal transport optimization.

The first material under investigation were heavily-doped polycrystalline silicon films with embedded nanocavities. We have analysed the effect of the formation of nanocavities, which were expected to act as efficient phonon scattering centres, thus reducing the thermal conductivity. We found that the nanocavities did not deteriorate the electronic transport properties of the film.

To our surprise, the material also showed outstanding thermoelectric properties. Upon thermal treatments at temperatures above 800°C we measured higher Seebeck coefficients than those normally found in monocrystalline silicon at corresponding doping level. This increase was found to be connected to the formation of the potential barriers at the grain boundaries which accumulated dopant precipitates during the thermal treatments. In such regime the electrical transport is limited only to those electrons which energy is high enough to overcome the potential barriers. The average energy of the electrons contributing to the conduction becomes higher, hence higher is the thermopower.

The thermal conductivity of polysilicon films with nanocavities was found to be almost two times lower the value reported in the literature for bulk polysilicon. Unexpectedly enough, the same low value was measured also in the sample without nanocavities. This might suggest that the film microstructure dominates the thermal conductivity in all cases. Grain boundaries are exceedingly effective in damping phonon diffusion, to the point that reportedly effective phonon scatterers as nanocavities have no impact on thermal conductivity.

Nevertheless, owing to outstanding electrical properties and rather low (especially compared to single crystal Si) thermal conductivities the resulting figures of merit ZT were found to be equal to 0.18 and 0.13 for polysilicon films with and without nanocavities, respectively, being an order of magnitude higher than those reported for single crystal silicon.

This result is of a great importance especially in a view of large scale industrial applications. As opposed to many other applications when the transition from the single crystal to polysilicon is mostly motivated by the cost efficiency, in the case of thermoelectric materials, polycrystalline silicon films actually found to have superior thermoelectric properties than single crystals.

The second system we have studied were InGaAs nanocomposites with high concentration ($> 1\%$) of rare earth TbAs embedded nanoparticles. In this group of materials, the nanoparticles serve to reduce thermal conductivity (through phonon scattering), increase Seebeck coefficient (through electron energy filtering), and increase of electrical conductivity (through nanoparticle donation of electrons). Progress in the development of this material system has thus far led to an n-type ZT of 1.33 at 800 K for 0.6 at. % ErAs in InGaAlAs.

Although, previous experiments on TbAs:InGaAs nanocomposites with small ($< 1\%$) content of TbAs nanoparticles showed a significant improvement of the power factor, significant reduction of the thermal conductivity was not observed. Larger concentrations of nanoparticles were expected to result in a more significant reduction of the thermal conductivity.

We studied high temperature thermoelectric properties of TbAs:InGaAs nanocomposites with 1.68, 2.47, and 6.36% of TbAs nanoparticles.

The Seebeck coefficients and electrical conductivities showed unusual for a typical semiconductor behavior simultaneously increasing with temperature, which indicated presence of electron energy filtering.

However, we observed over twofold drop of the electrical conductivity compared to the common-doped InGaAs which was likely to be due to pronounced nanoparticle scattering and scattering due to possible strain induced defects at the TbAs/InGaAs interfaces.

The thermal conductivity of TbAs:InGaAs nanocomposites was lower than that of common-doped InGaAs and it decreased with increasing nanoparticle content. In spite of that decrease the thermoelectric performance was still governed by the electrical properties and no enhancement of ZT over Si-doped InGaAs was achieved.

Appendix A

LabView program for room temperature Seebeck measurement

A LabView program was used to control room temperature Seebeck measurements. A snapshot of the front panel of the program is given in Fig. A.1

The three channels of a voltage scanning card (Keithley® data acquisition system Model 7702) were used to simultaneous (within 1 s) reading of the Seebeck voltage (Channel 105) and the temperatures of the hot and cold part (Channels 106:107). The readings were performed every 10 s.

Fig. A.2 shows the programs block diagram. First, the scanning card channels were configured according to the measurement type (voltage or temperature). The data were then acquired from the defined channels forming an array of three data points: the Seebeck voltage and the temperatures of the hot and cold sides. After acquisition, the data were organised by splitting the three components of the array, such that the data points will be then grouped according to their channel. The loop structure was used in order to perform the multiple readings. After the end of the loop cycle the data were saved to a .txt file in a form of a three-column table.

A. LABVIEW PROGRAM FOR ROOM TEMPERATURE SEEBECK MEASUREMENT

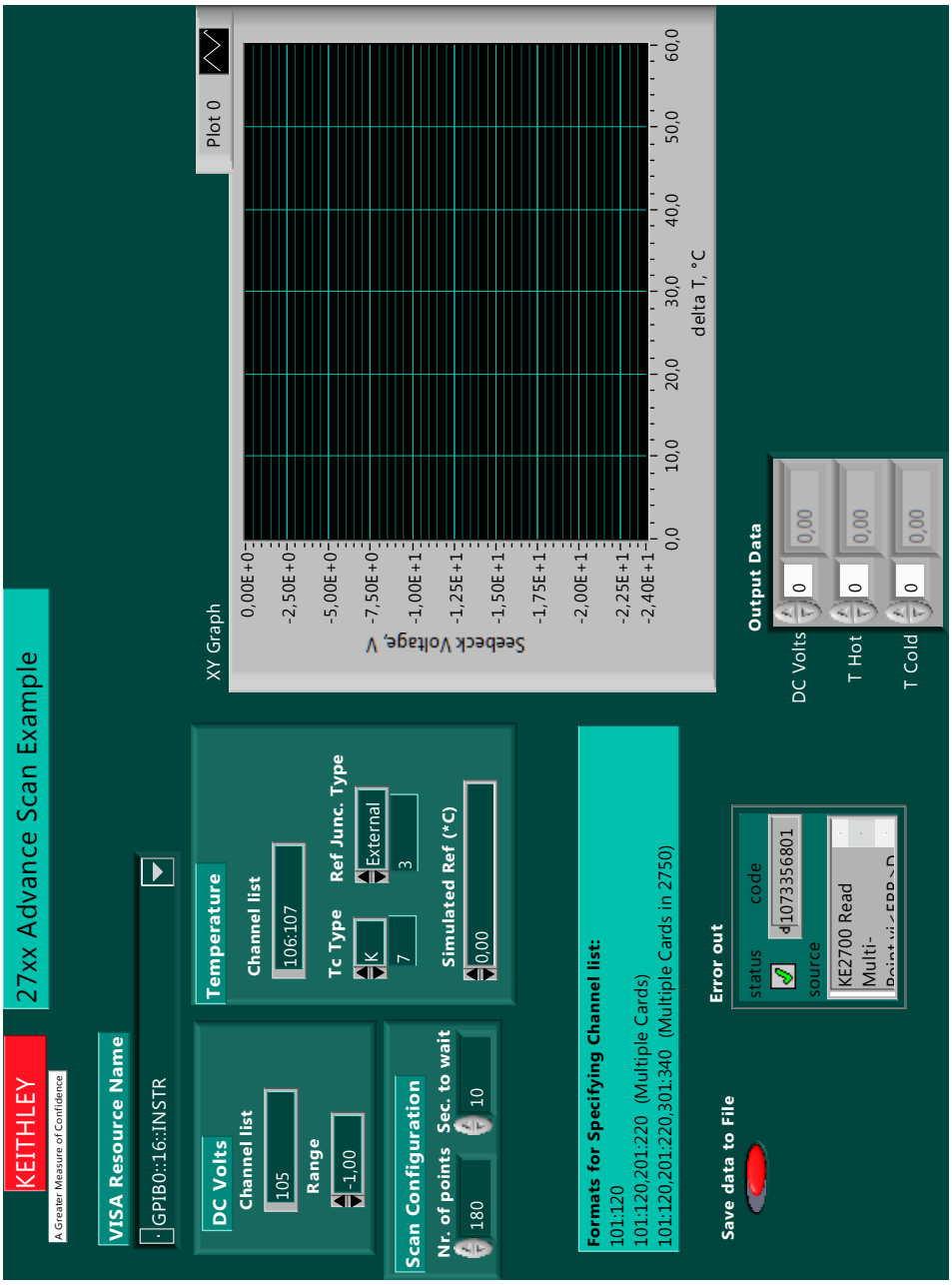

Figure A.1: The front panel of the LabView program for Seebeck measurment

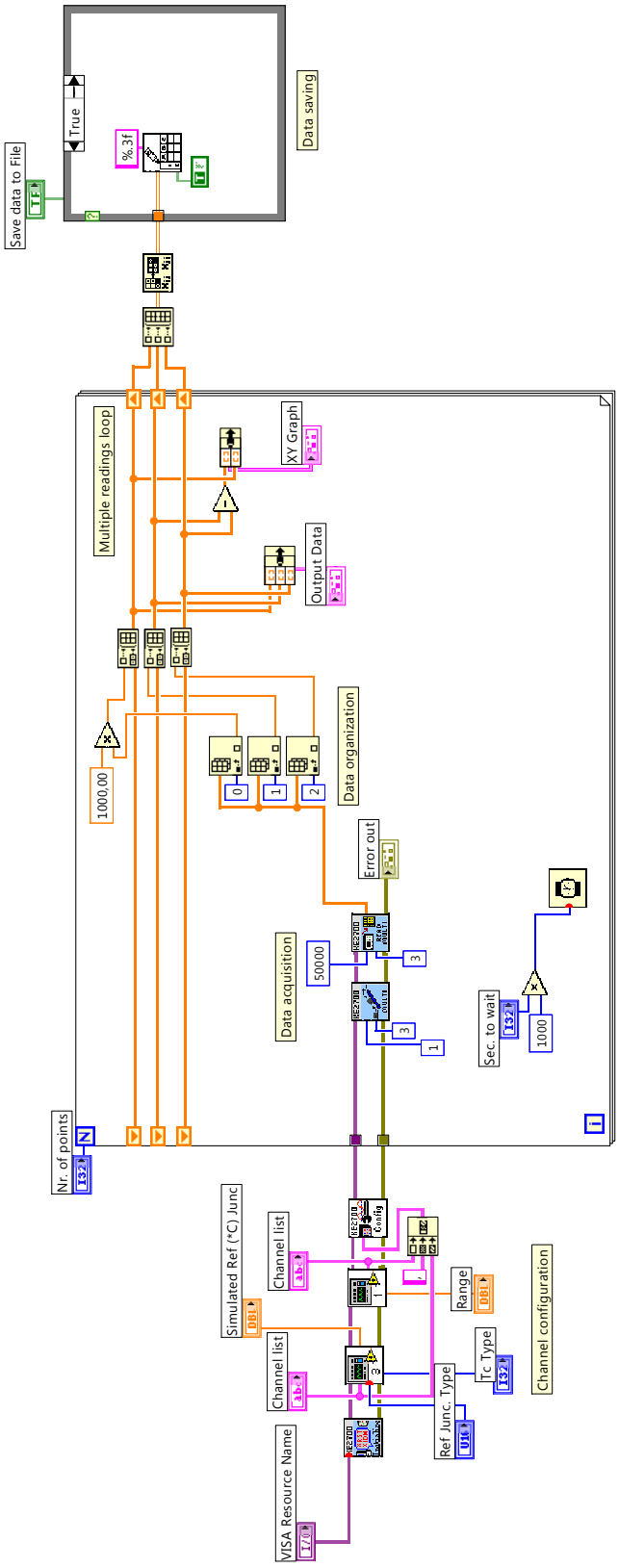

Figure A.2: The block diagram of the LabView program for Seebeck measurment

A. LABVIEW PROGRAM FOR ROOM TEMPERATURE SEEBECK MEASUREMENT

References

[1] Energy Balances of OECD Countries, IEA. URL http://www.iea.org/stats/index.asp. xv, 3

[2] Estimated U. S. Energy Use in 2009. URL https://flowcharts.llnl.gov/energy.html. xv, 5

[3] L. I. Anatychuk. On the discovery of thermoelectricity by Volta. *Journal of Thermoelectricity*, 2:5, 2004. xv, 11, 12

[4] Je-Hyeong Bahk. *Electron transport in ErAs:InGa(Al)As metal/semiconductor nanocomposites for thermoelectric power generation.* PhD thesis, University of California, Santa Barbara, 2010. xv, 22

[5] M. S. Dresselhaus, G. Chen, M. Y. Tang, R. G. Yang, H. Lee, D. Z. Wang, Z. F. Ren, J.-P. Fleurial, and P. Gogna. New Directions for Low-Dimensional Thermoelectric Materials. *Advanced Materials*, 19:1043, 2007. xv, 23

[6] L. D. Hicks, T. C. Harman, X. Sun, and M. S. Dresselhaus. Experimental study of the effect of quantum-well structures on the thermoelectric figure of merit. *Physical Review B*, 53:R10493, 1996. xv, 24

[7] T. C. Harman, P. J. Taylor, D. L. Spears, and M. P. Walsh. Thermoelectric quantum-dot superlattices with high ZT. *Journal of Electronic Materials*, 29:L1, 2000. xv, 24, 25

[8] C. Vineis, T. Harman, S. Calawa, M. Walsh, R. Reeder, R. Singh, and A. Shakouri. Carrier concentration and temperature dependence of the

electronic transport properties of epitaxial PbTe and PbTe/PbSe nanodot superlattices. *Physical Review B*, 77:235202, 2008. xv, 23, 24, 25

[9] Ali Shakouri and Mona Zebarjadi. *Thermal Nanosystems and Nanomaterials*. Springer Berlin Heidelberg, 2009. xvi, 17, 19, 24, 26

[10] Daryoosh Vashaee and Ali Shakouri. Improved Thermoelectric Power Factor in Metal-Based Superlattices. *Physical Review Letters*, 92:106103, 2004. xvi, 25, 27

[11] Mona Zebarjadi, Keivan Esfarjani, Ali Shakouri, Zhixi Bian, Je-Hyeong Bahk, Gehong Zeng, John Bowers, Hong Lu, Joshua Zide, and Art Gossard. Effect of Nanoparticles on Electron and Thermoelectric Transport. *Journal of Electronic Materials*, 38:954, 2009. xvi, 26, 27, 28, 29

[12] David Cahill, Fumiya Watanabe, Angus Rockett, and Cronin Vining. Thermal conductivity of epitaxial layers of dilute SiGe alloys. *Physical Review B*, 71:235202, 2005. xvi, 29, 30

[13] Kuei Fang Hsu, Sim Loo, Fu Guo, Wei Chen, Jeffrey S. Dyck, Ctirad Uher, Tim Hogan, E. K. Polychroniadis, and Mercouri G. Kanatzidis. Cubic $AgPb_{(m)}SbTe_{(2+m)}$: bulk thermoelectric materials with high figure of merit. *Science*, 303:818, 2004. xvi, 30, 31

[14] Allon I. Hochbaum, Renkun Chen, Raul Diaz Delgado, Wenjie Liang, Erik C. Garnett, Mark Najarian, Arun Majumdar, and Peidong Yang. Enhanced thermoelectric performance of rough silicon nanowires. *Nature*, 451: 163, 2008. xvi, 31, 32

[15] Pierre Martin, Zlatan Aksamija, Eric Pop, and Umberto Ravaioli. Impact of Phonon-Surface Roughness Scattering on Thermal Conductivity of Thin Si Nanowires. *Physical Review Letters*, 102:125503, 2009. xvi, 31, 32

[16] J.-H. Lee, J. C. Grossman, J. Reed, and G. Galli. Lattice thermal conductivity of nanoporous Si: Molecular dynamics study. *Applied Physics Letters*, 91:223110, 2007. xvi, 32, 33, 63, 77, 78

[17] Jing-Feng Li, Wei-Shu Liu, Li-Dong Zhao, and Min Zhou. High-performance nanostructured thermoelectric materials. *NPG Asia Materials*, 2:152, 2010. xvi, 35, 37

[18] S. R. Brown, S. M. Kauzlarich, Franck Gascoin, and J. G. Snyder. $Yb_{14}MnSb_{11}$: New high efficiency thermoelectric material for power generation. *Chemistry of Materials*, 18:1873, 2006. xvi, 36, 37

[19] A. W. Van Herwaarden. Thermal sensors based on the Seebeck effect. *Sensors and Actuators*, 10:321, 1986. xvii, xviii, 42, 43, 71, 72

[20] L. J. van der Pauw. A method of measuring specific resistivity and Hall effect of discs of arbitrary shape. *Philips Res. Repts*, 13:1, 1958. xvii, 39, 46, 47, 48, 51

[21] V. Raineri, M. Saggio, and E. Rimini. Voids in silicon by He implantation: From basic to applications. *Journal of Materials Research*, 15:1449, 2000. xvii, 64, 65

[22] E. Romano, D. Narducci, F. Corni, S. Frabboni, G. Ottaviani, R. Tonini, and G. F. Cerofolini. Nanocavities in silicon: An infrared investigation of internal surface reconstruction after hydrogen implantation. *Materials Science and Engineering B*, 159-160:173, 2008. xvii, 64, 65

[23] Electron Spectroscopic Imaging. URL `http://www.microscopy.ethz.ch/ESI.htm`. xviii, 68, 69

[24] G. L. Vick and K. M. Whittle. Solid Solubility and Diffusion Coefficients of Boron in Silicon. *Journal of The Electrochemical Society*, 116:1142, 1969. xviii, 74

[25] J. M. O. Zide, J.-H. Bahk, R. Singh, M. Zebarjadi, G. Zeng, H. Lu, J. P. Feser, D. Xu, S. L. Singer, Z. X. Bian, A. Majumdar, J. E. Bowers, A. Shakouri, and A. C. Gossard. High efficiency semimetal/semiconductor nanocomposite thermoelectric materials. *Journal of Applied Physics*, 108: 123702, 2010. xviii, 82, 83

[26] Vaclav Smil. *Energy at the crossroads : global perspectives and uncertaities*. MIT Press, Cambridge, Massachusetts, 2003. 2

[27] Henrik Lund. *Renewable Energy Systems*. Elsevier, 2010. 4

[28] D. M. Rowe. Thermoelectric waste heat recovery as a renewable energy source. *International Journal of Innovations in Energy Systems and Power*, 1:13, 2006. 6, 9

[29] G. Bennet. *CRC Handbook of Thermoelectrics*. 6

[30] Gao Min. *Energy Harvesting for Autonomous Systems*. Artech House, 2010. 8

[31] Thermoelectric car prototypes in 2009 and in production 2012. URL http://nextbigfuture.com/2008/08/thermoelectric-car-prototypes-in-2009.html. 8

[32] BMW Future Technology Talk. URL http://www.roadandtrack.com/auto-news/tech/bmw-future-technology-talk. 8

[33] Takenobu Kajikawa. Approach to the Practical Use of Thermoelectric Power Generation. *Journal of Electronic Materials*, 38:1083, 2009. 9

[34] David Keith Chalmers MacDonald. *Thermoelectricity: an introduction to the principals*. Dover Publications, INC., 2006. 11

[35] Julian Goldsmid. *Introduction to Thermoelectricity*. Springer, 2010. 14, 33, 34

[36] John Sydney Blakemore. *Solid State Physics*. Cambridge University Press, Cambridge, 2nd edition, 1985. 20

[37] Terry Tritt. *Thermal Conductivity: theory, properties, and applications*. Kluwer Academic / Plenum Publishers, 2004. 21, 54, 59, 60

[38] L. D. Hicks and M. S. Dresselhaus. Effect of quantum-well structures on the thermoelectric figure of merit. *Physical Review B*, 47:12727, 1993. 23

[39] T. C. Harman, D. L. Spears, and M. P. Walsh. PbTe/Te superlattice structures with enhanced thermoelectric figures of merit. *Journal of Electronic Materials*, 28:L1, 1999. 24

[40] T. Koga, T. C. Harman, S. B. Cronin, and M. S. Dresselhaus. Mechanism of the enhanced thermoelectric power in (111)-oriented n-type PbTe/$Pb_{(1-x)}Eu_{(x)}$ Te multiple quantum wells. *Physical Review B*, 60: 14286, 1999. 24

[41] Hiromichi Ohta, Sungwng Kim, Yoriko Mune, Teruyasu Mizoguchi, Kenji Nomura, Shingo Ohta, Takashi Nomura, Yuki Nakanishi, Yuichi Ikuhara, Masahiro Hirano, Hideo Hosono, and Kunihito Koumoto. Giant thermoelectric Seebeck coefficient of a two-dimensional electron gas in $SrTiO_3$. *Nature materials*, 6:129, 2007. 24

[42] H. Ohta, Y. Mune, K. Koumoto, T. Mizoguchi, and Y. Ikuhara. Critical thickness for giant thermoelectric Seebeck coefficient of 2DEG confined in $SrTiO_3/SrTi_{0.8}Nb_{0.2}O_3$ superlattices. *Thin Solid Films*, 516:5916, 2008. 24

[43] Raseong Kim, Supriyo Datta, and Mark S. Lundstrom. Influence of dimensionality on thermoelectric device performance. *Journal of Applied Physics*, 105:034506, 2009. 25

[44] G. D. Mahan, J. O. Sofo, and M. Bartkowiak. Multilayer thermionic refrigerator and generator. *Journal of Applied Physics*, 83:4683, 1998. 25

[45] J. M. Zide, D. O. Klenov, S. Stemmer, A. C. Gossard, G. Zeng, J. E. Bowers, D. Vashaee, and A. Shakouri. Thermoelectric power factor in semiconductors with buried epitaxial semimetallic nanoparticles. *Applied Physics Letters*, 87:112102, 2005. 26, 82

[46] A. F. Ioffe. *Semiconductor Thermoelecments and Thermoelectric Cooling*. Infosearch Limited, London, 1957. 28

[47] E. A. Skrabek and D. S. Trimmer. *CRC Handbook of Thermoelectrics*. CRC Press, 1995. 29

[48] B. A. Cook, M. J. Kramer, X. Wei, J. L. Harringa, and E. M. Levin. Nature of the cubic to rhombohedral structural transformation in $(AgSbTe_2)_{15}(GeTe)_{85}$ thermoelectric material. *Journal of Applied Physics*, 101:053715, 2007. 29

[49] Nancy Chen, Franck Gascoin, Jeffrey Snyder, Eckhard Muller, Gabriele Karpinski, and Christian Stiewe. Macroscopic thermoelectric inhomogeneities in $(AgSbTe_2)_x(PbTe)_{(1-x)}$. *Applied Physics Letters*, 87:171903, 2005. 30

[50] J. Androulakis, K. F. Hsu, R. Pcionek, H. Kong, C. Uher, J. J. D'Angelo, A. Downey, T. Hogan, and M. G. Kanatzidis. Nanostructuring and High Thermoelectric Efficiency in p-Type $Ag(Pb_{(1-y)}Sn_y)_mSbTe_{(2+m)}$. *Advanced Materials*, 18:1170, 2006. 30

[51] H. B. G. Casimir. Note on the conduction of heat in crystals. *Physica*, 5: 495, 1938. 30

[52] H. J. Goldsmid and A. W. Penn. Boundary scattering of phonons in solid solutions. *Physics Letters A*, 27:523, 1968. 30

[53] N. Savvides and H. J. Goldsmid. The effect of boundary scattering on the high-temperature thermal conductivity of silicon. *Journal of Physics C: Solid State Physics*, 6:1701, 1973. 30

[54] Takafumi Yao. Thermal properties of AlAs/GaAs superlattices. *Applied Physics Letters*, 51:1798, 1987. 31

[55] X. Y. Yu, G. Chen, A. Verma, and J. S. Smith. Temperature dependence of thermophysical properties of GaAs/AlAs periodic structure. *Applied Physics Letters*, 67:3554, 1995. 31

[56] S.-M. Lee, D. G. Cahill, and Rama Venkatasubramanian. Thermal conductivity of Si-Ge superlattices. *Applied Physics Letters*, 70:2957, 1997. 31

[57] I. Yamasaki, R. Yamanaka, and M. Mikami. Thermoelectric properties of Bi_2Te_3/Sb_2Te_3 superlattice structure. *ICT1998 Proceedings*, page 210, 1998. 31

[58] D. W. Song, W. L. Liu, T. Zeng, T. Borca-Tasciuc, G. Chen, J. C. Caylor, and T. D. Sands. Thermal conductivity of skutterudite thin films and superlattices. *Applied Physics Letters*, 77:3854, 2000. 31

[59] R. Venkatasubramanian, E. Siivola, T. Colpitts, and B. O'Quinn. Thin-film thermoelectric devices with high room-temperature figures of merit. *Nature*, 413:597, 2001. 31

[60] Akram I. Boukai, Yuri Bunimovich, Jamil Tahir-Kheli, Jen-Kan Yu, William A. Goddard, and James R. Heath. Silicon nanowires as efficient thermoelectric materials. *Nature*, 451:168, 2008. 31

[61] T. C. Harman, D. L. Spears, and J. M. Manfra. High thermoelectric figures of merit in PbTe quantum wells. *Journal of Electronic Materials*, 25:1121, 1996. 32

[62] T. C. Harman, P. J. Taylor, M. P. Walsh, and B. E. LaForge. Quantum dot superlattice thermoelectric materials and devices. *Science*, 297:2229, 2002. 32

[63] L. I. Arutyunyan, V. N. Bogomolov, N. F. Kartenko, D. A. Kurdyukov, V. V. Popov, A. V. Prokofev, I. A. Smirnov, and N. V. Sharenkova. Thermal conductivity of a new type of regular-structure nanocomposites: PbSe in opal pores. *Physics of the Solid State*, 39:510, 1997. 32

[64] David Song and Gang Chen. Thermal conductivity of periodic microporous silicon films. *Applied Physics Letters*, 84:687, 2004. 32

[65] Glen Slack. *CRC Handbook of Thermoelectrics*. CRC Press, 1995. 32

[66] D. G. Cahill, S. K. Watson, and R. O. Pohl. Lower limit to the thermal conductivity of disordered crystals. *Physical Review B*, 46:6131, 1992. 32

[67] D. T. Morelli, T. Caillat, J. P. Fleurial, A. Borshchevsky, J. Vandersande, B. Chen, and C. Uher. Low-temperature transport properties of p-type $CoSb_3$. *Physical Review B*, 51:9622, 1995. 33

[68] B. C. Sales, D. Mandrus, B. C. Chakoumakos, V. Keppens, and J. R. Thompson. Filled skutterudite antimonides: Electron crystals and phonon glasses. *Physical Review B*, 56:15081, 1997. 33

[69] G. S. Nolas, H. Takizawa, T. Endo, H. Sellinschegg, and D. C. Johnson. Thermoelectric properties of Sn-filled skutterudites. *Applied Physics Letters*, 77:52, 2000. 33

[70] L. D. Chen, T. Kawahara, X. F. Tang, T. Goto, T. Hirai, J. S. Dyck, W. Chen, and C. Uher. Anomalous barium filling fraction and n-type thermoelectric performance of $Ba_yCo_4Sb_{12}$. *Journal of Applied Physics*, 90: 1864, 2001. 33

[71] X. Shi, L. Chen, J. Yang, and G. P. Meisner. Enhanced thermoelectric figure of merit of $CoSb_3$ via large-defect scattering. *Applied Physics Letters*, 84: 2301, 2004. 33

[72] J. L. Cohn, G. S. Nolas, V. Fessatidis, T. H. Metcalf, and G. A. Slack. Glasslike Heat Conduction in High-Mobility Crystalline Semiconductors. *Physical Review Letters*, 82:779, 1999. 33

[73] V. L. Kuznetsov, L. A. Kuznetsova, and A. E. Kaliazin. Preparation and thermoelectric properties of ABB clathrate compounds. *Journal of Applied Physics*, 87:7871, 2000. 33

[74] A. Saramat, G. Svensson, A. E. C. Palmqvist, C. Stiewe, E. Mueller, D. Platzek, S. G. K. Williams, D. M. Rowe, J. D. Bryan, and G. D. Stucky. Large thermoelectric figure of merit at high temperature in Czochralski-grown clathrate $Ba_8Ga_{16}Ge_{30}$. *Journal of Applied Physics*, 99:023708, 2006. 33

[75] E. Toberer, M. Christensen, B. Iversen, and G. Snyder. High temperature thermoelectric efficiency in $Ba_8Ga_{16}Ge_{30}$. *Physical Review B*, 77:075203, 2008. 33

[76] I. Terasaki and Y. Sasago. Large thermoelectric power in $NaCo_2O_4$ single crystals. *Physical Review B Rapid Communications*, 56:R12 685, 1997. 35

[77] K. Koumoto, I. Terasaki, and R. Funahashi. Complex oxide materials for potential thermoelectric applications. *Mater. Res. Soc. Bull.*, 31:206, 2006. 35

[78] Hiromichi Ohta, Kenji Sugiura, and Kunihito Koumoto. Recent progress in oxide thermoelectric materials: p-type $Ca_3Co_4O_9$ and n-type $SrTiO_{3-}$. *Inorganic Chemistry*, 47:8429, 2008. 35

[79] T. Caillat, J. Fleurial, and A. Borshchevsky. Preparation and thermoelectric properties of semiconducting Zn_4Sb_3. *Journal of Physics and Chemistry of Solids*, 58:1119, 1997. 36

[80] Yoshisato Kimura and Akihisa Zama. Thermoelectric Properties of P-type Half-Heusler Compounds HfPtSn and ZrPtSn. *ICT 2006 Proceedings*, page 115, 2006. 36

[81] Susan M. Kauzlarich, Shawna R. Brown, and Jeffrey G. Snyder. Zintl phases for thermoelectric devices. *Dalton transactions (Cambridge, England)*, page 2099, 2007. 36, 37

[82] Jeffrey G. Snyder and Eric S. Toberer. Complex thermoelectric materials. *Nature materials*, 7:105, 2008. 37

[83] P. Blood and J. W. Orton. *The Electrical Characterization of Semiconductors: majority Carriers and Electron States*. Academic Press, 1992. 40, 51, 52

[84] R. Heikes and R. W. Ure. *Thermoelectricity: Science and Engineering*. Interscience, New York, 1961. 40

[85] C. Wood, A. Chmielewski, and D. Zoltan. Measurement of Seebeck coefficient using a large thermal gradient. *Review of Scientific Instruments*, 59: 951, 1988. 41

[86] A. T. Burkov, A. Heinrich, P. P. Konstantinov, T. Nakama, and K. Yagasaki. Experimental set-up for thermopower and resistivity measurements at 100-1300 K. *Measurement Science and Technology*, 12:264, 2001. 41

[87] O. Boffoue, A. Jacquot, A. Dauscher, B. Lenoir, and M. Stolzer. Experimental setup for the measurement of the electrical resistivity and thermopower of thin films and bulk materials. *Review of Scientific Instruments*, 76: 053907, 2005. 41

[88] Zhenhua Zhou and Ctirad Uher. Apparatus for Seebeck coefficient and electrical resistivity measurements of bulk thermoelectric materials at high temperature. *Review of Scientific Instruments*, 76:023901, 2005. 41

[89] V. Ponnambalam, S. Lindsey, N. S. Hickman, and Terry M. Tritt. Sample probe to measure resistivity and thermopower in the temperature range of 300-1000 K. *Review of Scientific Instruments*, 77:073904, 2006. 41

[90] L. Cowles and L. Dauncey. Apparatus for the rapid scanning of the Seebeck coefficient of semiconductors. *Journal of Scientific Instruments*, 39:16, 1962. 41

[91] H. J. Goldsmid. A simple technique for determining the Seebeck coefficient of thermoelectric materials. *Journal of Physics E: Scientific Instruments*, 19:921, 1986. 41

[92] S. R. Sarath Kumar and S. Kasiviswanathan. A hot probe setup for the measurement of Seebeck coefficient of thin wires and thin films using integral method. *The Review of Scientific Instruments*, 79:024302, 2008. 41

[93] Stainless Steal - Grade 304, . URL http://www.azom.com/article.aspx?ArticleID=965. 43

[94] Stainless Steal - Grade 310, . URL http://www.azom.com/article.aspx?ArticleID=966. 43

[95] James Chan and Paul Friedberg. Four-Point Probe Manual. URL http://physlab.lums.edu.pk/images/c/c6/Four_point_probe.pdf. 45

[96] D. G. Cahill and R. O. Pohl. Thermal conductivity of amorphous solids above the plateau. *Physical Review B*, 35:4067, December 1987. 55, 58

[97] David G. Cahill. Thermal conductivity measurement from 30 to 750 K: the 3ω method. *Review of Scientific Instruments*, 61:802, 1990. 55, 56, 57

[98] S.-M. Lee and David G. Cahill. Heat transport in thin dielectric films. *Journal of Applied Physics*, 81:2590, 1997. 55, 57

[99] S.-M. Lee, David G. Cahill, and Rama Venkatasubramanian. Thermal conductivity of Si-Ge superlattices. *Applied Physics Letters*, 70:2957, 1997. 55

[100] Rama Venkatasubramanian. Lattice thermal conductivity reduction and phonon localizationlike behavior in superlattice structures. *Physical Review B*, 61:3091, 2000. 55

[101] Scott T. Huxtable, Alexis R. Abramson, Chang-Lin Tien, Arun Majumdar, Chris LaBounty, Xiaofeng Fan, Gehong Zeng, John E. Bowers, Ali Shakouri, and Edward T. Croke. Thermal conductivity of Si/SiGe and SiGe/SiGe superlattices. *Applied Physics Letters*, 80:1737, 2002. 55

[102] T. Borca-Tasciuc, D. W. Song, J. R. Meyer, I. Vurgaftman, M.-J. Yang, B. Z. Nosho, L. J. Whitman, H. Lee, R. U. Martinelli, G. W. Turner, M. J. Manfra, and G. Chen. Thermal conductivity of $AlAs_{0.07}Sb_{0.93}$ and $Al_{0.9}Ga_{0.1}As_{0.07}Sb_{0.93}$ alloys and $(AlAs)_1/(AlSb)_1$ digital-alloy superlattices. *Journal of Applied Physics*, 92:4994, 2002. 55

[103] H. S. Carslaw and J. C. Jaeger. *Conduction of Heat in Solids*. Oxford University Press, Oxford, 1959. 56

[104] K. Maize, Y. Ezzahri, X. Wang, S. Singer, A. Majumdar, and A. Shakouri. Measurement of Thin Film Isotropic and Anisotropic Thermal Conductivity using 3 omega and Thermoreflectance Imaging. *Semiconductor Thermal Measurement and Management Symposium, 2008*, page 185, 2008. 58

[105] Yee Kan Koh, Suzanne L. Singer, Woochul Kim, Joshua M. O. Zide, Hong Lu, David G. Cahill, Arun Majumdar, and Arthur C. Gossard. Comparison of the 3ω method and time-domain thermoreflectance for measurements of the cross-plane thermal conductivity of epitaxial semiconductors. *Journal of Applied Physics*, 105:054303, 2009. 58, 61

[106] David G. Cahill. Analysis of heat flow in layered structures for time-domain thermoreflectance. *Review of Scientific Instruments*, 75:5119, 2004. 61

[107] Ho-Ki Lyeo, David G. Cahill, Bong-Sub Lee, John R. Abelson, Min-Ho Kwon, Ki-Bum Kim, Stephen G. Bishop, and Byung-Ki Cheong. Thermal conductivity of phase-change material $Ge_2Sb_2Te_5$. *Applied Physics Letters*, 89:151904, 2006. 61

[108] Ruxandra Costescu, Marcel Wall, and David Cahill. Thermal conductance of epitaxial interfaces. *Physical Review B*, 67:054302, 2003. 61

[109] Yee Koh and David Cahill. Frequency dependence of the thermal conductivity of semiconductor alloys. *Physical Review B*, 76:075207, 2007. 61

[110] J. H. Lee, G. A. Galli, and J. C. Grossman. Nanoporous Si as an efficient thermoelectric material. *Nanoletters*, 8:3750, 2008. 63

[111] F. Corni, G. Calzolari, F. Gambetta, and C. Nobili. Evolution of vacancy-like defects in helium-implanted (100) silicon studied by thermal desorption spectrometry. *Materials Science and Engineering B*, 71:207, 2000. 64, 65

[112] S. Frabboni, F. Corni, C. Nobili, R. Tonini, and G. Ottaviani. Nanovoid formation in helium-implanted single-crystal silicon studied by in situ techniques. *Physical Review B*, 69:165209, 2004. 64, 65

[113] E. Landi, A. Armigliato, S. Solmi, R. Kgler, and E. Wieser. Electrical Activation of Boron-Implanted Silicon During Rapid Thermal Annealing. *Applied Physics A: Solids and Surfaces*, 47:359, 1988. 66

[114] Electron energy-loss spectroscopy. URL `http://www.microscopy.ethz.ch/EELS.htm`. 67

[115] Glen A. Slack. Thermal Conductivity of Pure and Impure Silicon, Silicon Carbide, and Diamond. *Journal of Applied Physics*, 35:3460, 1964. 70, 78

[116] G. Masetti, M. Severi, and S. Solmi. Modeling of carrier mobility against carrier concentration in arsenic-, phosphorus-, and boron-doped silicon. *IEEE Transactions on Electron Devices*, 30:764, 1983. 71

[117] Xuan Luo, S. Zhang, and Su-Huai Wei. Understanding Ultrahigh Doping: The Case of Boron in Silicon. *Physical Review Letters*, 90:026103, 2003. 72

[118] J. Adey, R. Jones, and P. R. Briddon. Enhanced dopant solubility in strained silicon. *Journal of Physics: Condensed Matter*, 16:9117, 2004. 72

[119] F. S. Ham. Theory of diffusion-limited precipitation. *Journal of Physics and Chemistry of Solids*, 6:335, 1958. 73

[120] S. Solmi, E. Landi, and F. Baruffaldi. High-concentration boron diffusion in silicon: Simulation of the precipitation phenomena. *Journal of Applied Physics*, 68:3250, 1990. 73

[121] Y. I. Ravich. *CRC Handbook of Thermoelectrics*. 1995. 77

[122] A. Popescu, L. Woods, J. Martin, and G. Nolas. Model of transport properties of thermoelectric nanocomposite materials. *Physical Review B*, 79: 205302, 2009. 77

[123] Y. S. Ju and K. E. Goodson. Phonon scattering in silicon films with thickness of order 100 nm. *Applied Physics Letters*, 74:3005, 1999. 78

[124] A. D. McConnell, Srinivasan Uma, and K. E. Goodson. Thermal conductivity of doped polysilicon layers. *Journal of Microelectromechanical Systems*, 10:360, 2001. 78

[125] Laura E. Cassels, Gilles Pernot, Trevor E. Buehl, Art C. Gossard, Chris J. Palmstrom, Ali Shakouri, and Joshua M. O. Zide. Thermoelectric Properties of Epitaxial TbAs:InGaAs Nanocomposites. *in preparation*, 2011. 81, 83

[126] Woochul Kim, Joshua Zide, Arthur Gossard, Dmitri Klenov, Susanne Stemmer, Ali Shakouri, and Arun Majumdar. Thermal Conductivity Reduction and Thermoelectric Figure of Merit Increase by Embedding Nanoparticles in Crystalline Semiconductors. *Physical Review Letters*, 96:045901, 2006. 81

[127] Kris Delaney, Nicola Spaldin, and Chris Van de Walle. Theoretical study of the structural and electronic properties of strained ErAs. *Physical Review B*, 77:235117, 2008. 83

[128] Je-Hyeong Bahk, Gehong Zeng, Joshua M. O. Zide, Hong Lu, Rajeev Singh, Di Liang, Ashok T. Ramu, Peter Burke, Zhixi Bian, Arthur C. Gossard, Ali Shakouri, and John E. Bowers. High-Temperature Thermoelectric Characterization of III-V Semiconductor Thin Films by Oxide Bonding. *Journal of Electronic Materials*, 39:1125, 2010. 85

[129] Rajeev Singh and Ali Shakouri. Thermostat for high temperature and transient characterization of thin film thermoelectric materials. *Review of Scientific Instruments*, 80:025101, 2009. 86

[130] D. C. Driscoll, M. Hanson, C. Kadow, and A. C. Gossard. Electronic structure and conduction in a metalsemiconductor digital composite: ErAs:InGaAs. *Applied Physics Letters*, 78:1703, 2001. 87

[131] A. T. Ramu, L. E. Clinger, P. B. Dongmo, J. T. Imamura, J. M. O. Zide, and J. E. Bowers. The incompatibility of standard III-V processing techniques with Tb-doped InGaAs. *in preparation*. 88

[132] Ashok T. Ramu, Laura E. Cassels, Nathan H. Hackman, Hong Lu, Joshua M. O. Zide, and John E. Bowers. Rigorous calculation of the Seebeck coefficient and mobility of thermoelectric materials. *Journal of Applied Physics*, 107:083707, 2010. 88, 89